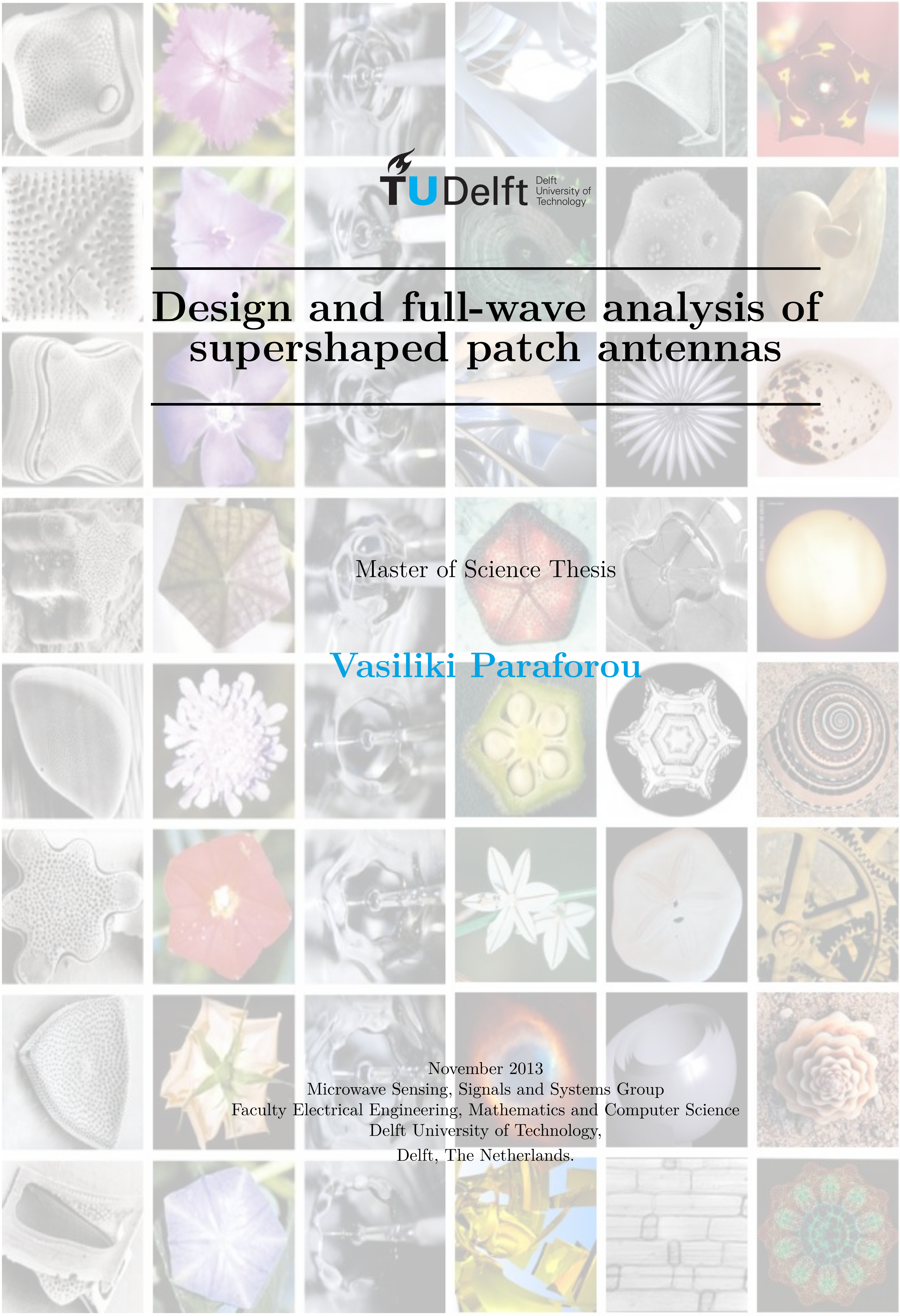

TU Delft Delft University of Technology

Design and full-wave analysis of supershaped patch antennas

Master of Science Thesis

Vasiliki Paraforou

November 2013

Microwave Sensing, Signals and Systems Group
Faculty Electrical Engineering, Mathematics and Computer Science
Delft University of Technology,
Delft, The Netherlands.

Design and full-wave analysis of supershaped patch antennas

THESIS

submitted for the degree of

MASTER OF SCIENCE IN ELECTRICAL ENGINEERING

by

Vasiliki Paraforou

Supervisors:

Dr. Diego Caratelli

Prof. Alexander Yarovoy

November 2013

Microwave Sensing, Signals and Systems Group

Faculty Electrical Engineering, Mathematics and Computer Science

Delft University of Technology,

Delft, The Netherlands.

Delft University of Technology

Σε αυτούς
που στοχάζονται ελεύθερα

Abstract

The rapid development of wireless communication systems and the subsequent burst of wireless devices place several demands on the antenna designs. In particular, the development of high-performance radio systems require the adoption of broadband antennas featuring low profile, high gain, embedded installation and reduced manufacturing costs. Printed antennas, despite their inherent limitations can meet most of these requirements by employing innovative design solutions aiming at improving their electromagnetic performance. In this respect, a novel class of supershaped patch antennas is introduced and thoroughly investigated. The geometry of the proposed radiating structures is described by the polar equation known in the scientific literature as superformula or Gielis equation. Such equation can generate a large variety of different nature-inspired and abstract shapes which translates into the possibility of automatically reshaping the geometry of the radiating patch through the tuning of its parameters and consequently modifying the circuital performance and the radiation properties. In this context, the commercially available CST Studio Suite, based on the Finite Integration Technique (FIT), is used to perform the numerically based time domain full-wave analysis of the supershaped patch antennas. These simulations help to the deduction of useful conclusions upon the characteristics of general supershaped patch antennas as a function of the pertinent Gielis parameters. Moreover, a new developed semi-analytical method is used in order to obtain a meaningful physical insight to the operation of these antennas. At the end, we explore the possibilities of building novel high-performance antenna structures based on the supershape formula that are intended for modern applications. This investigation led in the conception of two dual-band supershaped patch antenna configurations designed for the WLAN IEEE 802.11$a/b/g/n$ standards. The proposed planar designs are not only low-cost and simple to manufacture but also exhibit a plethora of attractive characteristics such as exact mathematical shaping definition, multi-band/wideband operation, very low cross-polarization levels, high radiation efficiency, frequency control capability, etc.

Contents

Chapter 1

Introduction

1.1 The development of microstrip patch antennas

Wireless communications has become the fastest growing segment of the communications industry. The explosive growth of the wireless systems such as cellular telephony, wireless local area networks, wireless sensor networks, smart home and appliances, remote telemedicine has evoked a subsequent boost of the wireless devices. Furthermore, a number of other technology fields have embedded wireless features to their applications. Namely, high performance aircraft, spacecraft, satellite and missile applications' design includes high demanding wireless specifications. Accordingly, in regard to the antenna needs of many of these wireless systems size, weight, cost, performance, ease of installation and aerodynamic profile are constraints which must be satisfied. Hence, low-profile antennas should be used in order to meet these requirements. Microstrip patch antennas are suitable for this kind of applications since they are low profile, adaptable to planar and non planar surfaces, simple and inexpensive to manufacture using modern printed-circuit technology, mechanically robust when mounted on rigid surfaces and compatible with MMIC designs. Additionally, when the particular patch shape and mode are selected, they are very versatile in terms of resonant frequency, polarization, pattern and impedance. For these reasons they have become favourites among antenna designers and have been widely used in the military as well as in the commercial sector.

Microstrip technology has been popular for millimetre wave applications since the 1970s and recently has taken off, with the tremendous growth in communications, wireless, as well as space-born/airborne applications, although the concept dates back to 1952 [1]. The basic microstrip configuration is very similar to a printed circuit board (PCB) used for low frequency electronic circuits. It constitutes a low-loss thin substrate, both sides being coated with copper film. Printed transmission lines, patches, etc. are etched out on one side of the microstrip board and the other copper-clad surface is used as the ground plane. In between the ground plane and the microstrip structure, a quasi-TEM electromagnetic wave is launched and allowed to spread.

Such a structure offers some unique basic advantages such as low profile, low cost, light weight, ease of fabrication, suitability to conform on curved surface, etc. All these have made microstrip technology attractive since the early phase of its development.

In 1953, a year after the publication of the article of Greig and Engelmann [1], Deschamps [2] had conceived of microstrip as ”microwave antenna”. But its practical application started nearly two decades later. Then, Howell [3] and Munson [4] may be considered as the pioneer architects of microstrip antenna engineering.

These early developments immediately attracted some potential research groups and the following studies were mainly concerned with theoretical analysis of different patch geometries and experimental verifications. A parallel trend also developed very quickly and some researchers tried to implement conventional antennas such as dipole, wire, aperture, etc. in planar form. They are commonly referred to as printed circuit antennas or simply *printed antennas*. Their operations and characteristics are completely different from those due to microsttrip patches, although microstrip patch antennas, in many papers, are casually called printed circuit antennas.

Since the perception of the concept of the microstrip patch antenna in the early 1950s and in the late 1970s that this type of antenna attracted serious attention of the antenna community, significant progress was noted in terms of broadbanding, dual and multiband operation, size reduction and others. The almost forty years old substantial investigation has yielded a great amount of research articles in archival journals, several review articles and more than a dozen books related to microstrip patch antennas.

1.2 The supershaped patch antennas project

The goal of this thesis is the analysis of supershaped patch antennas and the investigation of their potential as antenna design solutions. The patch profile of these antennas results from a parametrically defined mathematical equation known as *Gielis* formula or supershape formula. Furthermore, it is aimed to propose some new antenna configurations for wireless applications whose patch shape is generated by the supershape formula. So, after almost forty years of thorough studies, the reasonable question is what new aspects this project brings to the extended list of research analysis on microstrip patch antennas.

Challenges

- The introduction of a mathematical formula (*Gielis* formula) into the antenna design sector. Specifically, this research part includes the correlation of the relevant equation parameters with the performance characteristics of the patch antennas. Moreover, the selection of the appropriate values for the equation parameters since the multi-parametric dependence and the non-linearity of the *Gielis* formula complicates this task.
- Since there is no closed-form relation describing the field configuration of irregularly shaped patch antennas but only full-wave solvers, alternative methods providing a profound comprehension of the antenna's operation needed to be explored.
- The investigation of the possibilities regarding the utilization of *Gielis* formula in new antenna designs meeting high standards concerning wideband or multi-band function. In this respect, certain requirements about the operational bandwidth, the polarization, the radiation pattern and the profile of the structure should be met.

Approach

- Firstly, the necessary literature study about the newest trends regarding the patch antenna design was carried out. Furthermore, particular attention was given to antenna structures featuring irregular shapes.

- Then we explore the possible radiator shapes that can be derived by the supershape formula. A group of basic patch antennas whose patch geometry is based on some of these shapes are analysed with a commercially available full-wave solver and their performance is associated with the relevant equation's parameters.

- In order to give an interpretation of the performance characteristics derived from the numerical analysis we need to resort to analytical tools. A semi-analytical approach that combines the cavity model theory and the numerically based solutions helps in understanding the principles of the function mechanism.

- After establishing the fundamental background from the literature study and the supershaped patch antennas analysis we proceed further to the design procedure. It was aimed to create a new patch antenna whose basic profile is produced by the supershape formula. As design goal, a dual-band operation at $2.4/5\,GHz$, suitable for WLAN applications, was set. This is because there is a high interest in the research community for multi-frequency antenna structures since practically they consist two antennas incorporated into one device. Finally, two new antennas meeting the above requirements are proposed and analysed. One printed dipole antenna with balanced feeding and one annular slot loaded patch antenna fed by a coaxial probe.

Novelties

- A mathematical formula such as *Gielis* formula is used for planar antenna designs. The patch shape optimization was realized through the variation of six parameters (four if symmetry is required).

- Generally, a dipole antenna features an omnidirectional radiation pattern. On the contrary,the proposed printed dipole has a unidirectional radiation pattern due to the introduction of a ground plane making the use of absorption cavities unnecessary.

- The development of a novel supeshaped dual-band printed dipole with broadside radiation for WLAN applications. The cross-polarization levels obtained are of the order of $-160\,dB$ which is the lowest ever recorded for a microstrip patch antenna.

- A novel supershaped dual-band annular slotted patch antenna intended for WLAN systems is presented. The change of the slot width through the scaling of the ring slot contour profiles yields a frequency ratio range f_h/f_l of about 1.3 to 3. The antenna features also high frequency selectivity and high sensitivity levels.

1.3 Thesis outline

Chapter 2

This is an introductory chapter which covers the primary concept of the microstrip patch antennas. The basic model of the patch antenna with its operation principles is presented. Also the most common feeding techniques as well as the fundamental characteristics are cited.

Chapter 3

In this chapter all the recent advances and trends regarding the microstrip patch antennas are summarized. There are three sections dedicated to the broadbanding methods, the dual-frequency operation techniques and the circularly polarized patch antennas respectively.

Chapter 4

There are three main categories of analysis methods regarding the microstrip patch antennas. Here, the transmission line model and the cavity model are presented. The third wide category comprises the numerical methods such as *method of moments* (MoM), *finite-difference time-domain* (FDTD), *finite element method* (FEM), etc. In this thesis, a short overview of the *finite integration technique* (FIT) is given since this is the technique that is employed by the solver of *CST Microwave Studio*.

Chapter 5

In chapter 5 the correlation between the patch shape and the impedance bandwidth is studied. Also, the *Gielis* formula (supershape formula) is introduced as a tool for the production of a variety of possible radiator shapes.

Chapter 6

The results of the full-wave analysis of a group of supershaped patch antennas are included in this chapter. The performance characteristics such as the impedance bandwidth, the realized gain and the radiation pattern are thoroughly investigated and some useful conclusions necessary for the further usage of the supershape formula are deduced.

Chapter 7

In this chapter the supershaped patch antennas are analysed based on a semi-analytical technique. Namely, it is a combination of the cavity model theory and the full-wave analysis provided by the commercial software *CST Microwave Studio*. This study gives us a better insight in the operation of the patch antennas and helps us understand the basic operation principles that are necessary for the design process.

Chapter 8

The last chapter consists of the presentation of two novel proposed designs resulting from the supershape formula. These new antenna designs demonstrate a dual-band operation which is a fundamental requirement for the modern antenna systems. Specifically, they are suitable for the WLAN IEEE 802.11$a/b/g/n$ standards operating at 2.4/5 GHz bands.

Chapter 9

The results of the thesis are summarized and commented. Also, in the end remarks and recommendations for future work are lined up.

Chapter 2

The microstrip patch antenna

2.1 Principal model

Microstrip antennas consist of a very thin ($t \ll \lambda_0$, where λ_0 is the free-space wavelength) metallic strip (patch) placed a small fraction of wavelength ($h \ll \lambda_0$, usually $0.003\lambda_0 \leq h \leq 0.05\lambda_0$) above a ground plane. The patch and the ground plane are separated by a dielectric substrate. A typical microstrip patch antenna configuration is illustrated in figure 2.1. The radiation pattern is dependent on electric current distribution on the patch. The patch shape, feeding structure and substrate properties can be chosen to achieve the desired performance for a specific application.

The radiator should be a material with low ohmic loss and high conductivity at the operating frequency (such as copper), which can be fixed to a dielectric substrate. The shape of the radiating patch may be square, rectangular, thin strip (dipole), circular, elliptical, triangular, or any other configuration. More complex variations on the basic shapes are frequently used to meet particular design demands. The selection of a particular shape is contingent on specific requirements in terms of polarization, bandwidth, gain, etc. Square, rectangular, strip and circular are the most common because of ease of analysis and fabrication, and their attractive radiation characteristics, especially low-cross polarization radiation. For a rectangular patch, the length L of the element is usually $\lambda_0/3 < L < \lambda_0/2$. In general, the antenna's characteristics are defined by the excited operating modes, which depend on the

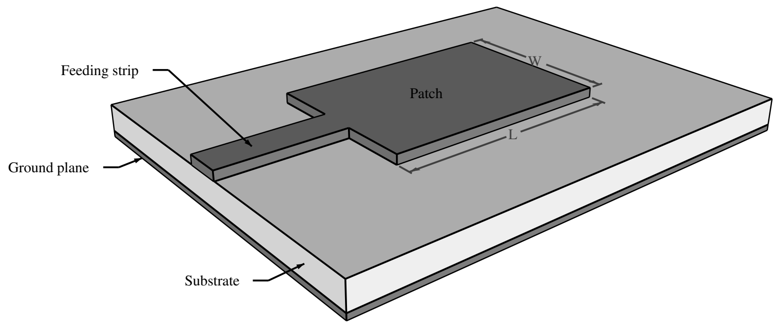

(a) Microstrip antenna

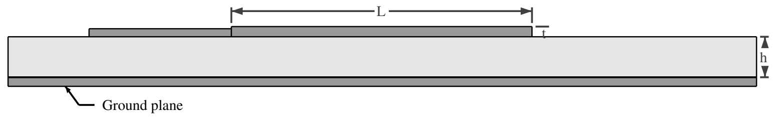

(b) Side view

Figure 2.1 Microstrip antenna

shape and dimensions of the patch, the thickness and dielectric constant of the substrate, as well as the feed arrangement.

There is a multitude of dielectric materials available for substrates, and their dielectric constants are usually in the range of $2.2 \leq \epsilon_r \leq 12$. Cost, power loss, and performance are trade-off considerations in choosing the substrate material. Namely, due to their low cost, ease of manufacture and good surface adhesion, plastics are commonly used in RF and microwave bands, although they have large thermal expansion coefficients, poor dielectric properties, poor dimensional stability and poor thermal conductivity compared with other materials such as ceramic and sapphire. The substrates that are most desirable for good antenna performance are thick substrates whose dielectric constant is in the lower end of the range because they provide better efficiency, larger bandwidth, loosely bound fields for radiation into space, but at the expense of larger element size. Thin substrates with higher dielectric constants are desirable for microwave circuitry because they require

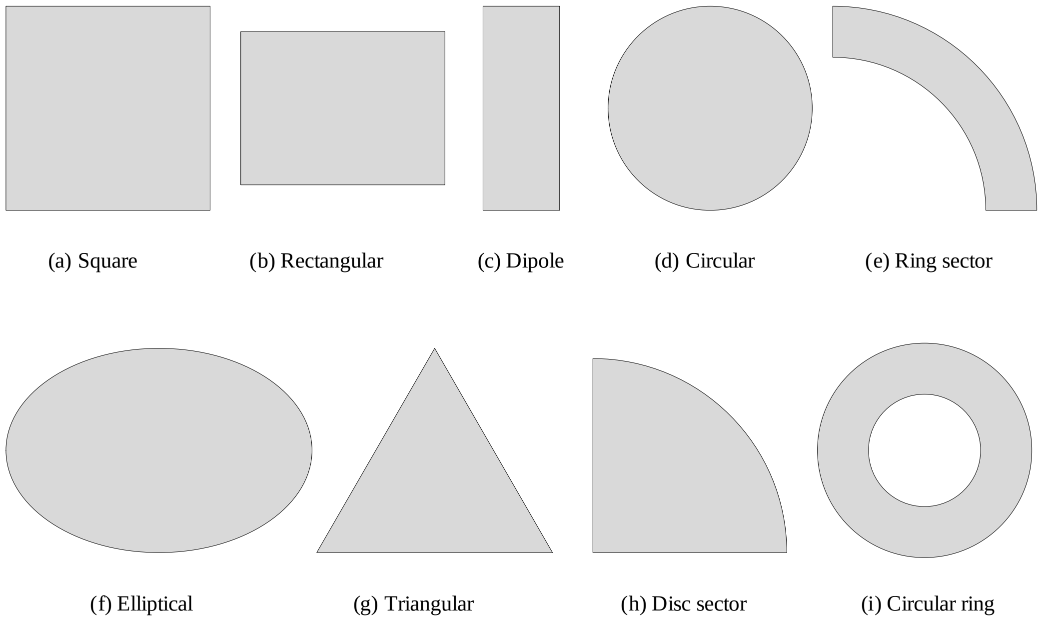

Figure 2.2 Representative shapes of radiators

tightly bound fields to minimize undesired radiation and coupling, and lead to smaller element sizes. However, because of their greater losses, they are less efficient and have relatively smaller bandwidths. Since microstrip antennas are often integrated with other microwave circuitry, a compromise has to be reached between good antenna performance and circuit design.

The most commonly used material is Teflon-based with a relative permittivity between 2 and 3. This material is also called PTFE (PolyTeraFluoroEthylene). It has a structure very similar to fibreglass material used for digital circuit boards, but has a much lower loss tangent.

2.2 Feeding methods

The feed must transfer energy efficiently from the transmission system to the antenna. There are many configurations that can be used for this purpose. The design of the feeding structure directly affects the impedance matching, operating modes, spurious radiation, surface waves and geometry of the antenna. The feeding structure thus plays a vital role in widening the impedance bandwidth and enhancing radiation performance. The four most popular feeding methods are the microstrip line, coaxial probe, aperture coupling and proximity coupling.

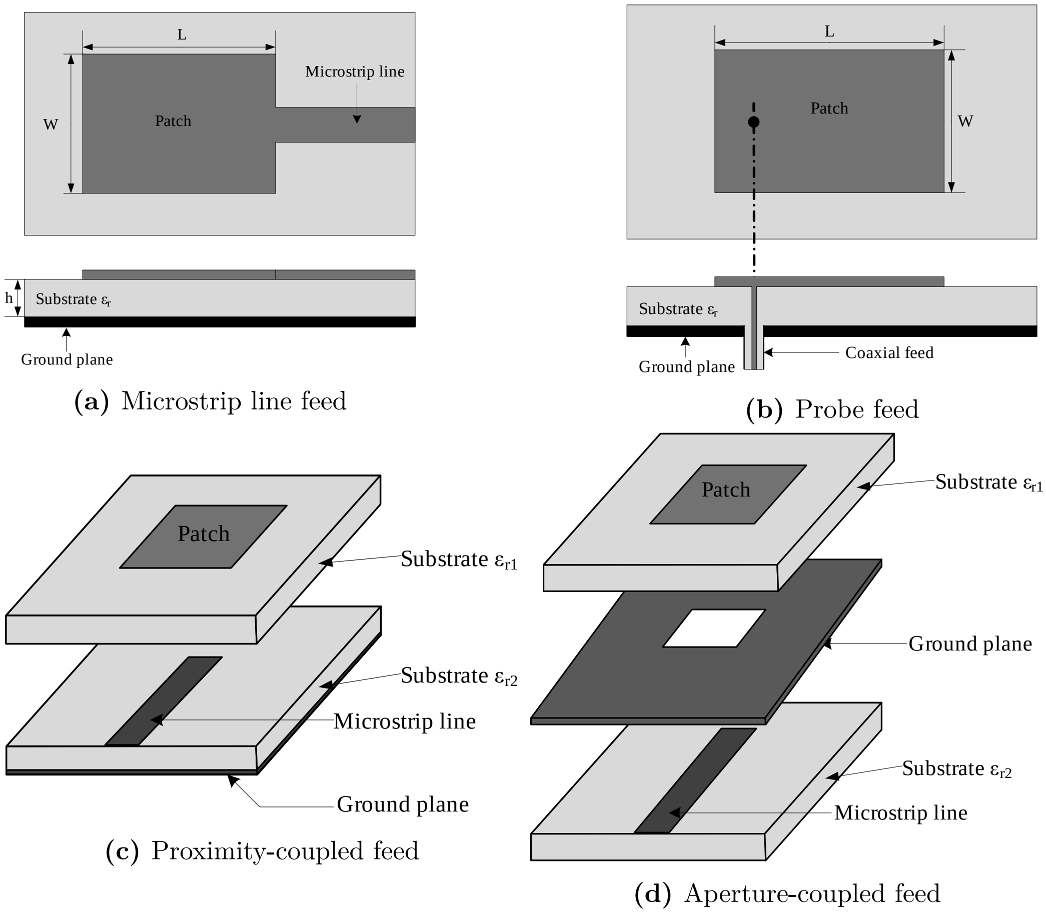

Figure 2.3 Typical feeds for microstrip antennas

The microstrip-line feed is also a conducting strip as shown in figure 2.3a, usually of much smaller width compared to the patch. It is easy to fabricate, not costly, simple to match by controlling the inset position and rather simple to model. The feeding strip may be fed by a transmission line, a surface-mounted RF connector or a coaxial line at the end of the ground plane. The feeding strip may be directly attached or coupled to the edge of the patch. To avoid impedance mismatch, sections of quarter-wavelength transformers can be used to transform a large input impedance to a 50 *ohm* line. Another method of matching the antenna impedance is to extend the microstrip line into the patch. However, as the substrate thickness increases, surface waves and spurious feed radiation increase, which for practical designs limit the bandwidth (typically $2-5\%$)

The coaxial probe feed is perhaps the most common feeding method. According to its configuration presented in figure 2.3b, the inner conductor of the coax is attached to the radiation patch while the outer conductor is connected to the ground plane. Its characteristic impedance is usually $50\,ohm$. The input impedance of the patch antenna varies with the feed location, thus, the location of the probe should be at a $50\,ohm$ point of the patch to achieve impedance matching. Therefore, the coaxial probe feed is also easy to fabricate and match and it has low spurious radiation. However, it also has narrow bandwidth and it is more difficult to model, especially for thick substrates ($h > 0.02\lambda_0$).

Both the microstrip feed line and the probe possess inherent asymmetries which generate higher order modes which produce cross-polarized radiation. To overcome some of these problems, non contacting aperture-coupling feeds, have been introduced. Such a method is the proximity-coupled feeding (figure 2.3c), whereby an open-ended microstrip feed line is located below the radiation patch but above a ground plane. There are thus two dielectric layers between the patch and the ground plane. Energy is transferred by means of the electromagnetic coupling between the patch and the feeding strip. Owing to the double-layered structure, the impedance bandwidth may be increased by properly aligning the patch and the feeding strip. However, the multi-layered structure increases fabrication cost and surface wave losses.

The aperture coupling (2.3d) is the most difficult of the four feeding techniques presented to fabricate and it also has a narrow bandwidth. However, it is somewhat easier to model and has moderate spurious radiation. The aperture coupling consists of two substrates separated by a ground plane. On the bottom side of the lower substrate there is a microstrip feed line whose energy is coupled to the patch through a slot on the ground plane separating the two substrates. This arrangement allows independent optimization of the feed mechanism and the radiating element. Typically a high dielectric material is used for the bottom substrate, and thick low dielectric constant material for the top substrate. The ground plane between the substrates also isolates the feed from the radiating element and minimizes interference of spurious radiation for pattern formation and polarization purity. For this design, the substrate electrical parameters, feed line width and slot size and position can be used to optimize the design. Typically, matching is performed by controlling the width of the feed line and the length of the slot. An antenna excited by this feeding structure usually features wider bandwidth compared to the coax probe feed, high polarization purity but is has higher fabrication complexity as mentioned above, higher cost than single layered structures and back radiation from the slot.

Modelling techniques

There are two approaches to deducing the performance characteristics of microstrip patch antennas. One is to devise a physical model based on a number of simplifying assumptions and the other is to solve Maxwell's equations subject to the boundary conditions. The physical model used for the deduction of the characteristics of the patch antennas is the cavity model [6] and it is based on a number of assumptions applicable to thin substrates. These assumptions enable the fields between the patch and the ground plane to be determined analytically for a number of patch shapes. From these, the various characteristics of the microstrip patch antenna can be calculated. Within its limitations, the theory provides an understanding of the physical principles and can predict the parametric dependence of a number of antenna characteristics. In practice, it is rare that certain performance specifications can be met by the basic microstrip patch antenna structure. Thick substrates and additional features, such as parasitic patches, shorting pins or slots in the patch have to be added. Unfortunately, once the structure departs from the basic geometry, it is not amenable to analysis via a simple model. Maxwell's equations must be solved and boundary conditions satisfied, a procedure known as full-wave analysis. Such analysis, while not providing much physical insight and requiring extensive computation time, does yield numerical results predicting the performance of the antenna structure.

According to cavity model, microstrip antennas resemble dielectric-loaded cavities, and they exhibit higher order resonances. The normalized fields within the dielectric substrate (between the patch and the ground plane) can be found more accurately by treating that region as a cavity bounded by electric conductor (above and below it) and by magnetic walls (to simulate an open circuit) along the perimeter of the patch. This is an approximate model, which in principle leads to a reactive input impedance (of zero or infinite value of resonance), and it does not radiate any power. However, assuming that the actual fields are approximate to those generated by such a model, the computed pattern, input admittance and resonant frequencies compare well with measurements.

In the last two decades, many commercial simulation softwares based on the full-wave method are available. One class of them uses the method of moments (MoM) [7] in the numerical analysis, which solves the integral equations for the unknown currents resulting from the boundary conditions. Another approach converts Maxwell's equations into difference equations, which, together with appropriate models for the boundary conditions, are solved numerically in the time domain. This is known as the finite-difference time-domain (FDTD) method [8]. Still another method, known as the finite element method, solves Maxwell's equation in the form of the vector wave equation by the Rayleigh-Ritz variational method.

2.3 Basic characteristics

While differing in detail, there are a number of features which are common to the basic geometry of the patch antennas, irrespective of the shapes of the patch. These features follow naturally from viewing the patch antenna as a leaky cavity with losses.

- There are an infinite number of resonant modes, each characterized by a resonant frequency. The latter is dependent on the size and shape of the patch, the relative permittivity of the substrate ε_r and to some extend the thickness of the substrate. For example if the patch is rectangular in shape with dimensions a and b, the resonant frequencies are determined by
$$f_{mn} = \frac{k_{mn} c}{2\pi\sqrt{\varepsilon_r}} \tag{2.3.1}$$
where $k_{mn} = \left[(m\pi/a)^2 + (n\pi/b)^2\right]^{1/2}$. Similarly, if the patch is circularly shaped with radius a the resonant frequencies are given by
$$f_{mn} = \frac{X_{mn} c}{2\pi a\sqrt{\varepsilon_r}} \tag{2.3.2}$$
where X_{mn} are the roots of the equation $J'_m(X_{mn}) = 0$. J_m is the Bessel function of the first kind of order m.
- The fields at the edges of the patch undergo fringing which influences the resonant frequency of the antenna. The amount of fringing is a

function of the dimensions of the patch and the height of the substrate Because of fringing fields, the patch behaves as if it has a slightly larger dimension. Semi-empirical factors are usually introduced to obtain these effective dimensions. These factors vary from patch to patch.

- Each resonant mode has its own characteristic radiation patterns. The lowest mode, normally (1,0) or (0,1), usually radiates strongest in the broadside direction. The patterns are broad, with half-power beamwidths of the order of 100° and the gain is typically $5dB$.

- When the feeding method is the coaxial probe, the input impedance is dependent on the feed position. The variation of input resistance at resonance with feed position essentially follows that of the cavity field. The magnitude of the input impedance can vary from tens to hundreds of ohms. By choosing the feed position properly, an effective match between the antenna and the transmission line can be achieved. Also, the use of thin substrates ($h \leq 0.03\lambda_0$) will minimize the feed inductance at resonance, resulting in a reflection coefficient S_{11} near zero. For linear polarization, the impedance bandwidth is customarily defined as the range of frequencies for which the return loss is less than or equal to $10dB$.

- Since the cavity under the patch is basically a resonator, the total Q and the impedance bandwidth are dependent on the thickness of the substrate h and its permittivity ε_r. In general, the impedance bandwidth is found to increase with substrate thickness h and inversely proportional to $\sqrt{\varepsilon_r}$. However, use of low permittivity substrates can lead to high levels of radiation from the feed lines while for higher permittivities, an increase in substrate thickness can lead to decrease in efficiency due to surface wave generation. Additionally, when the substrate thickness exceeds about $0.05\lambda_0$, where λ_0 is free space wavelength, the antenna cannot be matched to the feedline. As a result, for the basic patch antenna geometry, the impedance bandwidth is limited to about 5%.

Chapter 3

State of the art

3.1 Broadbanding techniques

The microstrip patch antenna in the basic form of a conducting patch in a grounded substrate is inherently narrowband and is not able to meet the requirements of wireless communication systems. Whereas bandwidth can be increased by using lossy substrates, this is usually not desirable as efficiency will be reduced. In the last decades, a number of techniques have been developed to broaden the bandwidths of microstrip patch antennas, without compromising efficiency. The various designs provide bandwidths in the range from 10% to 60%. They have been developed basing on one or more of the following principles:

1. The excitation of two or more adjacent resonances within the operating frequency range simultaneously has been shown to be a practical way of enhancing the bandwidth. This is achieved by placing parasitic elements or slots close to the main radiator. These are excited by means of the electromagnetic coupling between them and the main patch. The parasitic elements can be in the same plane as, or stacked above, the main patch.

2. One way to alleviate the narrow bandwidth is to reduce Q. Using thick substrates of low permittivity decreases the Q and consequently broadens the bandwidth.

3. The use of an impedance matching network can reduce the mismatch problem associated with thick substrates. There are two common methods employed in microstrip patch antennas. One is to insert a sepa-

> rate matching network without altering the radiator. Another is to introduce an on-patch matching network either by slotting or notching the radiator. With both methods, the insertion of a lossy or lossless impedance matching network between the antenna and feeding structure can directly improve the impedance bandwidth.

The figures 3.1 show some wideband designs based on the above principles. In figure 3.1a, parasitic patches of sizes different from the fed patch are placed on the same plane as the fed patch. The coplanar parasitic patches are gap coupled to the fed patch and they provide a resonance near the main resonance. The thickness of the substrate remains thin ($< 0.02\lambda_0$). The bandwidth achieved in this design seldom exceeds 15% [10]. The increase of the bandwidth of patch antennas by introducing closely spaced parasitic patches on the same layer as the fed patch has been extensively studied both experimentally and theoretically. Wood in 1980 [11] showed that the impedance bandwidth of a rectangular patch can be enhanced by an adjacent patch. Aanandan et al. [12] studied a broadband design in which a rectangular patch was broken up into several gap-coupled rectangular strips. Gupta [13] showed that the impedance bandwidth can be enhanced by using parasitic patches smaller than the fed patch. By varying the number and the size of patches as well as the gap between them many configurations of coplanar patch arrays can be achieved. The parasitic elements can be coupled to the main patches along the non-radiating edges or along the main radiating edges. In the first case, one drawback is the increased cross-polarized radiation levels in H planes and even co-polarized radiation patterns in E planes, especially at higher operating frequencies. Configurations concerning the second case feature unchanged radiation performance in E-planes, but distorted co-polarized radiation patterns in H planes at higher operating frequencies. The combination of the two schemes mentioned above can be used for further bandwidth improvement. The latter design can be also employed to achieve circularly polarized operation by properly positioning the elements around the patch.

The stacked patch arrangement consists of one fed patch on one layer and one or more parasitic patch of equal or different size on another layer and is also known as as a stacked electromagnetically coupled patch antenna. Through the coupling between the stacked elements and the driven element, additional resonances are introduced, so, the impedance bandwidth can be increased greatly. Usually the bandwidth achieved in this design is usually in the $10\% - 20\%$ range, particularly as the medium between the upper and bottom patches is air or a material with low permittivity like the scheme in

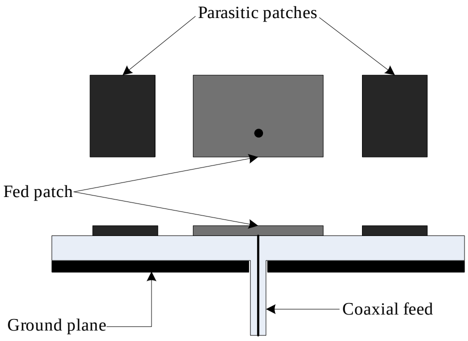

(a) Coplanar coupling scheme

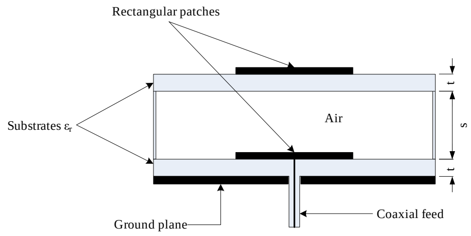

(b) Stacked coupling scheme

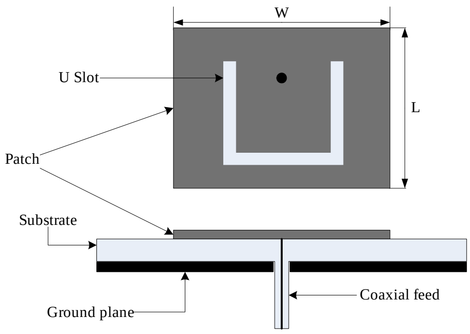

(c) U-slot patch

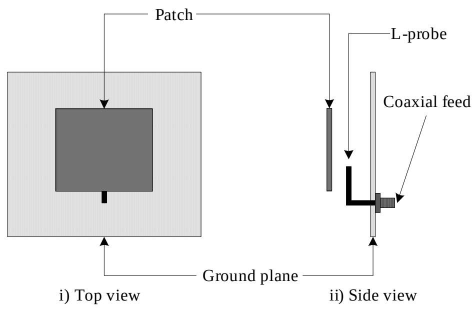

(d) L-probe coupled patch

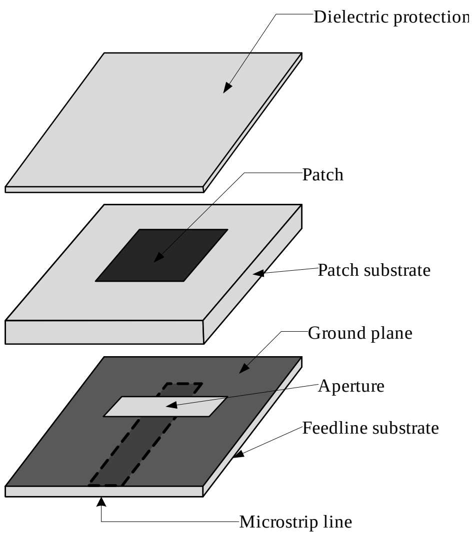

(e) Aperture coupled patch

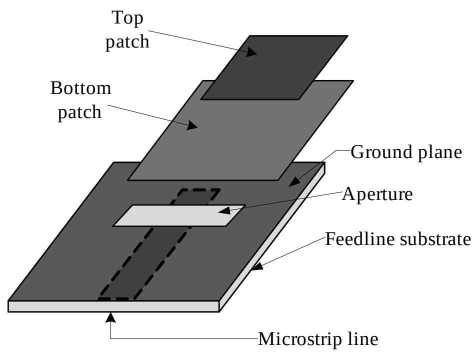

(f) Aperture coupled stacked patches

Figure 3.1 Geometries of various wideband patch antennas

figure 3.1b proposed by Lee et al. in 1987 [14]. Although the thickness in each layer remains thin, the overall thickness is in the range from 0.04 to $0.08\lambda_0$.

In order to increase the gain of the antenna, more than two top elements are stacked right above the bottom one. Other possible arrangements include combining the co-planar and stacked structures for a low-profile design with a broad bandwidth and high gain. Regardless their increased lateral size, stacked microstrip antennas and their variations have been applied widely in practical systems, particularly in arrays.

Figure 3.1c depicts a single layer single patch antenna as reported by Huynh and Lee in 1995 [15]. A long U-shaped slot was cut symmetrically from the plate. The bandwidth of this antenna was in excess of 30%, due to the additional resonances associated with the U-slot, the use of thick substrate of low permittivity, and the capacitance introduced by the U-slot which counters the inductance of the probe. A lot of effort has been devoted to refining this approach. These studies have suggested that a large aspect ratio W/L and a thickness of $h > 0.06\lambda_1$ are essential to attain an impedance bandwidth of $20\% - 40\%$, where λ_1 represents the wavelength corresponding to the lower edge of the bandwidth. One disadvantage is that, at the ends of the frequency bands, the cross polarization is quite high in the H plane.

Slots of other shapes may be used. For example, two L-shaped slots cut symmetrically on the plate were used to achieve an impedance bandwidth 22% [17]. Many studies have shown that cutting long slots of various shapes on the radiator can improve the impedance matching between the feed probe and the patch over a broad frequency range of up to 30%. The impedance matching is sensitive to the size, location and shape of the slots.

The wideband single layer single patch antenna of the figure 3.1d was introduced by Luk et al. in 1998 [18]. It is mainly characterized by a thick substrate of low permittivity and a L-shaped feeding probe. The broad bandwidth observed is attributed to the additional resonance introduced by the L-probe, the use of the specific kind of substrate and the capacitance introduced by the part of the L-probe which is parallel to the patch and the ground plane. This capacitance compensates for the inductance of the perpendicular part of the probe. More than 30% bandwidth is easily achieved with an air or foam substrate of about $0.1\lambda_0$ thickness. Similar to the U-slot patch, the cross-polarization in the H plane caused by the perpendicular arm of the probe is quite high.

Croq and Papiernik [19] proposed a patch antenna fed through an aperture slot by a microstrip line and covered by a dielectric protection as illustrated in 3.1e. If the slot is made to resonant at a frequency close to but not the same as the resonance of the patch, about 25% bandwidth can be obtained. The strong back radiation is a major disadvantage of a resonant slot aperture coupled patch antenna.

Another broadband configuration studied by Targonski et al. [20] consists of two stacked patches of slightly different size, the bottom of which is fed through an aperture by a microstrip line as shown in figure 3.1f. In this design there are three resonators, two patches and the slot. If the antenna parameters are adjusted properly, the introduction of multiple resonances can yield a bandwidth of the order of $50-60\%$. High backlobe radiation due to the resonant slot is the disadvantage of this antenna. Moreover, as it consists of several layers, the overall the antenna is very thick.

3.1.1 Irregularly shaped wideband patch antennas

Investigations have shown that the shape of the radiator affects the impedance bandwidth, even for the same maximum dimensions. Thus, a number of proposed schemes aiming at wideband operation are based on a variety of irregular patch shapes. However, most of the presented outlines originate from conventional shapes (i.e. rectangular) which have been modified by adding slots or/and cutting fragments as well as combining them resulting to new ones. Some examples of such cases are presented below.

A rectangular patch antenna with two parallel slots positioned symmetrically with respect to the feed point was presented in 2001 by Yang *et. al* [21]. As shown in the figure 3.2 the topological shape of the patch resembles the letter 'E'. By adjusting the slot length, width and position the achievable bandwidth can be controlled. In this way, two resonances are introduced in $1.9\,GHz$ and in $2.4\,GHz$ and widened bandwidth reaches 30.3%. The mechanism that explains the extended bandwidth is based on the fact that the slots affect the two resonant frequencies differently. That is to say, the slots control the lower resonant frequency, while the antenna width W controls the higher resonant frequency. So far, many variations of the E-shaped patch antenna have been proposed, leading to wideband operation for different frequency bands.

A ψ-shape microstrip patch antenna, as demonstrated by Sharma and Shafai [22], shows impedance bandwidth leading to 60%. The configuration of the antenna illustrated in figure 3.3, includes a ψ-shape patch on a microwave

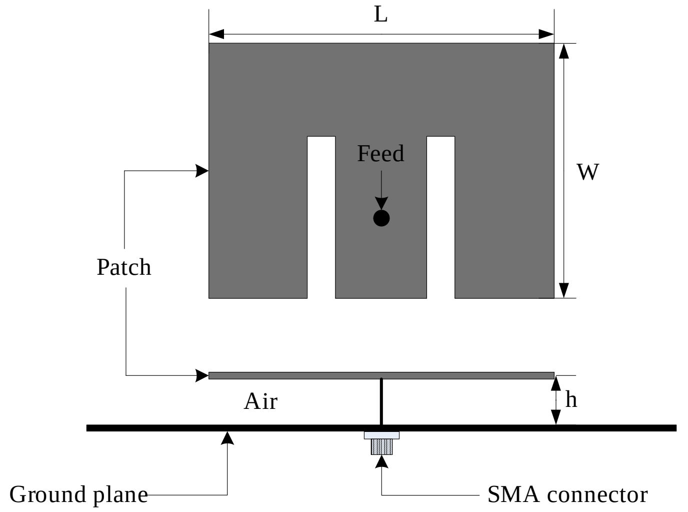

Figure 3.2 Geometry of the E-shaped patch antenna

substrate placed on a foam substrate. A coaxial probe is considered for feeding the patch antenna. According to the simulation results this patch antenna operates from 3.82 to 7.10 GHz. However, while the radiation pattern is acceptable for most of the frequency range, at higher frequency end a dip at the broadside angle is observed since the electrical length of the patch becomes large.

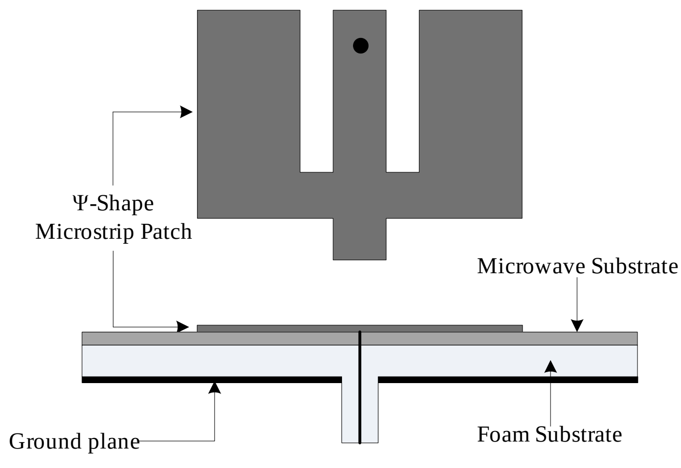

Figure 3.3 The ψ-shape microstrip patch antenna configuration

Furthermore, a number of nature-inspired shapes regarding the realization of wideband patch antennas can be found in the literature. Namely, a flower-shaped microstrip patch antenna, proximity-fed by a semicircle patch which is excited via a coaxial connector (figure 3.4a), operates at around $5\,GHz$ and achieves an impedance bandwidth of approximately 63% ($3.875 - 7.45\,GHz$) [23]. In this group belongs also the star-shaped microstrip patch antenna of the figure 3.4b. The proposed design is capacitively fed by a small rectangular patch and theoretically 63% impedance bandwidth in the frequency range $5 - 9.3\,GHz$ is obtained [24]. A patch antenna suitable for ultra wide band applications has been proposed by Neyestanak [25]. Figure 3.4c illustrates a rose leaf shaped patch which is separated from the ground plane by an air/foam filled substrate in the upper layer. The antenna is capacitively fed via a probe-fed small rectangular patch. The resulting impedance bandwidth is 69% for the frequency band of $4.175 - 8.5\,GHz$. Finally, a more complex star-shaped patch antenna with four shorting posts under the patch and a capacitive diamond shape patch fed, as shown in figure 3.4d, has been presented [26]. The results for this antenna reported an impedance bandwidth of 81% in the range $4 - 8.8\,GHz$.

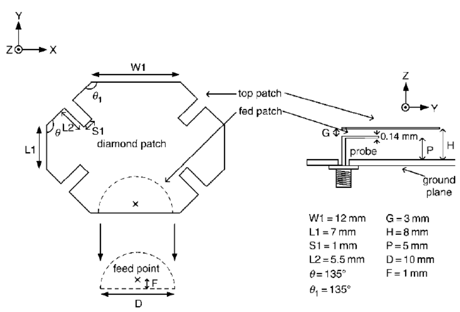

(a) Semicircle-fed flower-shaped microstrip patch antenna

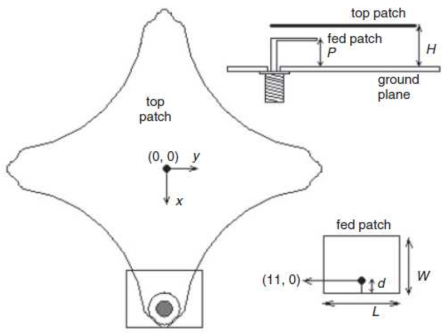

(b) Star-shaped microstrip patch antenna

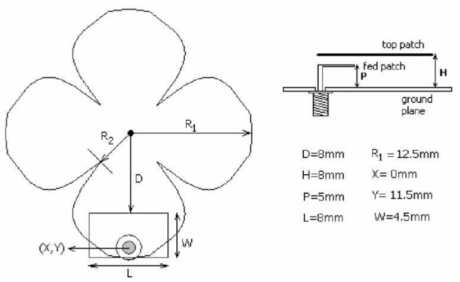

(c) Rose leaf microstrip patch antenna

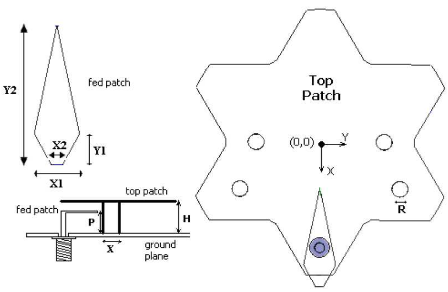

(d) Star-shaped patch antenna with diamond-shaped fed patch

Figure 3.4 Naturally inspired patch shapes

3.2 Dual- and multi- band designs

Many wireless applications, like GSM, UMTS, WLAN, WiMAX, etc., require two or more operating frequency bands. Due to their attractive characteristics, microstrip patch antennas have been considerably investigated with respect to their multi-band operating capabilities. The need for multi-frequency designs yields from the fact that a broadband patch antenna, which possibly covers the desirable frequency bands, receives also superfluous frequencies that have to be filtered out. On the contrary, a dual- and multi-band patch antenna can focus only on the frequencies of interest, so it operates in a more efficient way. A variety of designs that can be found in the literature includes stacked patches, use of dual modes in a patch, slotted patches and fractal patches. Some of these schemes are presented below.

3.2.1 Stacked patches

The scheme of the stacked patches was previously introduced as a broadbanding technique. In that application, the bottom patch was fed while the upper patch was parasitic. This produced strong coupling between the two resonances of the patches, resulting in broadband behaviour. Stacked patches can also be designed for dual-frequency operation. For the coax-fed case, the center conduction passes through a clearance hole in the lower patch and is connected directly to the upper patch. Such an arrangement appears to result in a weak coupling of the two resonances of the two patches, leading to dual-frequency operation.

Long and Walton in 1979 [27] presented the design depicted in figure 3.5, where two stacked circular patches were photo-etched on separate substrates and aligned so that their centers were along the same line. The input impedance and the radiation patterns were evaluated while varying the sizes of the two discs and the spacing between them. It was shown that the system behaves as a pair of two coupled cavities and it features a radiation pattern similar to that of the lowest mode for the single singular patch.

A variation of the above mentioned design is the introduction of air gaps

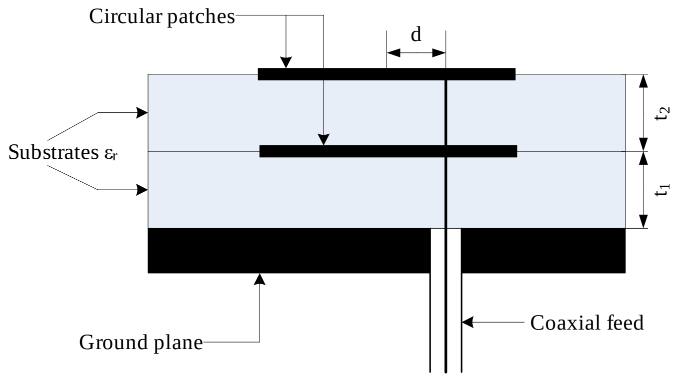

Figure 3.5 Dual-frequency stacked microstrip antenna

between the lowest substrate and/or between the two substrates [28]. It was shown that varying the width of the upper air gap is a convenient method of altering the separation of the frequency bands.

Clearly the technique of using stacked patches can be extended to multi-bands by simply stacking patches in multilayers. Such a case is a five-layered patch antenna consisting of four parasitic patches placed underneath the driven by a coaxial probe patch [29]. This antenna could be operated in five closely packed frequency bands. Apparently, the total size of this arrangement is relatively large.

3.2.2 Multiple modes in a single patch

It is possible for a single patch to operate in dual-band when two modes with similar radiation patterns that have the same polarization can be found. For the rectangular patch, the modes TM_{01} and TM_{03} produce a radiation predominantly in the broadside direction and with the same polarization. Normally, their resonant frequencies are related by a fixed ratio, approximately three. However, it has been demonstrated that, electrically shorting pins if placed on the nodal lines of the TM_{03} mode field could have a strong effect on the TM_{01} mode but not on the TM_{01} mode. According to Zhong and Lo [30], by implementing this method, the separation of the two frequency bands can be changed and also the input impedance of the TM_{01} mode. Specifically, by increasing gradually the number of pins inserted as shown in figure 3.6, the resonant frequency of the TM_{01} mode varies proportionally resulting in a variation of the frequency ratio.

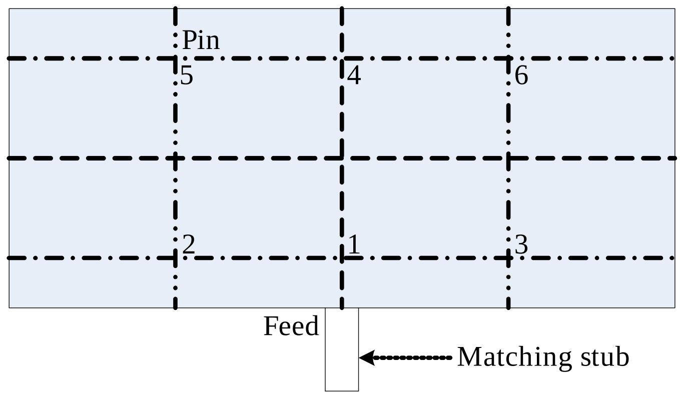

Figure 3.6 Rectangular patch antenna with six possible shorting pins

Similarly, the equilateral triangular patch can be used for triple-band operation [31]. In particular, the cavity model analysis of this antenna shows that the three modes, TM_{10}, TM_{20} and TM_{21} radiate strongly in the broadside radiation. By selecting the location of the coaxial feed properly, good matches can be obtained for all three modes.

3.2.3 Dual- and triple- band patches with slots

If two narrow slots are etched close and alongside to the radiating edges of a rectangular patch as shown in figure 4.5, a dual-band antenna with frequency ratio less than 2 can be obtained. The first band corresponds to the TM_{01} mode and the second one to the TM_{03} mode. The resonant frequency of the second mode decreases since the slots lead to strong modification of the current distribution for this mode, while TM_{01} current distribution is slightly perturbed. This explains the reduction of the frequency band separation. Maci et al. [32] studied this technique and fabricated several prototypes at C- and X- bands.

The U-slot antenna, which was previously introduced for broadbanding reasons, can also operate as a dual- and triple- band antenna if the parameters are appropriately chosen, since the U-slot adds another resonance. To obtain a triple-band operation, a second slot is needed. The dual-band design is achieved by adjusting the U-slot dimensions so that the patch resonance and the slot resonance do not merge to yield a broadband response. This ap-

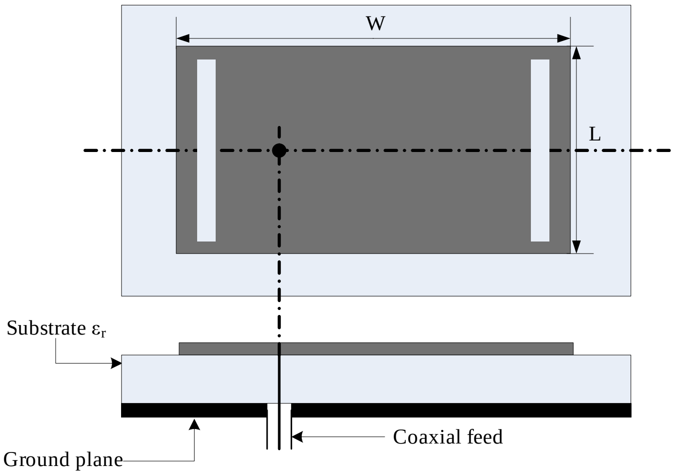

Figure 3.7 Probe feed double slotted patch antenna

proach results in a frequency ratio larger than 1.2. Namely, this antenna can operate at a band centered at $2\,GHz$ and another band centered at $4.8\,GHz$ (figure 3.8a). The patch dimension L determines the lower resonance. To achieve triple-band operation, two slots are necessary. The second slot can be a U-slot or an H-slot that offers better flexibility. The figure 3.8b shows a combination of a U-slot and an H-slot. This configuration can produce resonances at $1.94\,GHz$, $4.12\,GHz$ and $5.44\,GHz$ with bandwidths 2.6%, 9.8% and 10.4% respectively.

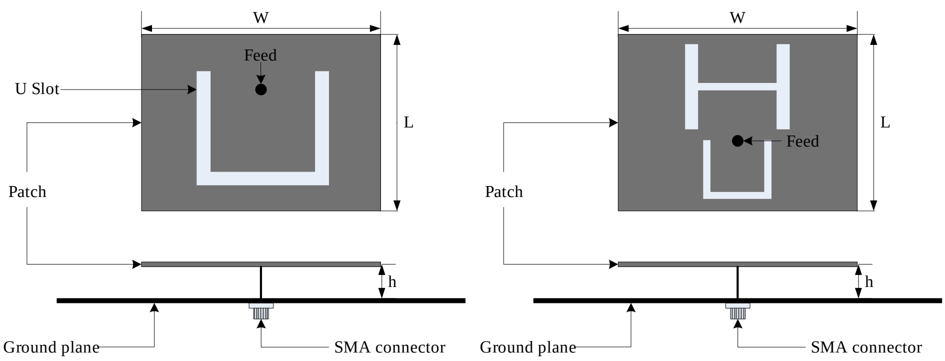

(a) Dual band U-slot patch antenna **(b)** Triple-band U-slot patch antenna

Figure 3.8 Large frequency ratio multi-band designs

A concept employed for obtaining small frequency ratios is to start with a broadband patch antenna, which can be an L-probe coupled patch, the coaxially fed stacked patches or the aperture coupled stacked patches. Such types of prototypes were studied by Lee et al. [35]. Specifically, in the L-probe feed patch antenna of figure 3.1d a U-slot is cut as illustrated in figure 3.9a. In this way a notch is introduced within the broad band and a dual band antenna results. With two U-slots (figure 3.9b), two notches are introduced and a triple-band antenna results. According to the results reported, while the broadband L-probe antenna operates in the frequency range $5.26-7.25\,GHz$, the dual-band design operates in the bands $4.97-5.22\,GHz$ and $5.94-7.26\,GHz$ and the triple-band design in the bands $4.95-5.20\,GHz$, $5.74-6.00\,GHz$ and $6.41-7.24\,GHz$. Apparently, the first U-slot inserts a notch at around $5.5\,GHz$ and the second U-slot at around $6.2\,GHz$.

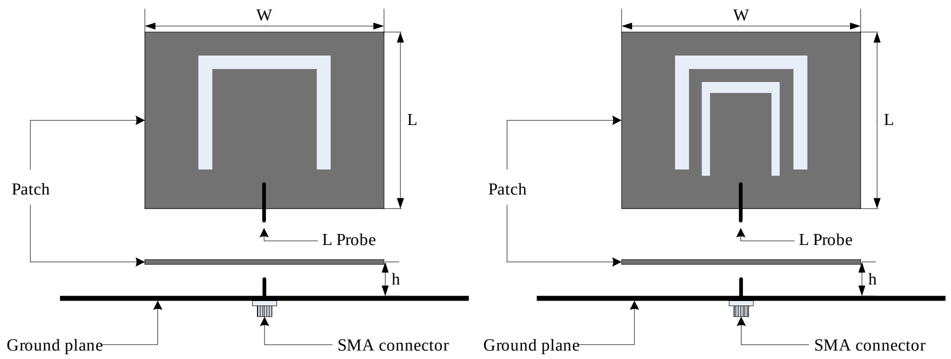

(a) Dual band L-probe slotted patch antenna

(b) Triple-band L-probe slotted patch antenna

Figure 3.9 Small frequency ratio multi-band designs

3.3 Circularly polarized patch antenna designs

An antenna radiates or receives electromagnetic wave into space as a function of direction and polarization. So, the microstrip patch antennas can be investigated also in terms of their polarization properties. So far, the cases presented exhibit linear polarization. However, there are many circumstances, such as multipath/fading environments and in communication with space vehicles above the earth's ionosphere, in which it is not possible to ascertain the polarization of an incoming wave. In such cases, it is more reliable to use circular polarization than linear polarization. Circular and elliptical polarizations can be obtained using various feed arrangements or slight modifications made to the elements. Circular polarization can be obtained if two orthogonal modes are excited with a 90° time-phase difference between them such as in figure 3.10. This can be accomplished by adjusting the physical dimensions of the patch and using either single, or two, or more feeds.

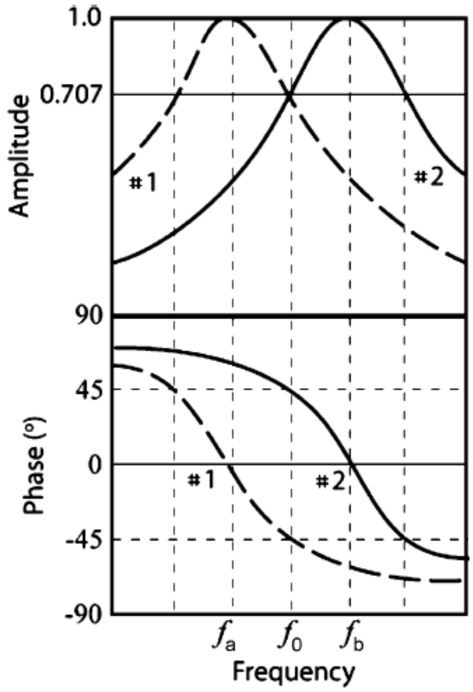

Figure 3.10 The amplitude and phase of two orthogonal modes

3.3.1 Single feed circularly polarized patch antennas

In the single feed category belong the patch antennas of the figure 3.11 which shows an almost square patch, an almost circular patch, a square patch with truncated corners and a circular patch with indentations. The basic principle is that a perturbation of the dimensions is introduced such that, by feeding the patch at the appropriate location, two modes with orthogonal linear polarizations are generated with resonant frequencies which are slightly different. This design is simple, but suffers from very narrow axial ratio bandwidth for thin substrates.

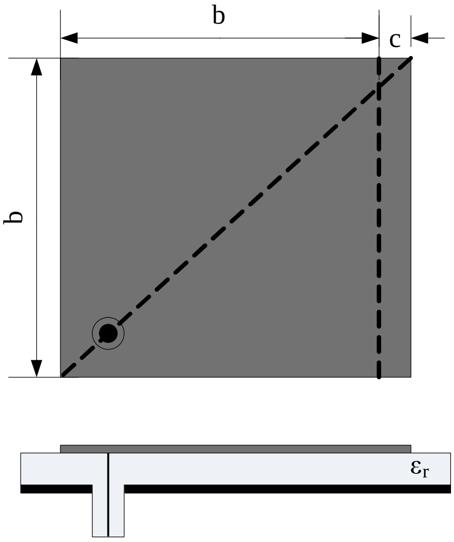

(a) Almost square patch

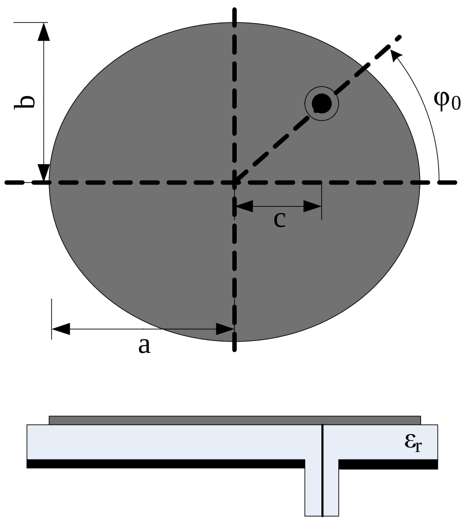

(b) Almost circular (elliptical) patch

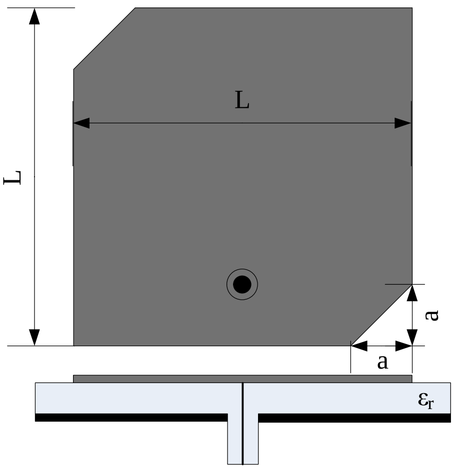

(c) Square patch with truncated corners

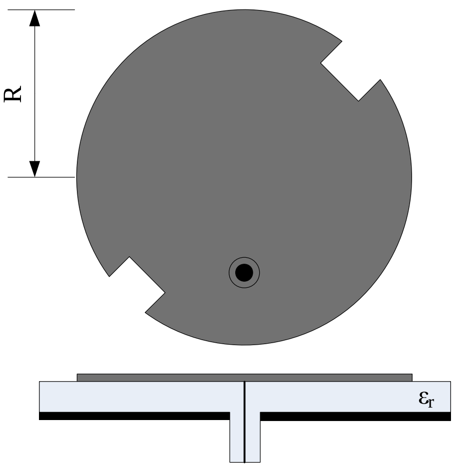

(d) Circular patch with indentations

Figure 3.11 Single feed circularly polarized patches

For the circularly polarized antennas, the axial ratio bandwidth, which is the frequency range for which the axial ratio is smaller than a specified value (usually $3\,dB$), should be within the impedance bandwidth if the antenna is to be useful. It has been shown that increasing the substrate thickness increases not only the impedance bandwidth but also the axial ratio bandwidth. However, this thickness is very limited if the impedance bandwidth and the axial ratio bandwidth should overlap. In order to increase sufficiently the two bandwidths by using thick substrates, the U-slot and the L-probe technique as well as the stacked patches method presented previously can be used.

Specifically, if the case of the square patch with the truncated corners is considered, it was found that although both impedance and axial ratio bandwidth increase with substrate thickness, these two bandwidths do not overlap once the thickness of the substrate exceeds about $0.02\lambda_0$, resulting in a useful frequency band of 0.82%. Yang et al. [36] studied a truncated corner square patch with a symmetric U-slot and showed that the circular polarization bandwidth can be widened to about 5.2% at the center frequency of $4.1\,GHz$ for an air substrate thickness of $0.08\lambda_0$. A asymmetric U-slot etched on a square patch was proposed by Tong et al. [37]. achieving a circular polarization bandwidth of 3.9% at the center frequency of $2.31\,GHz$ for an air substrate thickness of about $0.085\lambda_0$.

Other configurations aiming at improved circular polarization include the use of an E-patch [38], the polarization of which can be made reconfigurable by controlling the length of the slots using diode switches. Also, a dual frequency circularly polarized antenna was realized by stacking two asymmetric U-slot patches [39]. Finally, In another research, the stacking of truncated-corner square patches gave a bandwidth of 17% [40].

3.3.2 Dual feed circularly polarized patch antennas

For thin substrates ($< 0.03\lambda_0$), good circular polarization bandwidth can be obtained by the use of dual-feeds. The basic structure of a dual-feed circularly polarized patch antenna is depicted in figure 3.12. By feeding the two input ports of a dual polarized patch antenna with signals of equal amplitude and quadrature phase difference, two orthogonal modes are excited and an axial ratio bandwidth of 10% is attained [41]. The drawback of this method is the higher complexity in the feed circuitry.

To increase the impedance bandwidth, aperture coupling instead of edge feeding technique is utilized. The patch is either excited by two off-center apertures [42] or two crossed apertures at the ground plane [43]. In both cases the impedance bandwidth is more than 20%. However, in the first case a poor axial ratio bandwidth of around 10% is obtained since each aperture

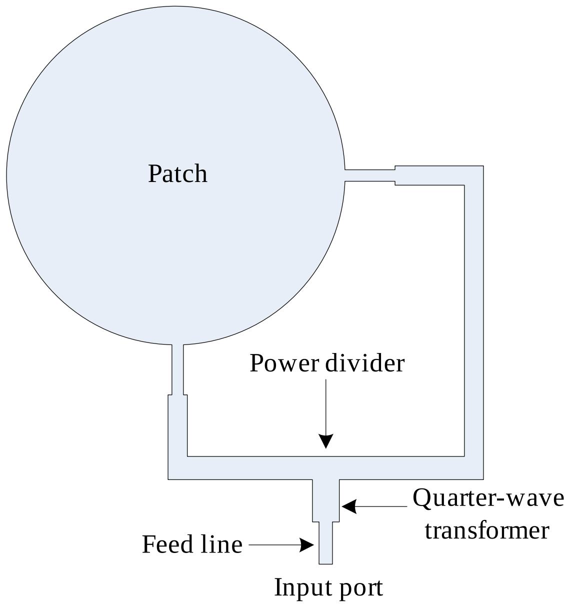

Figure 3.12 Dual feed circularly polarized patch antenna

is fed by a microstrip line causing high coupling between the apertures and high cross-polarization levels. On the other hand, for the crossed apertures, each aperture is fed by a pair of microstrip lines. Therefore, the antenna has a symmetric structure and high isolation is achieved between the apertures. Consequently, the antenna has wide axial ratio bandwidth of 25% to 30%.

The dual-feed design can be extended to multi-feed design. It has been demonstrated that equally feeding a patch at suitable multiple locations with appropriate phasing leads to the cancellation of the cross-circularly polarized components, resulting in improved axial ratio bandwidth.

Chapter 4

Microstrip antenna analysis methods

4.1 Introduction

It was known that the resonant length of a rectangular microstrip antenna is approximately one-half wavelength with the effective dielectric constant of the substrate taken into account. Following the introduction of the microstrip antenna, analysis methods were desired to determine the approximate resonant resistance of a basic rectangular microstrip radiator. The earliest useful model introduced to provide approximate values of resistance at the edge of a microstrip antenna is known as the transmission line model. The transmission line model provides insight into the simplest microstrip antenna design, but is not complete enough to be useful when more than one resonant mode is present. In the late 1970s Lo et. al [44] developed a model of the rectangular microstrip antenna as a lossy resonant cavity. Compared to the transmission line model, the cavity model is more accurate but at the same time more complex. However, it gives good physical insight considering also the excitation of modes which are not along the linear transmission line. Microstrip antennas, despite their simple geometry, proved to be very challenging to analyse using exact methods. In the 1980s, the method of moments (MoM) [45] became the first numerical analysis method that was computationally efficient enough so that contemporary computers could provide enough memory and CPU speed to practically analyse microstrip antennas.

Improvements in computational power and memory size of personal computers during the 1990s made numerical methods such as the finite difference time domain (FDTD) method [46] and finite element method (FEM) [47], which require much more memory than MoM solutions, workable for everyday use by designers. In general, when applied properly, the full-wave models are very accurate, very versatile, and can treat single elements, finite and infinite arrays, stacked elements, arbitrary shaped elements and coupling. However, they are the most complex models and usually give less physical insight.

4.2 The transmission line model

The rectangular patch antenna is very probably the most popular mirostrip antenna design implemented by designers. It is very easy to analyse using both the transmission line and the cavity model, which is most accurate for thin substrates. As it was indicated earlier, the transmission line model is the easiest of all but it yields the least accurate results and it lacks the versatility. However, it does set some physical insight. As it is demonstrated by the cavity model, a rectangular microstrip antenna can be represented by as an array of two radiating narrow apertures, each of width W and height h, separated by a distance L. Rectangular and square patches have a physical shape derived from microstrip transmission lines. Therefore, these antennas can be modeled as sections of transmission lines. Basically, the transmission line model represents the microstrip antenna by two slots, separated by a low impedance Z_c transmission line of length L. The characteristic impedance Z_0 and propagation constant β for the line are determined by the patch size and substrate parameters.

Because the dimensions of the patch are finite along the length and width, the fields at the edges of the patch undergo *fringing*. This is illustrated in figures 4.1b and 4.1c for the two radiating slots of the microstrip antenna. The amount of fringing is a function of the dimensions of the patch and the height of the substrate. Since for microstrip antennas $L/h \gg 1$, fringing is reduced, however, it must be taken into account because it influences the resonant frequency of the antenna. The same applies for the width. In figure 4.1c the non-homogeneous electric field lines are shown. As can be seen, most of the field lines reside in the substrate and parts of some lines exist in air. Fringing in this case makes the microstrip line look wider electrically compared to its physical dimensions. Since some of the waves travel in the

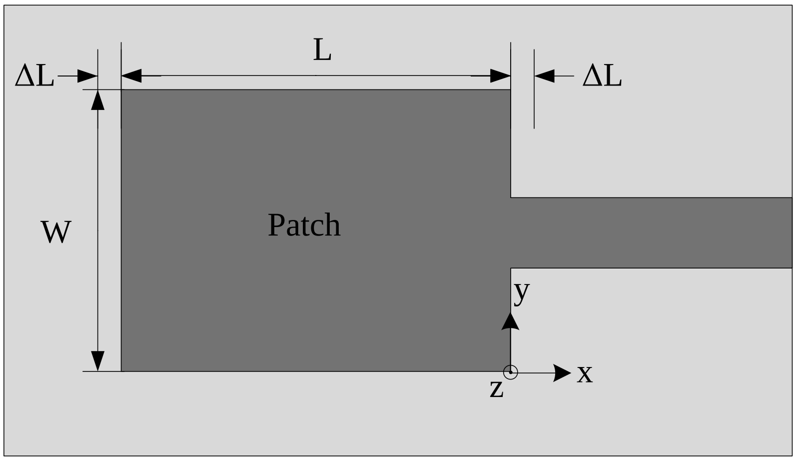

(a) Top view

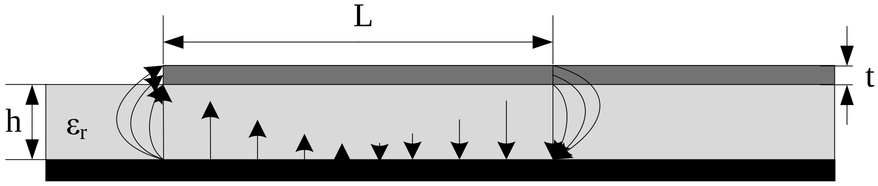

(b) Side view

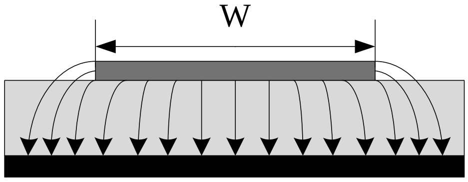

(c) Side view

Figure 4.1 Physical and effective lenghts of rectangular microstrip antenna

substrate and some in the air, an *effective dielectric constant* ϵ_{reff} is introduced to account for fringing and the wave propagation in the line.

The effective dielectric constant is also a function of frequency. As the frequency of operation increases, most of the electric fields lines concentrate in the substrate and therefore the effective dielectric constant approaches the value of the dielectric constant of the substrate. For low frequencies the effective dielectric constant is essentially constant and when $W/h > 1$ its value is given by

$$\epsilon_{\text{reff}} = \frac{\epsilon_r + 1}{2} + \frac{\epsilon_r - 1}{2}\left[1 + 12\frac{h}{W}\right]^{-1/2} \tag{4.2.1}$$

Because of the fringing effects, electrically the patch of the microstrip antenna looks greater than its physical dimensions. For the xz-plane, this is demonstrated in figure 4.1a where the dimensions of the patch along its length have been extended on each and by a distance ΔL, which is a function of the effective dielectric constant ϵ_{reff} and the width to height ratio (W/h). A very popular and practical approximate relation for the normalized extension of the length is

$$\frac{\Delta L}{h} = 0.412\frac{(\epsilon_{\text{reff}} + 0.3)\left(\frac{W}{h} + 0.264\right)}{(\epsilon_{\text{reff}} - 0.258)\left(\frac{W}{h} + 0.8\right)} \tag{4.2.2}$$

Since the length of the patch has been extended by ΔL on each side, the effective length of the patch is now ($L = \lambda/2$ for dominant TM_{010} mode with no fringing)

$$L_{\text{eff}} = L + 2\Delta L \tag{4.2.3}$$

For the dominant mode TM_{010}, the resonant frequency of the microstrip antenna is a function of its length, Usually it is given by

$$(f_r)_{010} = \frac{1}{2L\sqrt{\epsilon_r}\sqrt{\mu_0\epsilon_0}} = \frac{\upsilon_0}{2L\sqrt{\epsilon_r}} \tag{4.2.4}$$

where υ_0 is the speed of light in free space. Since equation 4.3.11 does not account for fringing, it must be modified to include edge effects and should be computed using

$$(f_{rc})_{010} = \frac{1}{2L_{\text{eff}}\sqrt{\epsilon_{\text{reff}}}\sqrt{\mu_0\epsilon_0}} = \frac{1}{2(L + 2\Delta L)\sqrt{\epsilon_{\text{reff}}}\sqrt{\mu_0\epsilon_0}} \tag{4.2.5}$$

The four edges of the patch are classified as radiating type or non-radiating type depending on the field variation along their length. The classification is based on the observation that a radiating edge is associated with slow field variations along its length. For the TM_{10} mode in the patch, the two ends of the antenna located at $x = 0$ and $x = L$ can be viewed as radiating because the electric field is uniform along these edges. The non-radiating edge, on the other hand, should have a integral multiple of half-wave variations along the edge, such that there is an almost complete cancellation of the radiated power from the edge. Therefore, the two edges along the sides of length L are referred to as non-radiating edges because of half-wave variation of the field along these edges.

Each radiating slot at $x = 0, L$ is represented by a parallel equivalent admittance $Y = G + jB$. Here, G is the conductance associated with the power radiated from the edge, and B is the susceptance due to the energy stored in the fringing field near the edge. The effect of the fringing fields at non-radiating edges at $y = 0, W$ is included in the determination of phase constant β. Based on this identification, the equivalent circuit of the rectangular patch antenna is shown in figure 4.2.

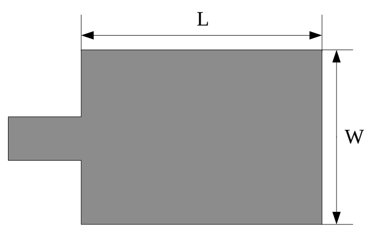

(a) Rectangular patch

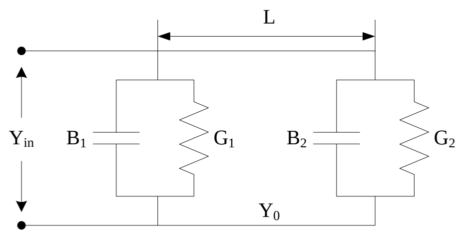

(b) Transmission model equivalent

Figure 4.2 Rectangular patch and its equivalent circuit transmission line model

The radiation patterns of the patch antenna are assumed to be the same as that of an array of two narrow slots separated by a distance equal to the length of the patch. The input admittance of the antenna at the feed port is obtained by transforming the edge admittances to the feed point according to the equation.

$$Y_{in} = Y_1 + Y_0 \frac{Y_2 + jY_0 \tan(\beta L)}{Y_0 + jY_2 \tan(\beta L)} \tag{4.2.6}$$

where Y_1 and Y_2 are the admittances of the first and the second slot respectively, Y_{in} is the input admittance at the the end of the transmission line of length L with characteristic admittance Y_0 and phase constant β. The equivalent conductance and susceptance of a slot of finite width W is given by the expressions.

$$G_1 = \frac{W}{120\lambda_0}\left[1 - \frac{1}{24}(k_0 h)^2\right] \qquad \frac{h}{\lambda_0} < \frac{1}{10} \tag{4.2.7}$$

$$B_1 = \frac{W}{120\lambda_0}\left[1 - 0.636\ln(k_0 h)\right] \qquad \frac{h}{\lambda_0} < \frac{1}{10} \tag{4.2.8}$$

Since the second slot is identical to the first one, its equivalent admittance is

$$Y_2 = Y_1, \quad G_2 = G_1, \quad B_2 = B_1 \tag{4.2.9}$$

Ideally the two slots should be separated by $L = \lambda/2$ where λ is the wavelength in the dielectric (substrate). However, because of fringing the length of the patch is electrically longer than the actual length. Therefore the actual separation of the two slots is slightly less than $\lambda/2$ (typically $0.48\lambda < L < 0.49\lambda$).

4.3 The cavity model

Microstrip antennas resemble dielectric-loaded cavities, and they exhibit higher order resonances. Therefore, the cavity model becomes a natural choice to analyse patch antennas. The cavity model, originated in the late 1970s, views the rectangular microstrip antenna as an electromagnetic cavity with electric walls at the groundplane and the patch, and magnetic walls at each edge to simulate an open circuit. The fields under the patch are the superposition of the resonant modes of this two-dimensional radiator. This is an approximate model, which in principle leads to a reactive input impedance and it does not radiate any power. However, assuming that the actual fields are approximate to those generated by such a model, the computed pattern, input admittance and resonant frequencies compare well with measurements.

To account for radiation, a loss mechanism has to be introduced. To make the microstrip lossy using the cavity model, which would then represent an antenna, the loss is taken into account by introducing an affective loss tangent δ_{eff}. The effective loss tangent is chosen appropriately to represent the loss mechanism of the cavity, which now behaves as an antenna and is taken as the reciprocal of the antenna quality factor Q ($\delta_{eff} = 1/Q$). In this way, the input impedance becomes complex as its real part consists of the radiation resistance R_r and the loss resistance R_L.

The cavity model is based on the following fundamental observations:

- Because the thickness of the microstrip is usually very small, the waves generated within the dielectric substrate (between the patch and the ground plane) undergo considerable reflections when they arrive at the edge of the patch. Therefore only a small fraction of the incident energy is radiated, thus the antenna is considered to be very inefficient.

- The fields beneath the patch form standing waves that can be represented by cosinusoidal wave functions.

- Since the height of the substrate is very small ($h \ll \lambda$ where λ is the wavelength within the dielectric), the field variations along the height are considered constant.

- Because of the very small substrate height, the fringing of the fields along the edges of the patch are also very small whereby the electric field is nearly normal to the surface of the patch. Therefore, only TM^z field configurations will be considered within the cavity.

- While the top and bottom walls of the cavity are perfectly electric conducting, the four side walls will be modelled as perfectly conducting magnetic walls (tangential magnetic fields vanish along those four walls).

In order to apply the theory for cavities and resonators we need to approximate the patch antenna as a dielectric loaded cavity laying between the conductive patch and the ground plane. The dielectric material of the substrate has dielectric constant ϵ_r and it is assumed to be truncated and not extended beyond the edges of the patch. The corresponding antenna geometry is illustrated in figure 4.3.

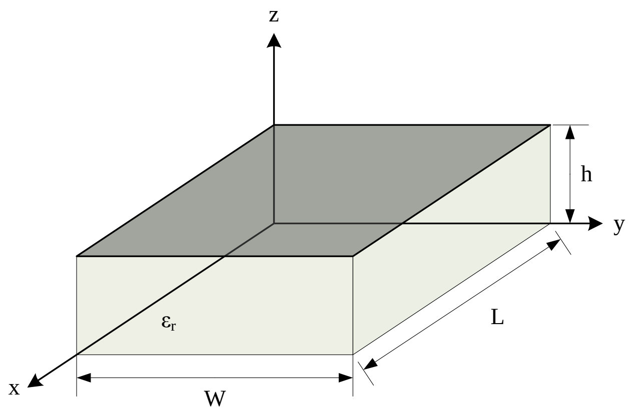

Figure 4.3 Rectangular microstrip patch geometry

For the calculation of the TM^z fields and the other appropriate parameters for the configuration 4.3, the electric vector potential and the magnetic vector potential are expressed as follows

$$\mathbf{A} = \hat{a}_z A_z(x, y, z) \tag{4.3.1a}$$

$$\mathbf{F} = 0 \tag{4.3.1b}$$

The electric vector potential must satisfy the homogeneous wave equation 7.1.1 which is derived from Maxwell's equations for a free source cavity space.

$$\nabla^2 A_z + k^2 A_z = 0 \tag{4.3.2}$$

The solution of the equation 7.1.1 is obtained using the *separation of variables method* and according to that it can be written as

$$A_z(x, y, z) = f(x)g(y)h(z) \tag{4.3.3}$$

For the rectangular cavity, $f(x)$, $g(y)$ and $h(z)$ are taking the appropriate form and equation 4.3.3 is written as

$$\begin{aligned} A_z = & \left[A_1 \cos(k_x x) + B_1 \sin(k_x x)\right] \left[A_2 \cos(k_y y) + B_2 \sin(k_y y)\right] \\ & \cdot \left[A_3 \cos(k_z z) + B_3 \sin(k_z z)\right] \end{aligned} \tag{4.3.4}$$

where k_x, k_y and k_z are the wavenumbers along the x, y and z direction respectively. The electric and magnetic fields within the cavity can be expressed with respect to A_z as follows.

$$
\begin{aligned}
E_x &= -j\frac{1}{\omega\mu\epsilon}\frac{\partial^2 A_z}{\partial x \partial z} & H_x &= \frac{1}{\mu}\frac{\partial A_z}{\partial y} \\
E_y &= -j\frac{1}{\omega\mu\epsilon}\frac{\partial^2 A_z}{\partial y \partial z} & H_y &= \frac{1}{\mu}\frac{\partial A_z}{\partial x} \\
E_z &= -j\frac{1}{\omega\mu\epsilon}\left(\frac{\partial^2}{\partial z^2}+k^2\right)A_z & H_z &= 0
\end{aligned}
\tag{4.3.5}
$$

Due to the boundary conditions imposed by the electric and magnetic wall assumptions

$$
\begin{aligned}
&E_x(0 \leqslant x' \leqslant L,\, 0 \leqslant y' \leqslant W,\, z' = 0) \\
&= E_x(0 \leqslant x' \leqslant L,\, 0 \leqslant y' \leqslant W,\, z' = h) = 0 \\
\\
&H_x(0 \leqslant x' \leqslant L,\, y' = 0,\, 0 \leqslant z' \leqslant h) \\
&= H_x(0 \leqslant x' \leqslant L,\, y' = W,\, 0 \leqslant z' \leqslant h) = 0 \\
\\
&H_y(x' = 0,\, 0 \leqslant y' \leqslant W,\, 0 \leqslant z' \leqslant h) \\
&= H_y(x' = L,\, 0 \leqslant y' \leqslant W,\, 0 \leqslant z' \leqslant h)
\end{aligned}
\tag{4.3.6}
$$

where x', y', z' represent the coordinates within the cavity, $B_1 = B_2 = B_3 = 0$ and the vector potential in equation 4.3.4 is getting the form

$$
A_z = A_{mnp}\cos(k_x x')\cos(k_y y')\cos(k_z z') \tag{4.3.7}
$$

where A_{mnp} represents the amplitude coefficients of each mnp mode. The wavenumbers k_x, k_y, k_z are equal to

$$
\begin{aligned}
k_x &= \frac{m\pi}{L}, & m &= 0, 1, 2, \ldots \\
k_y &= \frac{n\pi}{W}, & n &= 0, 1, 2, \ldots \\
k_z &= \frac{p\pi}{h}, & p &= 0, 1, 2, \ldots
\end{aligned}
\tag{4.3.8}
$$

provided that $m = n = p \neq 0$. The values of m, n, p represent, respectively, the number of half-cycle field variations along the x, y, z directions. The wavenumbers k_x, k_y and k_z are satisfying the equation

$$
k_x^2 + k_y^2 + k_z^2 = \left(\frac{m\pi}{L}\right)^2 + \left(\frac{n\pi}{W}\right)^2 + \left(\frac{p\pi}{h}\right)^2 = k_{mn}^2 = \omega^2\mu\epsilon \tag{4.3.9}
$$

However, it was assumed that the substrate thickness h is very small compared to W and L, thus, the field along the z direction is relatively constant. This leads to the conclusion that $E_x = E_y = 0$. Therefore, accounting 4.3.7, the reduced 4.3.5 can be written as

$$\begin{aligned} E_z &= -j\frac{k_x^2 + k_y^2}{\omega\mu\epsilon} A_{mn}\cos\left(k_x x'\right)\cos\left(k_y y'\right) \\ H_x &= -\frac{k_y}{\mu} A_{mn}\cos\left(k_x x'\right)\sin\left(k_y y'\right) \\ H_y &= \frac{k_x}{\mu} A_{mn}\sin\left(k_x x'\right)\cos\left(k_y y'\right) \end{aligned} \tag{4.3.10}$$

The resonant frequencies of the cavity are determined from the equation 4.3.9 considering $p = 0$ as follows

$$f_r^{mn} = \frac{1}{2\pi\sqrt{\mu\epsilon}}\sqrt{\left(\frac{m\pi}{L}\right)^2 + \left(\frac{n\pi}{W}\right)^2} \tag{4.3.11}$$

If $L > W > h$, the dominant mode (mode with the lowest order resonant frequency) is the TM_{10}. If in addition $L > W > L/2 > h$ the next higher order mode is the TM_{01}. If, however, $L > L/2 > W > h$, the second order mode is the TM_{20} instead of TM_{01}. Nevertheless, the fringing effects and their influence should be taken into account in the determination of k_x and k_y and consequently in the evaluation of the resonant frequencies. Therefore, 4.3.9 and 4.3.11 are modified in the following way

$$k_{mn}^2 = k_x^2 + k_y^2 = \left(\frac{m\pi}{L_{\text{eff}}}\right)^2 + \left(\frac{n\pi}{W_{\text{eff}}}\right)^2 \tag{4.3.12}$$

$$f_r^{mn} = \frac{1}{2\pi\sqrt{\mu\epsilon}}\sqrt{\left(\frac{m\pi}{L_{\text{eff}}}\right)^2 + \left(\frac{n\pi}{W_{\text{eff}}}\right)^2} \tag{4.3.13}$$

where $L_{\text{eff}} = L + 2\Delta L$ and $W_{\text{eff}} = W + 2\Delta W$. The extensions ΔL and ΔW are calculated according to 4.2.2.

For the real case of a patch excited by a coaxial feed probe the field is a superposition of all TM_{mn} modes and therefore the z-directed electric field will be

$$E_z(x, y) = \sum_{m=0}^{\infty}\sum_{n=0}^{\infty} A_{mn} e_{mn}(x, y) \tag{4.3.14}$$

where A_{mn} are the mode amplitude coefficient and e_{mn} are the z-directed orthonormalized electric field mode vectors.

$$A_{mn} = j\omega\mu \frac{\langle J_z, e_{mn}\rangle}{\langle e_{mn}, e_{mn}\rangle}\left(\frac{1}{k_{\text{eff}}^2 - k_{mn}^2}\right) \tag{4.3.15}$$

$$e_{mn} = \cos\left(\frac{m\pi x}{L_{\text{eff}}}\right)\cos\left(\frac{n\pi y}{W_{\text{eff}}}\right) \tag{4.3.16}$$

In 4.3.15, the wavenumber k has been substituted by the effective wavenumber k_{eff} in order to introduce the loss factor which accounts also for the radiation of the patch antenna. All losses are lumped into the *effective dielectric loss* with effective tangent loss δ_{eff} and the effective wavenumber is given by

$$k_{\text{eff}}^2 = \epsilon_r(1 - j\delta_{\text{eff}})k_0^2 \tag{4.3.17}$$

The effective loss tangent for the cavity is $\delta_{\text{eff}} = 1/Q_T$, where Q_T is the total quality factor.

We assume that the excitation current J_0 is a $z-$directed current probe I_0 of small rectangular cross-section (d_x, d_y) at the point (x_0, y_0) and zero elsewhere. Because the electric field is assumed to be constant along the z direction, the voltage at the feed point results from the multiplication of 4.3.14 with the substrate thickness h. So, the input impedance is given by the relation

$$Z_{in} = \frac{V_{in}}{I_0} = j\sqrt{\frac{\mu}{\epsilon}}\frac{k_{\text{eff}}h}{W_{\text{eff}}L_{\text{eff}}}\sum_{m=0}^{\infty}\sum_{n=0}^{\infty}\frac{\delta_m\delta_n}{k_{mn}^2 - k_{\text{eff}}^2}C_{mn} \tag{4.3.18}$$

$$C_{mn} = \cos^2\left(\frac{m\pi x_0}{L_{\text{eff}}}\right)\cos^2\left(\frac{n\pi y_0}{W_{\text{eff}}}\right)\text{sinc}\left(\frac{m\pi d_x}{2L_{\text{eff}}}\right)\text{sinc}\left(\frac{n\pi d_y}{2W_{\text{eff}}}\right) \tag{4.3.19}$$

$$\delta_i = \begin{cases} 1 \text{ if } i = 0 \\ 2 \text{ if } i \neq 0 \end{cases} \tag{4.3.20}$$

According to the field equivalence principle (Huygens' principle) the four slots of the microstrip patch are represented by an equivalent electric current density $\mathbf{J}_s$ and an equivalent magnetic current density $\mathbf{M}_s$.

$$\mathbf{J}_s = \hat{\mathbf{n}} \times \mathbf{H}_a \tag{4.3.21}$$

$$\mathbf{M}_s = -\hat{\mathbf{n}} \times \mathbf{E}_a \tag{4.3.22}$$

where $\mathbf{E}_a$ and $\mathbf{H}_a$ represent, respectively, the electric and magnetic fields at the slots. Because it was argued that the tangential magnetic fields along the edges of the patch are very small, ideally zero, we set $\mathbf{J}_s = 0$. Due to the presence of the ground plane, the image theory states that the equivalent magnetic current density will double.

$$\mathbf{M}_s = -2\hat{\mathbf{n}} \times \mathbf{E}_a \tag{4.3.23}$$

Assuming that the dominant mode within the cavity is the TM_{10}, the configuration of the electric field and the equivalent magnetic current densities are illustrated in figure 4.4. The equivalent magnetic current densities along the two slots, each of width W and height h, are both of the same magnitude and of the same phase (figure 4.4a). The equivalent magnetic current density at each slot according to 4.3.23 is

$$\mathbf{M}_1 = -2\hat{\mathbf{x}} \times E_z\hat{\mathbf{z}} = 2E_z\hat{\mathbf{y}} \tag{4.3.24a}$$
$$\mathbf{M}_2 = -2(-\hat{\mathbf{x}}) \times E_z(-\hat{\mathbf{z}}) = 2E_z\hat{\mathbf{y}} \tag{4.3.24b}$$

Thus these two sources will add in a direction normal to the patch forming a broadside pattern. The equivalent current densities for the other two slots, each of length L and height h, are of the same magnitude but opposite direction as shown in figure 4.4b, thus, they cancel each other along the principal planes. So, while there are a total of four slots representing the microstrip antenna, only two account for most of the radiation. Therefore the two slots, separated by the length of the patch L, are referred as *radiating* slots and they a two-element array with a spacing of $\lambda/2$ between the elements. The other two are referred as *non-radiating* slots.

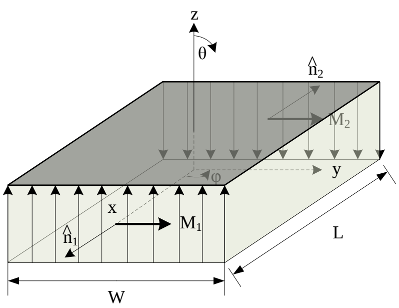

(a) Radiating slots

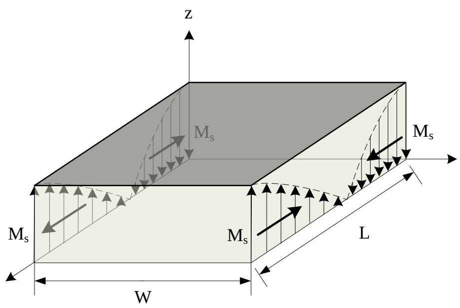

(b) Non-radiating slots

Figure 4.4 Rectangular patch slots and its equivalent magnetic current densities

The calculation of the radiation pattern for the TM_{10} mode is performed by modelling the antennas as a combination of two parallel slots of length W, width h and spaced a distance L apart, as depicted in figure 4.5.

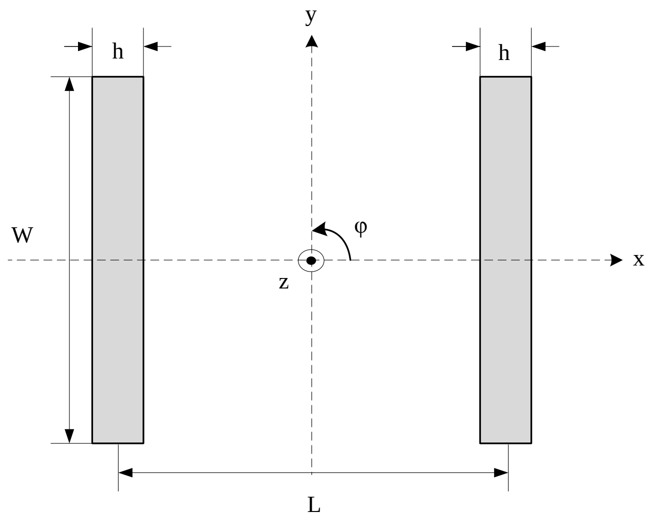

Figure 4.5 Two-slot model of a rectangular patch antenna for determining the radiation patterns

The total field is the sum of a two-element array with each element representing one of the slots. Since the slots are identical, this is accomplished by using an array factor for the two slots. The far-zone electric fields radiated by each slot, using the equivalent current densities of 4.3.24 are written as

$$E_\theta = jk_0 E_0 hW \frac{e^{jk_0 r}}{2\pi r} \cos\phi F \tag{4.3.25}$$

$$E_\phi = -jk_0 E_0 hW \frac{e^{jk_0 r}}{2\pi r} \cos\theta \sin\phi F \tag{4.3.26}$$

where

$$F = \operatorname{sinc}\left(\frac{k_0 h}{2} \sin\theta\cos\phi\right) \operatorname{sinc}\left(\frac{k_0 W}{2} \sin\theta \sin\phi\right) \tag{4.3.27}$$

The total field radiated by the two slots is derived by multiplying the above relations with the array factor

$$AF = 2\cos\left(\frac{k_0 L}{2}\sin\theta\cos\phi\right) \tag{4.3.28}$$

Equations 4.3.25 - 4.3.28 yield the following expressions for the radiation field in the principal planes of a rectangular microstrip antenna operated in the TM_{10} mode.

For the $\phi = 0°$ plane or E-plane:

$$E_\phi(\theta) = 0 \tag{4.3.29}$$

$$E_\theta(\theta) = jk_0E_0hW\frac{e^{jk_0r}}{\pi r}\mathrm{sinc}\left(\frac{k_0h}{2}\sin\theta\right)\cos\left(\frac{k_0L}{2}\sin\theta\right) \tag{4.3.30}$$

For the $\phi = 90°$ plane or H-plane:

$$E_\theta(\theta) = 0 \tag{4.3.31}$$

$$E_\phi(\theta) = -jk_0E_0hW\frac{e^{jk_0r}}{\pi r}\mathrm{sinc}\left(\frac{k_0W}{2}\sin\theta\right)\cos\theta \tag{4.3.32}$$

4.4 The finite integration technique (FIT)

The *finite integration technique* is a numerical method which provides a universal spatial discretization scheme, applicable to a variety of electromagnetic field problems with arbitrary geometries in time or frequency domain. It was developed in 1977 by Weiland [48] and it can be viewed as a generalization of the finite-diffence time-domain (FDTD) method. In principle, FIT creates a set of sparse matrix equations after discretizing the integral form of Maxwell's equations.

$$\begin{aligned}
&\oint_C \mathbf{E}\cdot\mathrm{d}l = -\frac{\partial}{\partial t}\iint_S \mathbf{B}\cdot\mathrm{d}S \qquad &&\oint_C \mathbf{H}\cdot\mathrm{d}l = \frac{\partial}{\partial t}\iint_S \mathbf{D}\cdot\mathrm{d}S + \iint_S \mathbf{J}\cdot\mathrm{d}S\\
&\oint_S \mathbf{D}\cdot\mathrm{d}S = \iiint_V \rho\cdot\mathrm{d}V &&\oint_S \mathbf{B}\cdot\mathrm{d}S = 0
\end{aligned} \tag{4.4.1}$$

The domain of interest is spatially divided into several elementary grid cells of volume V, creating in this way a suitable mesh system G which encloses the considered application problem. Apart from the initial grid system, another one $\tilde{G}$, orthogonally set up to the first one, is introduced. Then, Maxwell's equations and the constitutive relations are mapped onto this dual grid system $G, \tilde{G}$. The grid nodes are enumerated along the grid coordinates u, v and w by $P(p, q, r)$, where $0 \leq p \geq P$, $0 \leq q \geq Q$ and $0 \leq r \geq R$, with total number of nodes $N = (P-1)(Q-1)(R-1)$.

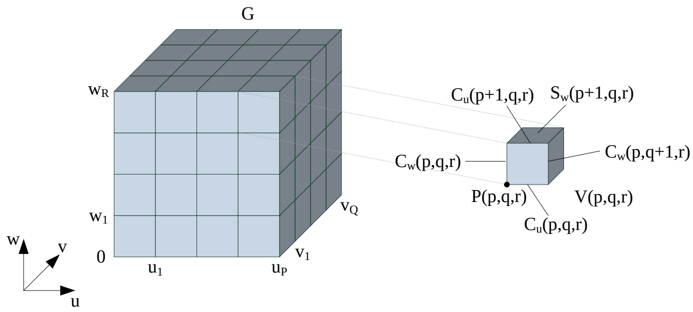

Figure 4.6 Example of a primary grid cell G in cartesian coordinates

The dual grid $\tilde{G}$ has the same volume as G and the same borders and is defined such that each point $\tilde{P}(p,q,r)$ of $\tilde{G}$ is located exactly in the center of one volume $V(p,q,r)$ of G, and vice versa, each point $P(p,q,r)$ is located inside $\tilde{V}(p,q,r)$ of $\tilde{G}$. The spatial discretization of Maxwell's equations is finally performed on this two orthogonal grid systems. The electric grid voltages $\mathbf{e}$ and the magnetic facet fluxes $\mathbf{b}$ are allocated on the primary grid G, whereas, the the magnetic grid voltages $\mathbf{h}$ as well as the electric facet fluxes $\mathbf{j}$ on the dual grid $\tilde{G}$.

$$\begin{aligned} \mathbf{e}(p,q,r) &= \int\limits_{C(p,q,r)} \mathbf{E}\cdot \mathrm{d}l \quad & \mathbf{b}(p,q,r) &= \iint\limits_{S(p,q,r)} \mathbf{B}\cdot \mathrm{d}S \\ \mathbf{h}(p,q,r) &= \int\limits_{\tilde{C}(p,q,r)} \mathbf{H}\cdot \mathrm{d}l \quad & \mathbf{j}(p,q,r) &= \iint\limits_{\tilde{S}(p,q,r)} \mathbf{J}\cdot \mathrm{d}S \end{aligned} \tag{4.4.2}$$

At this point, it is necessary to define the topological matrices $\mathbf{C}$ and $\mathbf{S}$ which correspond to the discrete equivalent of the curl and the divergence operator respectively belonging to the primary grid. Regarding the dual grid, $\tilde{\mathbf{C}}$ and $\tilde{\mathbf{S}}$ are the corresponding operators. These matrix operators just consist of elements $'0'$, $'1'$ and $'-1'$, representing merely topological information.

Considering Faraday's law, the closed integral on the equation's left side can be rewritten as a sum of four grid voltages. Consequently, the time derivative of the magnetic flux defined on the enclosed primary cell facet represents the right-hand side of the equation. By repeating this procedure for all available cell facets, the calculation rule can be summarized in a matrix

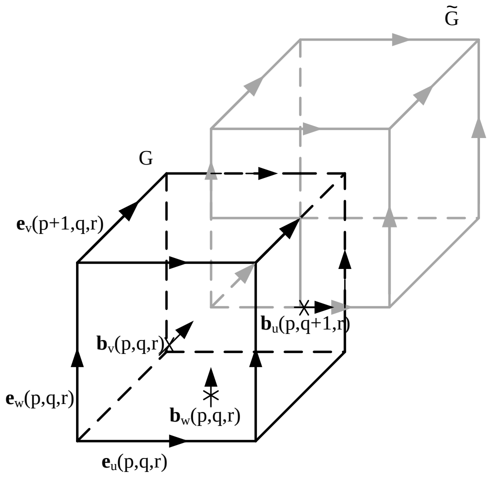

Figure 4.7 Spatial allocation of electric and magnetic field values on the staggered grid doublet $\{G, \tilde{G}\}$

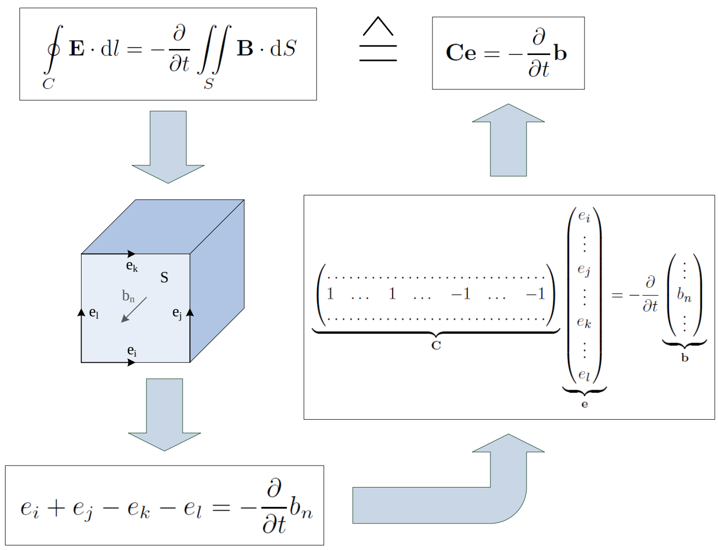

Figure 4.8 Matrix formulation of Maxwell's equations

formulation.

$$\oint_C \mathbf{E} \cdot \mathrm{d}l = -\frac{\partial}{\partial t} \iint_S \mathbf{B} \cdot \mathrm{d}S \qquad \Rightarrow \qquad \mathbf{Ce} = -\frac{d}{dt}\mathbf{b} \tag{4.4.3a}$$

$$\oint_{\tilde{C}} \mathbf{H} \cdot \mathrm{d}l = \frac{\partial}{\partial t} \iint_{\tilde{S}} \mathbf{D} \cdot \mathrm{d}S + \iint_{\tilde{S}} \mathbf{J} \qquad \Rightarrow \qquad \tilde{\mathbf{C}}\mathbf{h} = \frac{d}{dt}\mathbf{d} + \mathbf{j} \tag{4.4.3b}$$

$$\oint_{\tilde{S}} \mathbf{D} \cdot \mathrm{d}S = \iiint_V \rho \cdot \mathrm{d}V \qquad \Rightarrow \qquad \tilde{\mathbf{S}}\mathbf{d} = \mathbf{q} \tag{4.4.3c}$$

$$\oint_S \mathbf{B} \cdot \mathrm{d}S = 0 \qquad \Rightarrow \qquad \mathbf{Sb} = 0 \tag{4.4.3d}$$

The approximation of the Finite Integration Method appears in fact when the integrated voltage and flux variables allocated at two different grids have to be related to each other by the constitutive material relations. By defining the necessary relations between voltages and fluxes their integral values have to be approximated over the grid edges and cell areas, respectively. Consequently, the resulting coefficients depend on the averaged material parameters as well as on the spatial resolution of the grid and are summarized again in correspondent matrices:

$$\begin{aligned} \mathbf{D} &= \varepsilon\,\mathbf{E} & & & \mathbf{d} &= \mathbf{M}_\varepsilon\,\mathbf{e} \\ \mathbf{B} &= \mu\,\mathbf{H} & &\Rightarrow & \mathbf{b} &= \mathbf{M}_\mu\,\mathbf{h} \\ \mathbf{J} &= \sigma\,\mathbf{E} + \mathbf{J}_s & & & \mathbf{j} &= \mathbf{M}_\sigma\,\mathbf{e} + \mathbf{j}_s \end{aligned} \tag{4.4.4}$$

In the above relations (4.4.4), $\mathbf{M}_\varepsilon$, $\mathbf{M}_\mu$ and $\mathbf{M}_\sigma$ are the material matrices representing the discrete permittivity, permeability and conductivity matrices respectively.

The solution of the space discretized set of Maxwell's Grid Equations, in which the time derivatives are substituted by central differences yields the explicit update formulation for the loss-free case:

$$\mathbf{e}^{n+1/2} = \mathbf{e}^{n-1/2} + \Delta t\,\mathbf{M}_\varepsilon^{-1}\left[\tilde{\mathbf{C}}\mathbf{M}_\mu^{-1}\mathbf{b}^n + \mathbf{j}_S^n\right] \tag{4.4.5}$$

$$\mathbf{b}^{n+1} = \mathbf{b}^n - \Delta t\,\mathbf{C}\mathbf{e}^{n+1/2} \tag{4.4.6}$$

Regarding the relations above, the calculation variables are given by the electric voltages and the magnetic fluxes. Both unknowns are located alternately in time, as in the well-known leap-frog scheme, as demonstrated in figure 3. For example, the magnetic flux at $t = (n+1)\Delta t$ is computed from the mag-

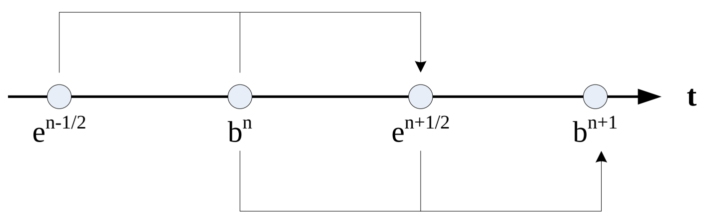

Figure 4.9 Time illustration of the solutions of the electric voltages and the magnetic fluxes

netic flux at the previous time step $t = n\Delta t$ and from the electric voltage at half time step before, at $t = (n+1/2)\Delta t$.

Chapter 5

The patch shaping and the super-shape formula

5.1 Input impedance of a microstrip patch

In general, a microstrip patch antenna is considered as a resonant device and as such for a single isolated mode, it can be represented by a equivalent R-L-C parallel resonant circuit with a series L_p inductance which accounts for the feeding probe reactance as shown in figure 5.1.

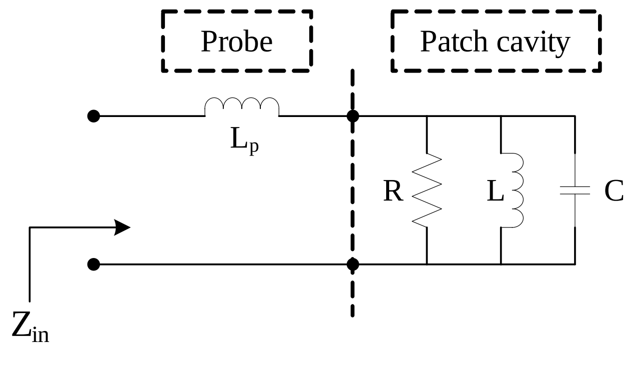

Figure 5.1 Equivalent circuit of a patch antenna

The input impedance is complex and involves a resistive and reactive part. These resistive and reactive components vary as a function of frequency and are symmetric around the resonant frequency. The input impedance near resonance is then given by

$$Z_{in} = R_{in} + jX_{in} \tag{5.1.1}$$

which can be expanded as

$$Z_{in} = \frac{R_r}{1 + Q_T^2\left(\frac{f}{f_{r,nm}} - \frac{f_{r,nm}}{f}\right)^2} + j\left[X_f - \frac{R_r Q_T\left(\frac{f}{f_{r,nm}} - \frac{f_{r,nm}}{f}\right)}{1 + Q_T^2\left(\frac{f}{f_{r,nm}} - \frac{f_{r,nm}}{f}\right)^2}\right] \tag{5.1.2}$$

where R_r is the input resistance at resonance, Q_T is the total quality factor of the resonator, $f_{r,nm}$ is the resonant frequency of the mode nm and X_f is the feed reactance which accounts for the reactance contributed by the feed for probe-fed microstrip antennas. The total quality factor Q_T of the resonator is given is given as

$$Q_T = \left[\frac{1}{Q_{rad}} + \frac{1}{Q_{con}} + \frac{1}{Q_{dlc}} + \frac{1}{Q_{sw}}\right]^{-1} \tag{5.1.3}$$

where Q_{rad}, Q_{con}, Q_{dlc} and Q_{sw} account for quality factors associated with losses caused by radiation, conductivity of the patch, substrate dielectric and surface wave, respectively.

A typical variation of the resistive and reactive part of the input impedance is shown in figure 5.2.

Typically, the feed reactance is very small, compared to the resonant resistance, for very thin substrates. However, for thick elements, the contribution of the equivalent inductance to the input impedance becomes significant and produces a larger and larger mismatch, until the patch antenna can no longer be matched by simply choosing an appropriate feed point location. At resonance the input impedance of the patch should be real with R_{in} reaching the maximum value, and hence the reactive part of Z_{in} should ideally be zero. Practically, as shown in figure 5.2, the input impedance at the resonance has a non-zero reactive component because of the inductance introduced by the feeding probe.

A formula that has been suggested to approximate the feed reactance is

$$X_f \simeq -\frac{\eta k h}{2\pi}\left[\ln\left(\frac{kd}{4}\right) + 0.577\right] \tag{5.1.4}$$

where h is the substrate thickness and d the diameter of the feed probe.

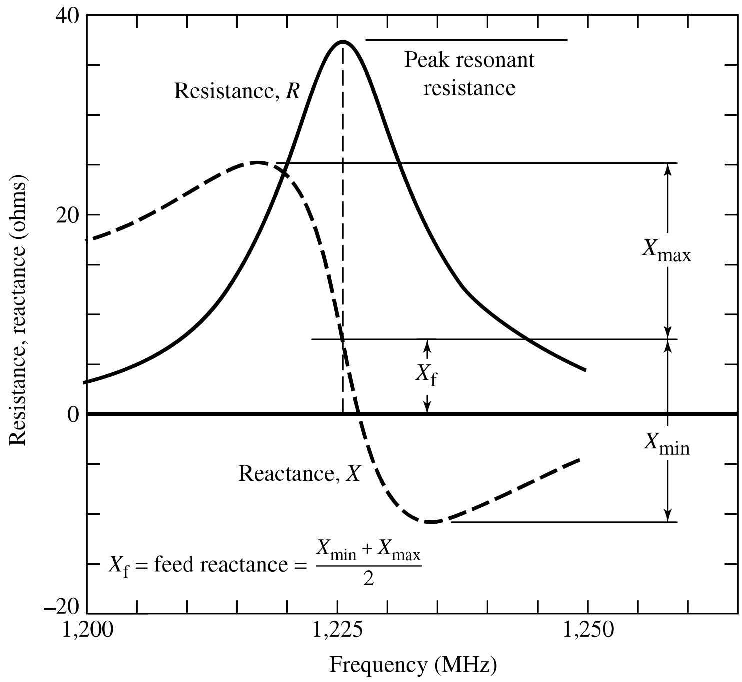

Figure 5.2 Typical variation of resistance and reactance of rectangular microstrip antennas versus frequency

5.2 The impedance bandwidth

If the antenna can be well matched to its feed across a certain frequency range, that frequency range is defined as its *impedance bandwidth*. The impedance bandwidth can be specified in terms of *return loss* ($|S_{11}|$) or a *voltage standing wave ratio* ($VSWR$) over a frequency range. The well-matched impedance bandwidth must totally cover the required operating frequency range for some specified level, such as $VSWR = 2$ or a return loss $|S_{11}|$ of less than $-10\,dB$.

The fractional bandwidth of a microstrip antenna can be written as

$$FBW = \frac{f_H - f_L}{f_C} \tag{5.2.1}$$

where f_H and f_L are the upper and the lower frequency of the frequency range respectively and f_C is the central frequency of the band. Furthermore, the impedance bandwidth is inversely proportional to the *quality factor* (Q_t)

of the antenna and it is given by

$$FBW = \frac{1}{Q_t} \tag{5.2.2}$$

A modified form of 5.2.2 that takes into account the impedance matching is

$$FBW = \frac{VSWR - 1}{Q_t\sqrt{VSWR}} \tag{5.2.3}$$

The radiation efficiency of an antenna is defined as the power radiated over the input power. It can also be expressed in terms of the quality factors, which for a microstrip antenna can be written as

$$e_{cdsw} = \frac{1/Q_{rad}}{1/Q_t} = \frac{Q_t}{Q_{rad}} \tag{5.2.4}$$

where Q_t is given by expression 5.1.3. Typical variations of the efficiency as a function of the substrate height for a microstrip antenna, with two different substrates, are shown in figure 5.3

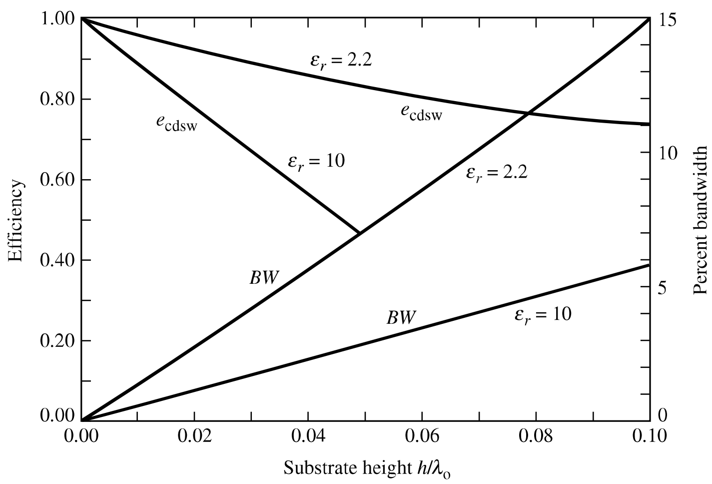

Figure 5.3 Efficiency and bandwidth versus substrate height at constant resonant frequency for rectangular microstrip patch for twodifferent substrates

The quality factor, bandwidth and efficiency characterize the performance of an antenna and they are interrelated in such a way that there is no complete freedom to independently optimize each one. Therefore, there is always a trade-off between them in arriving at an optimum antenna performance.

Microstrip antennas are inherently narrowband. The typical bandwidth of a microstrip antenna is around 4% to 7%. This is due to the high quality factor Q_t. The quality factor Q_t is representative of the antenna losses. Higher Q-factor indicates a lower rate of energy loss relative to the stored energy of the resonator, in other words, the oscillations die out more slowly.

$$Q = 2\pi \frac{Energy\ stored}{Energy\ dissipated\ per\ cycle} = \omega_r \frac{Energy\ stored}{Power\ loss} \tag{5.2.5}$$

This also can be explained by the equivalent circuit of figure 5.1. The quality factor of the resonant patch antenna with resonant frequency f_0 equals

$$Q = \frac{R}{\omega_0 L} \tag{5.2.6}$$

where

$$\omega_0 = 2\pi f_0 = \frac{1}{\sqrt{LC}} \tag{5.2.7}$$

The methods employed to increase impedance bandwidth are essentially variations of three approaches:

1. Increasing the antenna volume. This is accomplished by geometry changes that increase the volume under the patch (e.g., increasing the thickness h), decreasing the substrate dielectric constant, or adding additional coupled resonators.
2. The implementation of a matching network.
3. Perturbing the antenna geometry to create or relocate resonances using shorts and slots in the antenna.

The broadbanding of a microstrip antenna is often accomplished by increasing the thickness of a micrstrip antenna. This broadbanding reaches a limit when the series inductance produced by higher order modes produces a unacceptable mismatch in the driving point impedance Hence, the two properties, bandwidth and match, may need to be traded off in a design.

A large number of microstrip antenna design variations that utilize these approaches have been presented. However, determining the best antennas design is often a long and tedious process, even when carried out systematically, since the various parts of the antenna interact.

5.3 The bandwidth-shape relation

As mentioned in the previous chapter, the shape of the patch affects the impedance bandwidth even for the same maximum dimensions. Some examples demonstrating this have been presented in the corresponding section. This fact is mostly attributed to the superposition of two modes, for example TM_{10} and TM_{01}, which stretch out the bandwidth when compared with a single mode. Specifically, the modification of the patch shape causes a shifting in the cutting frequencies of the modes existing in the antenna cavity, bringing them close to each other. Usually, the implementation of this technique results in circularly polarized antennas, since the two contributing modes are orthogonal to each other.

In general, a microstrip patch antenna may be of any shape: oval, rectangular, star, cross, circle with slot, pentagon, etc. However, if the geometry of the patch differs from the conventional shapes, there are no closed form relations determining the behaviour of the antenna. For this reason, the numerical approach of the problem is indicated. Consideration of these facts about patch antennas leads one to a basic question about microstrip antennas which has not been answered by theory: What microstrip patch shape provides maximum impedance bandwidth?

Nature can be an inspiration for creation in many fields. At this thesis, the form of plants and organisms met in the natural environment has been the initialization point for the patch shape research which leads to improved performance characteristics. This is done by means of the *Gielis* formula [49], also known as the *super-shape* formula.

5.4 The Gielis formula

The Gielis formula (6.1.1) is a geometrical approach that allows the description of many abstract, naturally occurring and man-made geometrical shapes and forms with one simple generic formula.

$$r(\varphi) = \left[\left| \frac{1}{\alpha} \cos\left(\frac{m}{4}\varphi\right) \right|^{n_2} + \left| \frac{1}{b} \sin\left(\frac{m}{4}\varphi\right) \right|^{n_3} \right]^{-1/n_1} \tag{5.4.1}$$

Figure 5.4 Natural shapes described by Gielis formula

The equation 6.1.1 is a polar function of the form $r = f(\varphi)$, which consists a generalization of the super-ellipses formula 5.4.2, derived by converting from cartesian to polar coordinates and introducing the argument $m/4$ of the angle φ. These modifications introduce specific rotational symmetries. Additionally, the exponent n can also differ.

$$|x/\alpha|^n + |y/b|^n = 1 \tag{5.4.2}$$

In equation 6.1.1, the parameters n_i and $m \in \mathbb{R}^+$ (positive real numbers) and α, $b \in \mathbb{R}_0^+$ (positive real numbers but not zero). By setting $n_1 = n_2 = n_3$ and $m = 4$ in equation 6.1.1, an ellipse is obtained. A circle is obtained when additionally $\alpha = b$. A characteristic property of the super-shapes (shapes derived by equation 6.1.1) is that the plane can be divided into a number of sectors equal to m. Asymmetrical shapes can be generated by selecting different parameter in different sectors. Consequently, the super-shape formula generates a large class of super- and sub-shapes, including the super- and sub-circles as special cases.

In general, eq. 6.1.1 modifies the metric of functions and all associated graphs. The simplest case is the modification of the constant function $R = 1$ (deformation of the unit circle). However, other functions $f(\varphi)$ can be used as well. The generic equation 5.4.3 generates a large class of super- and sub-shapes (fig. 5.5), including the super- and sub-circles as special cases.

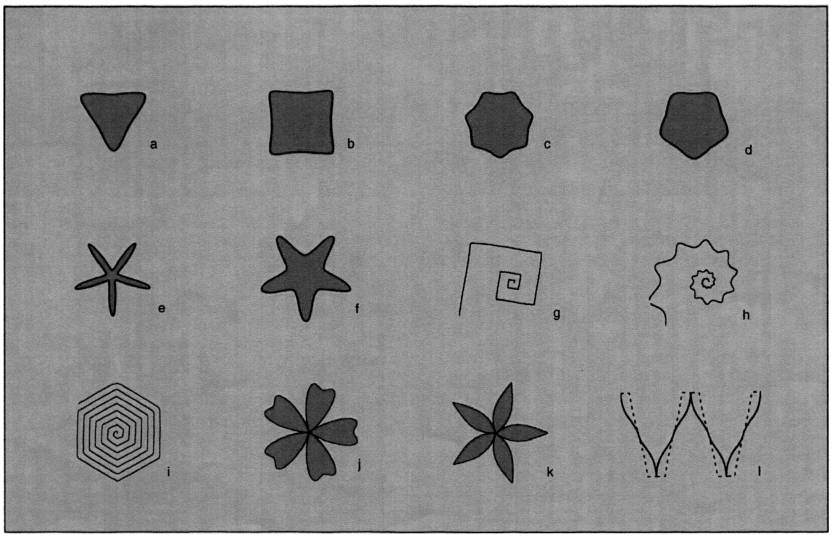

Figure 5.5 Natural super-shapes generated by equation 6.1.1. The numbers between brackets refer to $(m; n_1; n_2 = n_3)$. The value of $\alpha = b$ is 1 except for (e) where $\alpha = b = 10$. (a)$(3; 4.5; 10)$; (b)$(4; 12; 15)$; (c)$(7; 10; 16)$; (d)$(5; 4; 4)$; (e)$(5; 2; 13)$; (f)$(5; 2; 7)$. (g-h) spirals ($r = e^{0.2\varphi}$) modified by eq. 6.1.1. (g)$(4; 100; 100)$; (h)$(10; 5; 5)$. (i) Spiral of Archimedes ($r = \varphi$) modified by eq. 6.1.1 with $(6; 250; 100)$. (j-k) Modified rose curves $|cos(m.\varphi)|$ with $m = 2.5$ inscribed in polygons with values (j)$(2.5; 1/1.3; 2.7)$, (k)$(2.5; 5; 5)$. (l) Super- and sub-cosines: cosine functions ($cos\,\varphi$) inscribed in polygons with values $(4; 1; 1)$, super-cosines, solid line and $(4; 25; 25)$, sub-cosines, dashed line.

The two-dimensional shapes derived by equations 6.1.1 and 5.4.3 can also be described in a multi-dimensional parameter space $\mathbb{R}^6$ with the various parameters $(\alpha, b, n_1, n_2, n_3, m)$.

$$r = f(\varphi)\left[\left|\frac{1}{\alpha}\cos\left(\frac{m}{4}\varphi\right)\right|^{n_2} + \left|\frac{1}{b}\sin\left(\frac{m}{4}\varphi\right)\right|^{n_3}\right]^{-1/n_1} \tag{5.4.3}$$

For simplicity reasons, from now on we will focus on the case of the modification of the unit circle (eq. 6.1.1). The variable m can define zerogons ($m = 0$), monogones ($m = 1$) and diagons ($m = 2$), as well as triangles, squares and polygons with higher rotational symmetries. It determines the number of points fixed on the unit circle (or ellipse for $\alpha \neq b$) and their spacing. The values of n_2 and n_3 determine whether the shape is inscribed or circumscribed in the unit circle. For $n_2 = n_3 < 2$ the shape is inscribed (sub-polygons), while for $n_2 = n_3 > 2$ the shape will circumscribe the circle (super-polygons). Corners can be sharpened or flattened and the sides can be straight or bent (convex or concave). Also, when m is positive but not an integer, the shape generated does not close after one rotation. At this study though, we will consider only integer values for m.

As indicated, the super-shape formula provides a relative flexibility in the shaping of the radiator, since by tuning six parameters a large variety of shapes is derived. The range of the possible shapes includes also most of the trivial shapes such as circle, triangle, square, and other polygons or an approximation of them. In tables 5.2 and 5.1 some possible shaping modifications regarding the microstrip patch antennas are presented.

The flexibility feature of the super-shape patch antennas provides, thus, the possibility to investigate the effect of the patch shape modification to the performance characteristics of the patch antennas. Specifically, the impedance bandwidth, the radiation pattern, the realized gain and the polarization properties of the super-shape patch antennas are studied in this project. Since, there are no analytical equations describing the behaviour a patch antenna whose shape differs from the trivial ones, the radiation performance of these antennas is analysed by means of *CST Microwave Studio*. The latter is a powerful electromagnetic simulation tool that provides accurate analysis for high frequency devices like patch antennas.

Table 5.1 Examples of super-shapes when $n_2 = n_3 = 0.5$

n_1	$m = 1$	$m = 2$	$m = 3$	$m = 4$
0.1			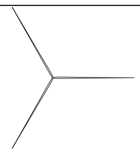	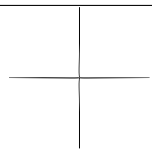
0.3	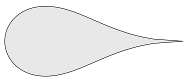	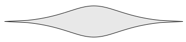	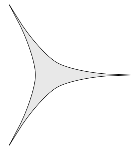	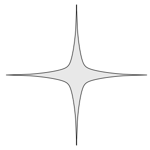
0.5	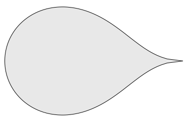	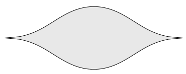	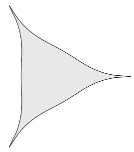	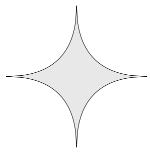
0.7	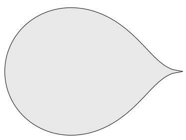	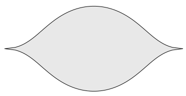	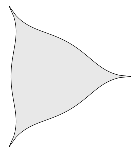	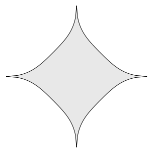
1	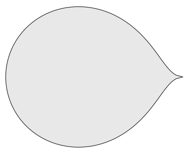	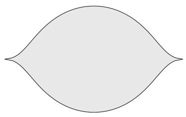	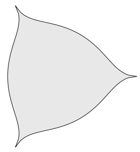	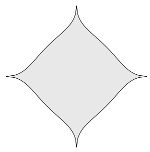
3	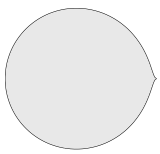	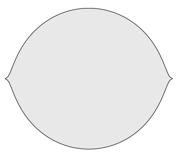	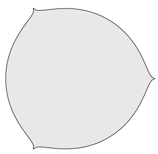	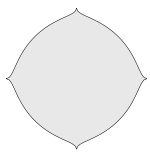
5	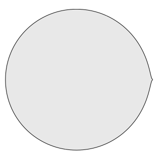	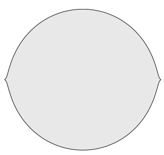	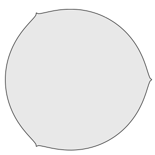	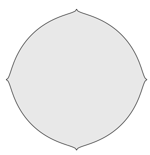
10	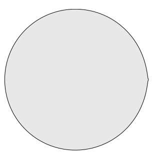	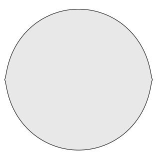	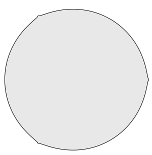	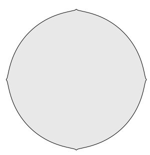

Table 5.2 Examples of super-shapes when $n_1 = 0.5$

$n_2 = n_3$	$m = 1$	$m = 2$	$m = 3$	$m = 4$
0.1	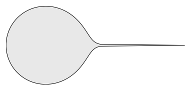	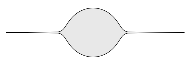	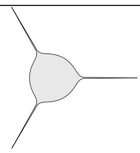	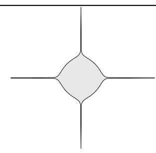
0.3	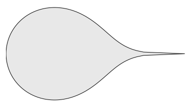	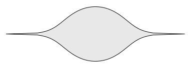	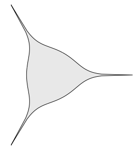	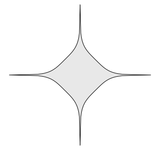
0.5	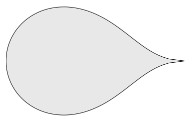	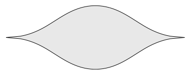	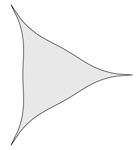	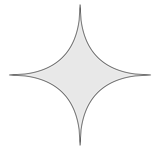
0.7	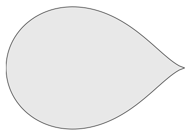	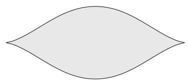	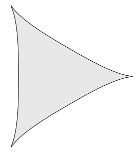	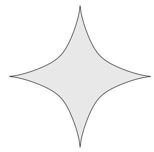
1	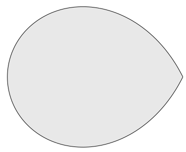	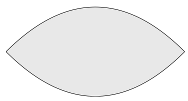	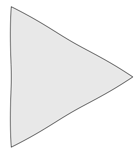	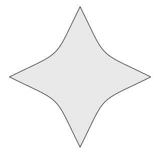
3	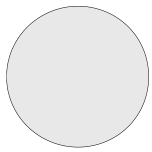	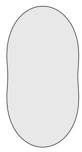	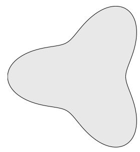	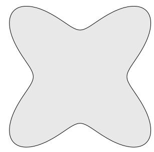
5	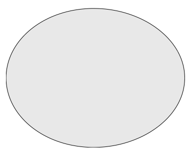	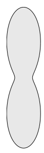	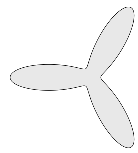	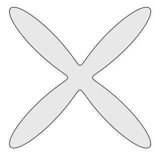
10	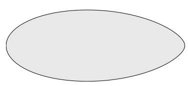	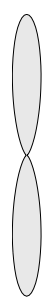	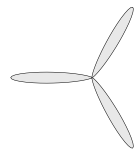	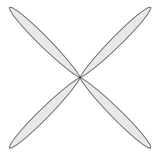

Chapter 6

Full-wave analysis of supershaped patch antennas

6.1 The geometry of the supershaped patch antennas

The investigated SPA (Supershaped Patch Antenna), as shown if figure 6.1, consists of a metallic microstrip patch placed on top of a circular grounded dielectric substrate having radius $R_s = 200\,mm$ and thickness $t_d = 6.35\,mm$. The patch and the ground plane are considered perfectly electric conductors (PEC) and their thickness was set to $t_g = 0.07\,mm$, while for the substrate, the dielectric material *Rogers RT duroid 5880* with dielectric permittivity $\varepsilon_r = 2.2$ was chosen. The SPA is fed via a SMA connector, whose inner and outer diameter is $d_f = 1.19\,mm$ and $D_f = 4.1\,mm$ respectively. The resulting characteristic impedance is thus $Z_0 = 50\,Ohm$.

$$R_g(\varphi) = \left[\left|\frac{1}{\alpha}\cos\left(\frac{m}{4}\varphi\right)\right|^{n_2} + \left|\frac{1}{b}\sin\left(\frac{m}{4}\varphi\right)\right|^{n_3}\right]^{-1/n_1} \tag{6.1.1}$$

The contour profile of the metallic patch is defined by the polar function (6.1.1), where $R_g(\varphi)$ is a curve located in the $xy-$plane and $\varphi \in [0, 2\pi)$ is the angular coordinate. Equation (6.1.1) is a generalization of the ellipse's polar equation and is known as *superformula*. The shape of the SPA profile can be modified by acting on a sextet of real and positive numerical parameters $(\alpha, b, m, n_1, n_2, n_3) \in \mathbf{R}^6$, with $\alpha, b \neq 0$. This parameter dependence gives the possibility of automatically reshaping the SPA profile and deriving the desired performance characteristics.

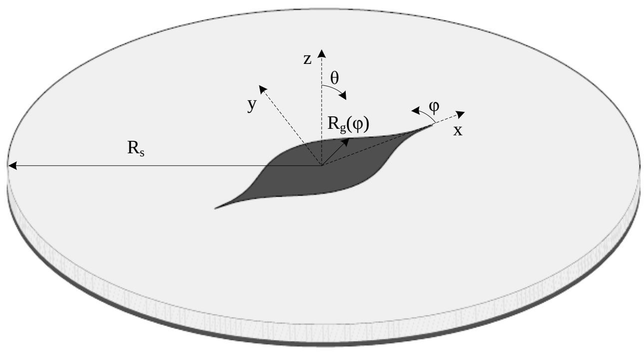

(a) Angle view

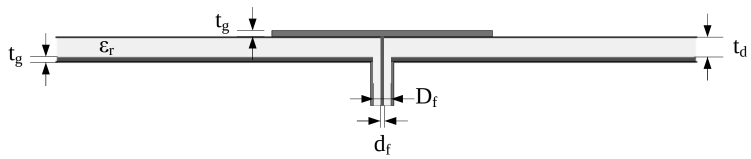

(b) Side view

Figure 6.1 SPA geometry with relevant reference system and dimensioning

The circular patch obtained for $m = 0$ was chosen as a starting point. The diameter was set to $d_p = 40\,mm$, which is approximately half wavelength in the dielectric at the operating frequency of interest $f_r = 2.4\,GHz$. In order to achieve this, we set the parameters α and b equal to 20 for the case $m = 0$. Varying the parameter (m, n_1, n_2, n_3), the effective radius (6.1.2) of the patch should remain constant because all the antennas must feature the same area. Therefore, different values for α and b should be calculated for each case so as this condition to be satisfied.

$$\rho_e = \sqrt{\frac{1}{2\pi}\int_0^{2\pi} R_g^2(\varphi)\mathrm{d}\varphi} \tag{6.1.2}$$

6.2 The impact of the parameter m to the performance characteristics of the supershaped patch antennas

The SPA's were designed and investigated by means of the full-wave commercial software *CST Microwave Studio.* In particular, a set of simulations was carried out in order to study the effect of the parameter m variation of equation (6.1.1) in the performance of the antennas. So, this set of simulations was carried out setting $(\alpha, b, n_1, n_2, n_3) = (\alpha, \alpha, 0.5, 0.5, 0.5)$ and $m = 0, 1, \ldots, 5$. Figure 6.2 shows the derived SPA's.

The fractional bandwidth with respect to the feeding probe location, as well as the radiation patterns of the corresponding antennas, were obtained and presented in figures 6.3 and 6.4 respectively.

The fundamental resonant frequency of the antennas $m = 0$ and $m = 1$ is $2.65\,GHz$ and $2.19\,GHz$ respectively while for $m = 2, \ldots, 5$ ranges between $1.7 - 1.8\,Gz$. The decline can be attributed to the increased maximum dimension associated with the first resonant mode. Namely, the branches that are formed in figures 6.2c-f stress the maximum current path between the periphery points raising the wavelength of the fundamental resonant mode.Moreover, it can be observed that the sharp branches impair the fractional bandwidth.

The radiation patterns in figure 6.4 are broadside since they result from the field configuration of the fundamental mode.

m	$a = b$	$f_c(GHz)$	$FBW(\%)$	$G_0(dBi)$
0	20	2.65	1.2	7.61
1	43.416	2.19	5.1	7.56
2	43.416	1.71	2.8	8.23
3	43.416	1.81	2.7	8.17
4	43.416	1.79	2.7	8.16
5	43.416	1.73	2.7	8.21

Table 6.1 Geometrical and performance characteristics of SPA $(n_1, n_2, n_3) = (0.5, 0.5, 0.5)$ for the fundamental resonant frequency

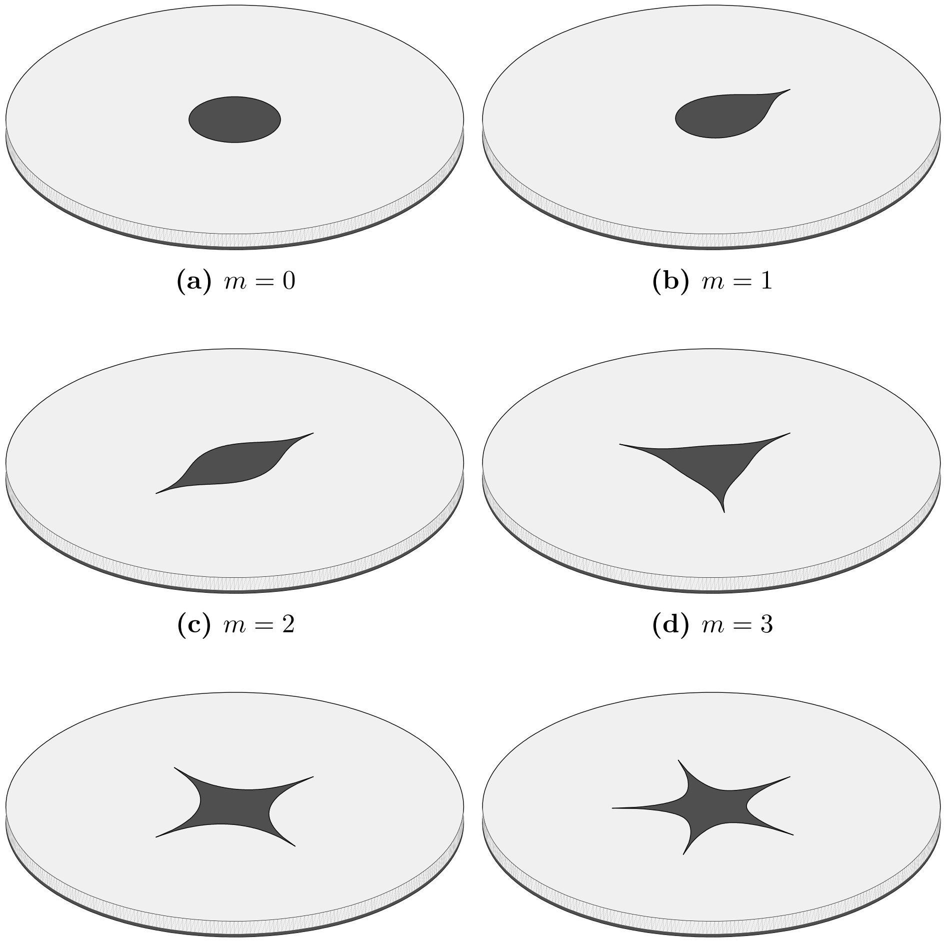

(a) $m = 0$ **(b)** $m = 1$

(c) $m = 2$ **(d)** $m = 3$

(e) $m = 4$ **(f)** $m = 5$

Figure 6.2 SPA's for different values of m and $(n_1, n_2, n_3) = (0.5, 0.5, 0.5)$

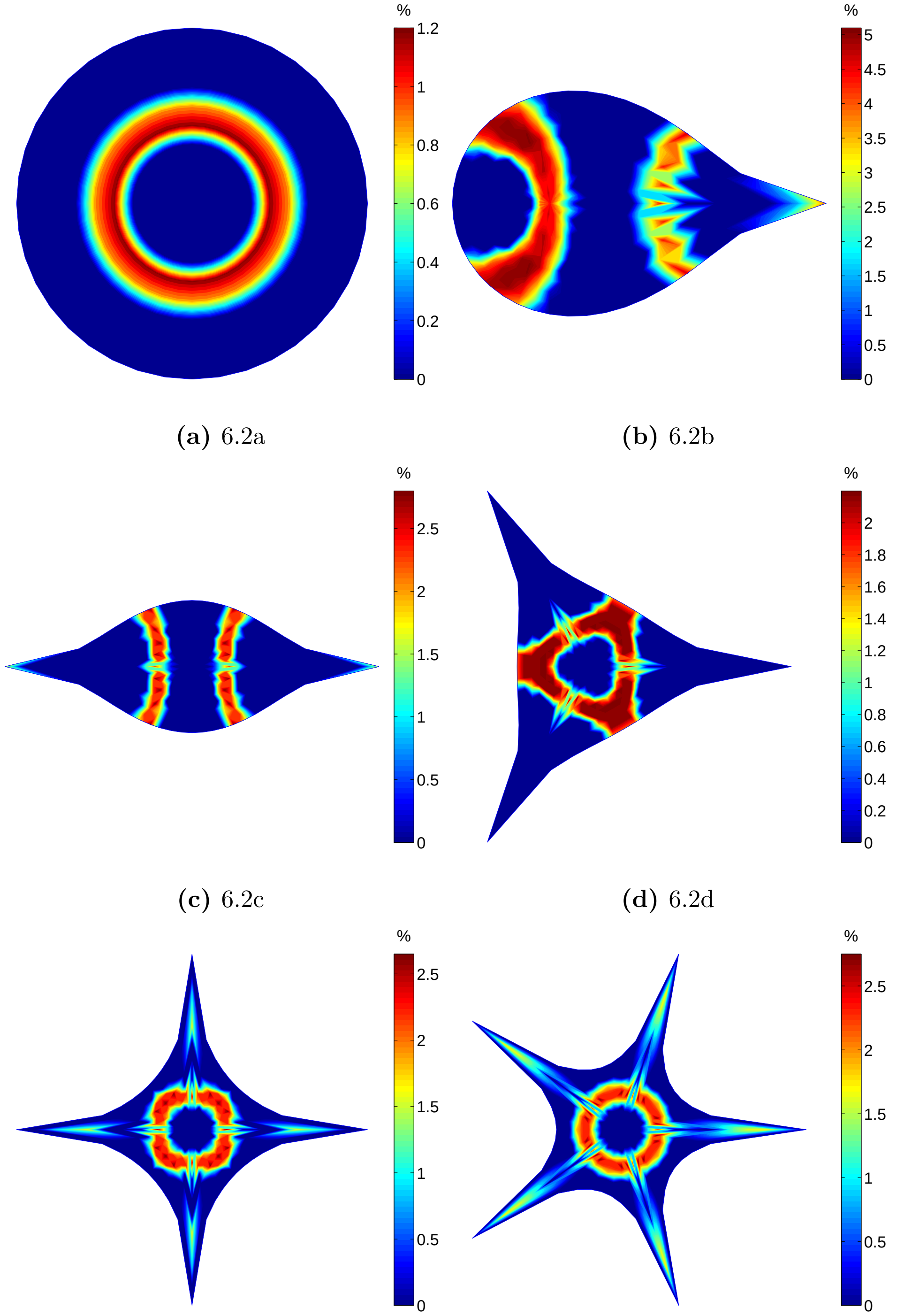

(a) 6.2a **(b)** 6.2b

(c) 6.2c **(d)** 6.2d

(e) 6.2e **(f)** 6.2f

Figure 6.3 SPA's fractional bandwidth in % as function of the probe location for the fundamental resonant frequency

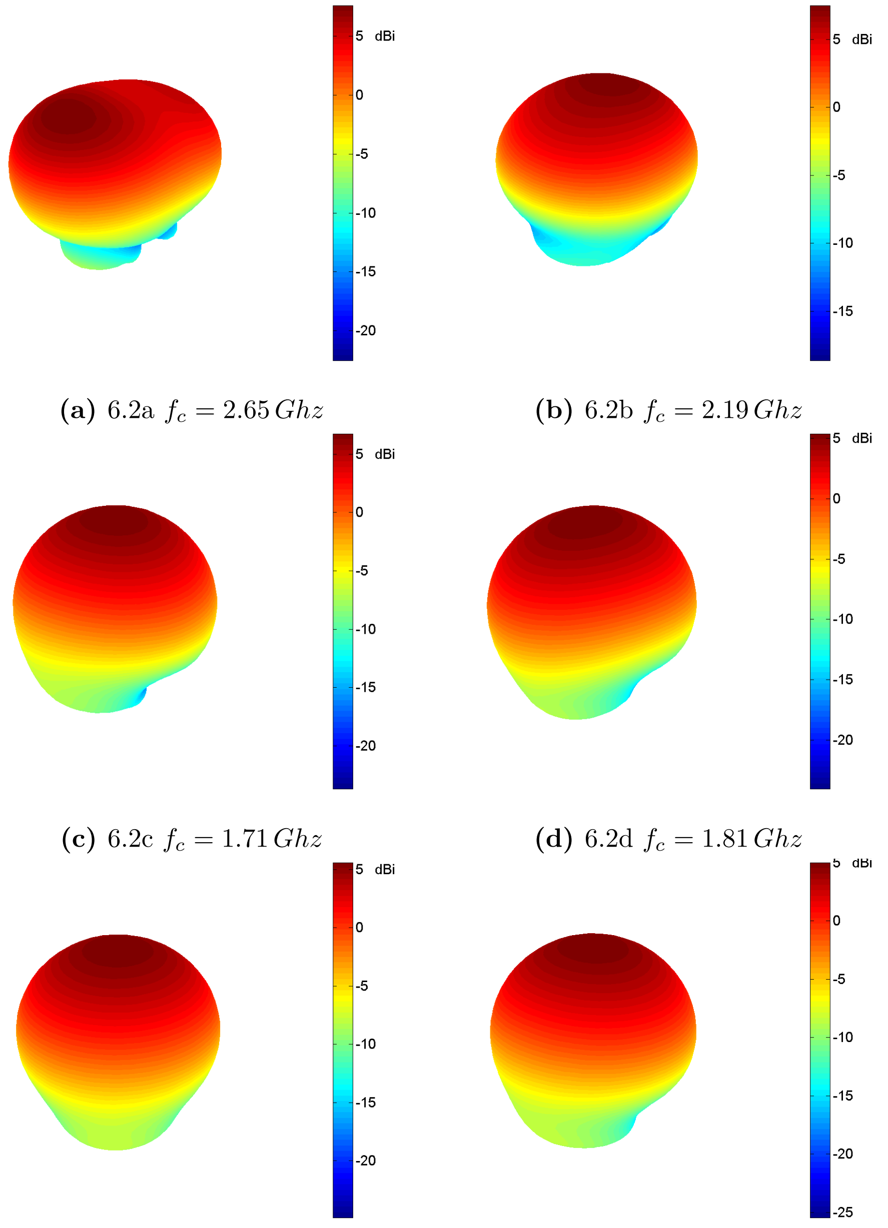

(a) 6.2a $f_c = 2.65\, Ghz$ **(b)** 6.2b $f_c = 2.19\, Ghz$

(c) 6.2c $f_c = 1.71\, Ghz$ **(d)** 6.2d $f_c = 1.81\, Ghz$

(e) 6.2e $f_c = 1.79\, Ghz$ **(f)** 6.2f $f_c = 1.73\, Ghz$

Figure 6.4 Radiation patterns of the SPA's $(m = 0, 1, \ldots, 5)$ in the central operating frequency

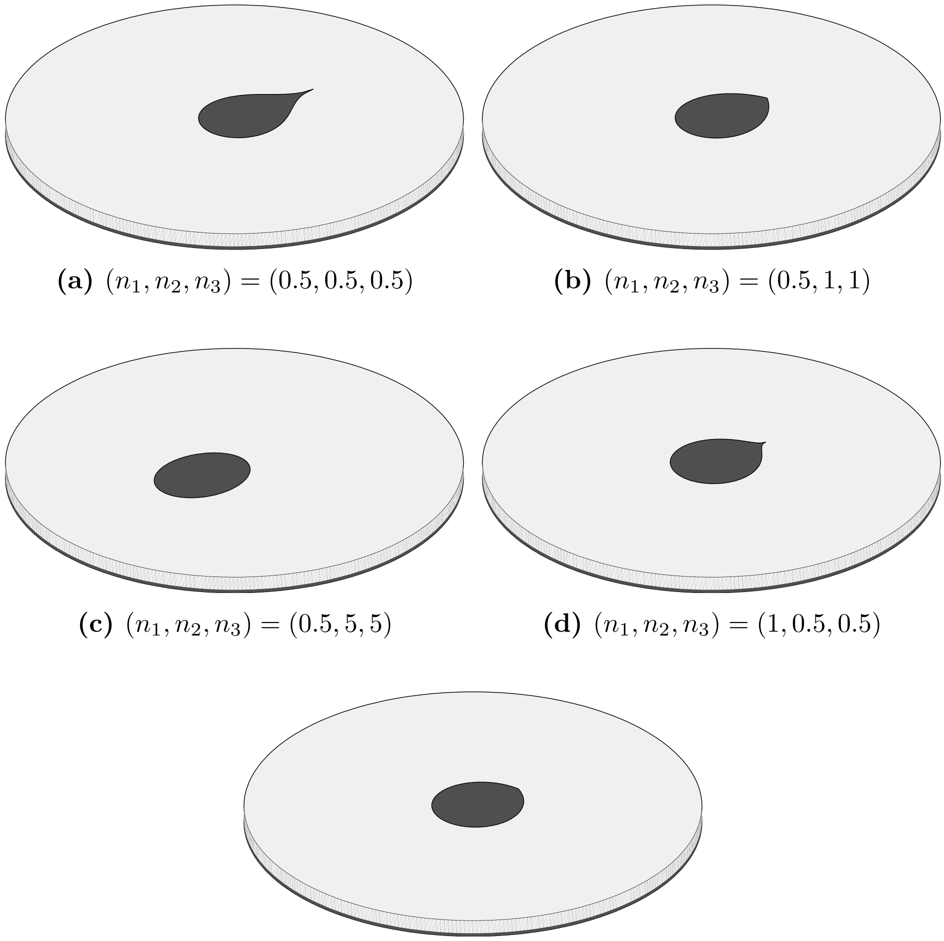

(a) $(n_1, n_2, n_3) = (0.5, 0.5, 0.5)$

(b) $(n_1, n_2, n_3) = (0.5, 1, 1)$

(c) $(n_1, n_2, n_3) = (0.5, 5, 5)$

(d) $(n_1, n_2, n_3) = (1, 0.5, 0.5)$

(e) $(n_1, n_2, n_3) = (1, 1, 1)$

Figure 6.5 Super-shaped microstrip patch antennas $m = 1$

6.3 One-branch supershaped patch antennas

Among the variations presented in section 6.2, the $m = 1$ case, also referred as monogon, seemed to be the most promising, thus, it was chosen for further investigation. Then, keeping fixed $m = 1$, the parameters n_1, n_2, n_3 were tuned in order the effect of their variation to the performance of the SPA to be studied. So, some configurations derived by the aforementioned procedure are introduced in figure 6.5.

In figure 6.6, the simulation results regarding the impedance bandwidth of the super-shaped patch antennas of figure 6.5 are summarized. The first patch antenna achieves maximum impedance bandwidth 5.1% for the frequency band $2.136 - 2.248\,GHz$ when it is fed via a coaxial cable to specific point. The antenna of the figure 6.5b presents an impedance bandwidth of approximately 20% in the frequency band $2.43 - 2.95\,GHz$. The figure 6.5c depicts a patch antenna which operates in the range $2.45 - 3.03\,GHz$, thus, its bandwidth exceeds 21%. With variation presented in figure 6.5d a bandwidth of the order of around 15.5% can be obtained for the frequencies $2.49 - 2.91\,GHz$. Finally, the antenna of the figure 6.5e achieves an impedance bandwidth of around 9.8% in the center frequency $2.68\,GHz$.

The operating frequency band is obtained from the magnitude of the return loss parameter $\mid S1,1 \mid$ when this falls below $-10\,dB$ as shown in figures 6.7a - e. In these figures, it can be observed that the extended bandwidth of the antennas 6.5b - d is due to the convergence of two adjacent modes. This happens because the dimensions associated with the first two modes are slightly different. Specifically, the first mode is related to the distance along x-axis while the second mode is designated by the dimension along y-axis. Observing the figures 6.6b-d we can see that the dimensions along x and y axes differ as much as it needs for the two resonant frequencies to get closer. However, if the two dimensions become too comparable, like in figure 6.6e, the two resonant frequencies almost coincide resembling the circular patch case.

As shown in figure 6.8, the variation of the maximum realized gain in the operating frequency band of each patch antenna of figures 6.5a to 6.5e ranges from 6 to approximately $7.5\,dB$.

The surface current distributions of the $m = 1$ SPA's were calculated with the help of *CST Microwave Studio* and presented in figure 6.9. Based on figures 6.9a and 6.9b, we can presume that this antenna is orthogonally polarized as it was expected from the fundamental mode operation. Figures 6.9d and 6.9f show a strong current at phase $\theta = 90^o$ which is almost orthogonally polarized compared to the currents at $\theta = 0^o$ in figures 6.9c and 6.9e. This leads to the conclusion that the antennas 6.5b and 6.5c produce a circularly polarized radiation. This effect is no longer dominant in figures 6.9g-h and 6.9i-j because the phase difference of the two mode currents is lower than 90^o.

Figures 6.10 correspond to the normalized radiation patterns in terms of the realized gain when the antennas operate in the central frequency. It can be

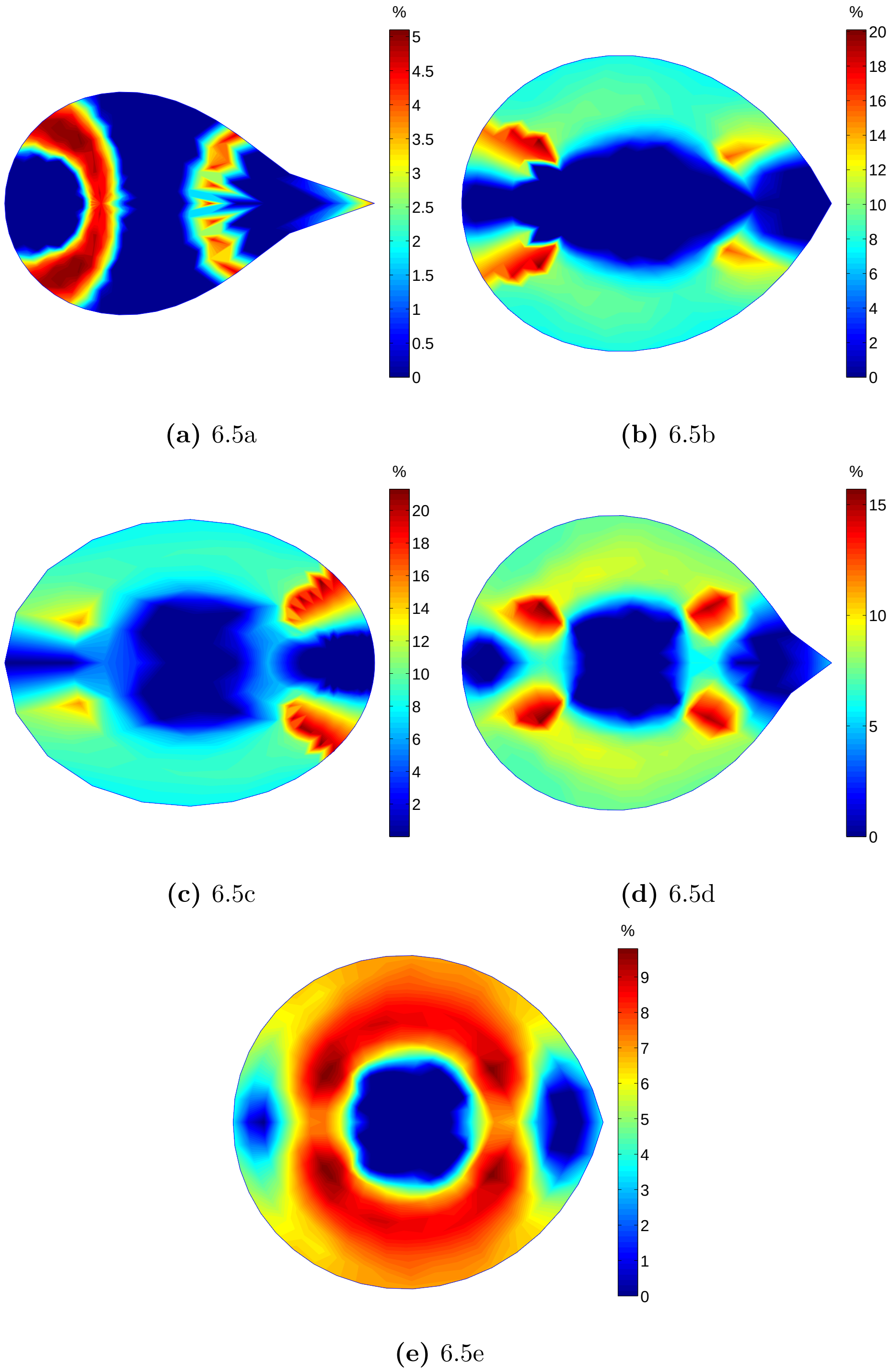

(a) 6.5a (b) 6.5b

(c) 6.5c (d) 6.5d

(e) 6.5e

Figure 6.6 Fractional bandwidth in % of SPA's ($m = 1$) for the fundamental resonant frequency

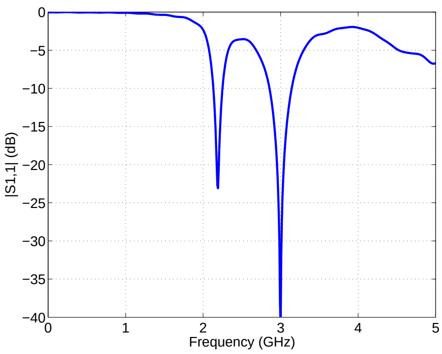

(a) 6.5a $(\phi_0, \rho_0) = (1.885, 0.6R_g)$

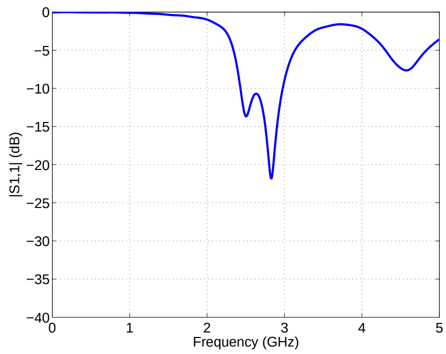

(b) 6.5b $(\phi_0, \rho_0) = (2.1991, 0.6R_g)$

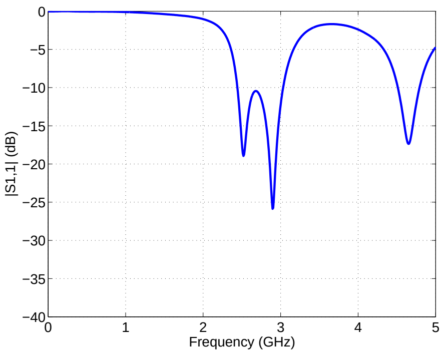

(c) 6.5c $(\phi_0, \rho_0) = (1.7279, 0.8R_g)$

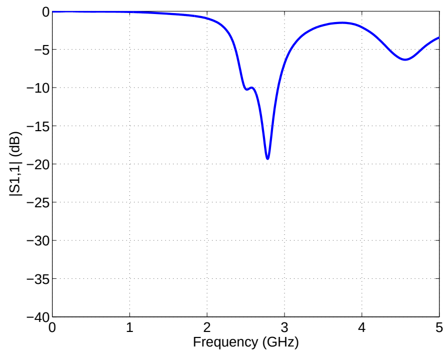

(d) 6.5d $(\phi_0, \rho_0) = (2.3562, 0.6R_g)$

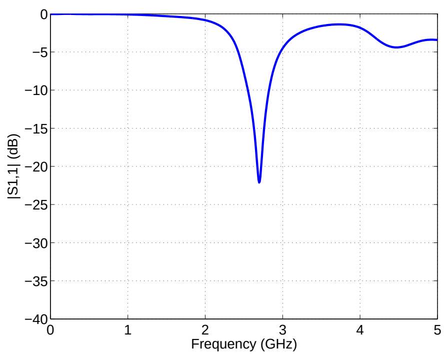

(e) 6.5e $(\phi_0, \rho_0) = (0.4712, 0.6R_g)$

Figure 6.7 Return loss $(m = 1)$ when feeding probe is located to the maximum FBW point

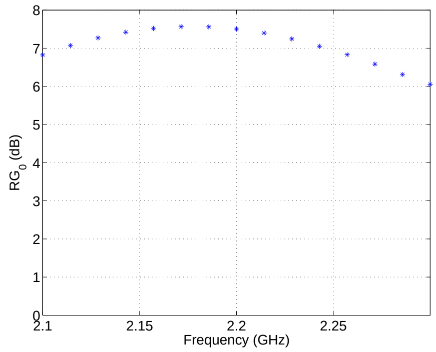

(a) 6.5a

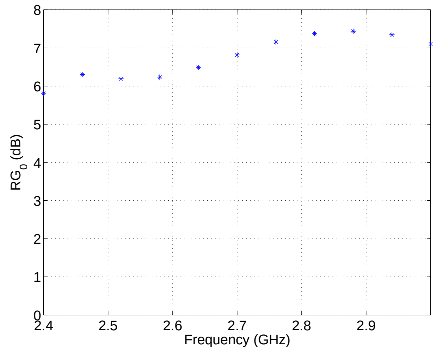

(b) 6.5b

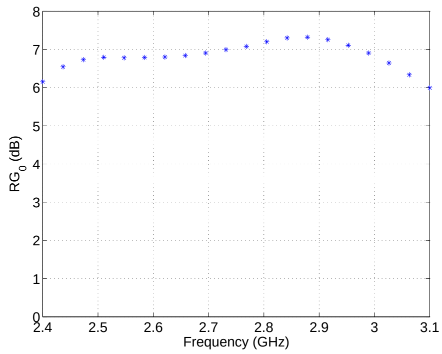

(c) 6.5c

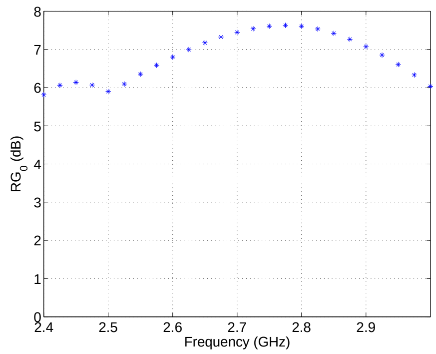

(d) 6.5d

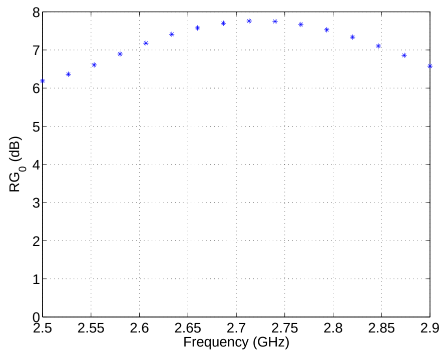

(e) 6.5e

Figure 6.8 The maximum realized gain ($m = 1$) with respect to operating frequency

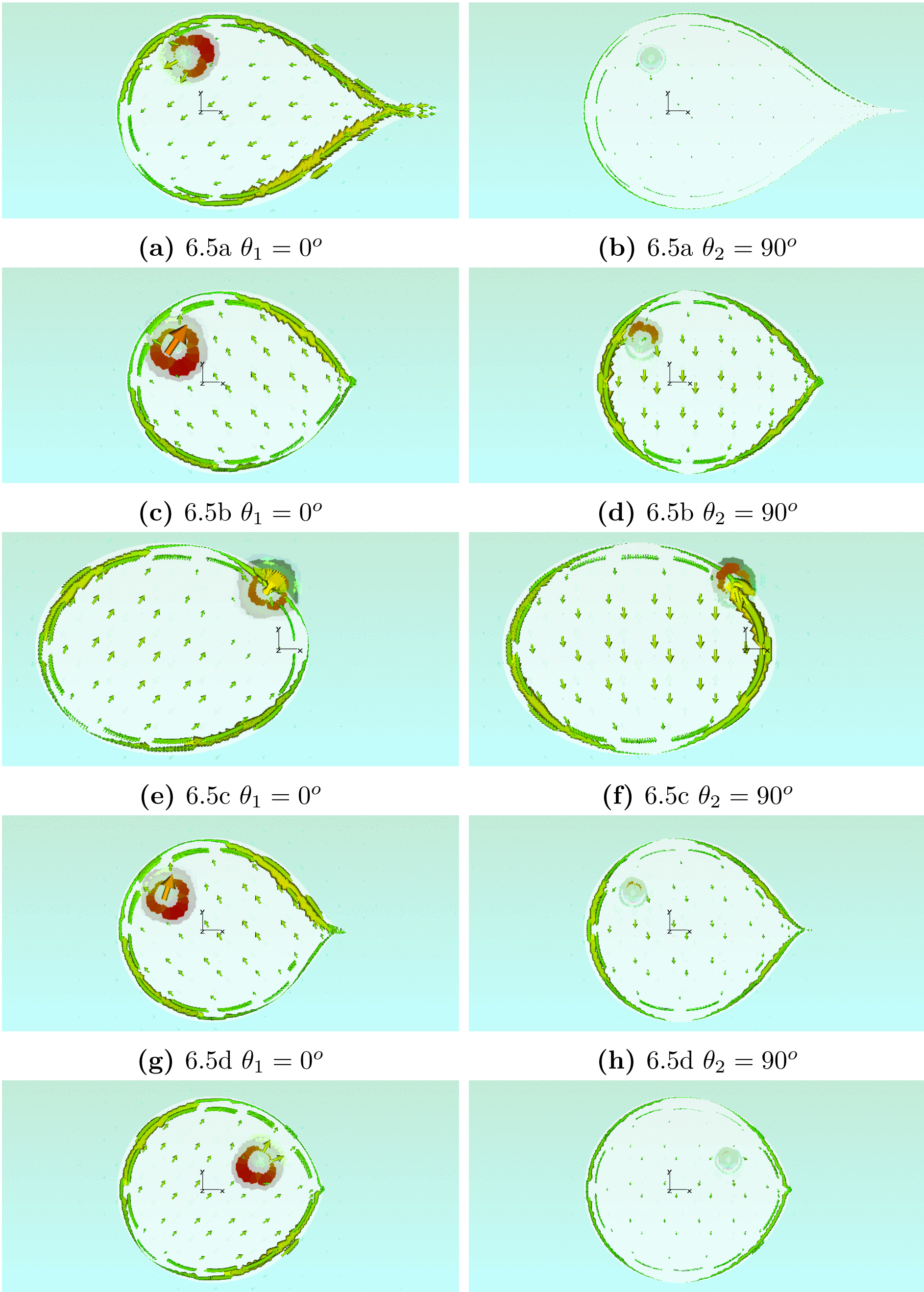

(a) 6.5a $\theta_1 = 0^o$ **(b)** 6.5a $\theta_2 = 90^o$

(c) 6.5b $\theta_1 = 0^o$ **(d)** 6.5b $\theta_2 = 90^o$

(e) 6.5c $\theta_1 = 0^o$ **(f)** 6.5c $\theta_2 = 90^o$

(g) 6.5d $\theta_1 = 0^o$ **(h)** 6.5d $\theta_2 = 90^o$

(i) 6.5e $\theta_1 = 0^o$ **(j)** 6.5e $\theta_2 = 90^o$

Figure 6.9 Surface current of $m = 1$ SPA's at the central frequency for the phase angles $\theta_1 = 0^o$ and $\theta_2 = 90^o$

seen that the radiation pattern depicted in 6.10a is broadside with one wide main lobe. On the other hand, in the radiation pattern corresponding to the antenna 6.5c two peaks are slightly distinguished, so, the pattern seems to consist of two merged lobes. This is attributed to the two converged resonant modes as shown in the figure 6.7c. However, the radiation pattern 6.10c still can be considered broadside.

The numerical results for the configurations shown in the figures 6.5a - e are listed in table 6.2.

$n1$	$n2$	$n3$	$a = b$	$f_c(GHz)$	$FBW(\%)$	$G_0(dBi)$
0.5	0.5	0.5	43.416	2.19	5.1	7.56
0.5	1	1	5.5407	2.7	20	7.49
0.5	5	5	1.1758	2.74	21	7.32
1	0.5	0.5	895.9921	2.7	15.5	7.63
1	1	1	25.0663	2.68	9.8	7.75

Table 6.2 Geometrical and performance characteristics of the different super-shaped patch antennas ($m = 1$) for the fundamental resonant frequency

6.4 Four-branch supershaped patch antennas

An interesting variation of the shapes derived from the *Gielis* superformula results as m is set equal to 4. Then four branches are formed around the patch. Similarly to the cases studied in the section 6.3, the performance of a number of four-branch supershaped patch antennas is reported in this section. Figure 6.11 shows the geometry of four patch antennas belonging to the subgroup $m = 4$. Figures 6.12 and 6.13 illustrate the fractional bandwidth as a function of the feeding probe location and the return loss with respect to the operating frequency when the antennas are fed to the best matching point.

In figures 6.12 the red regions represent the well matching feeding locations. The less concave shapes 6.12b and 6.12d exhibit better bandwidth characteristics than the other two antennas. The broadening is due to the excitation of two modes caused by the proper feeding location.

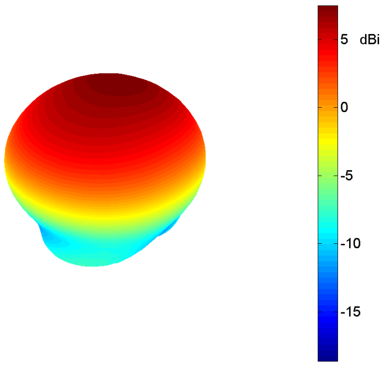

(a) 6.5a $f_c = 2.2\,GHz$

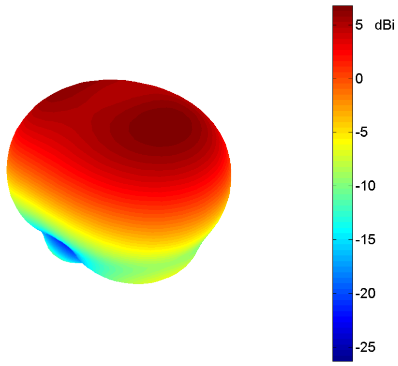

(b) 6.5b $f_c = 2.7\,GHz$

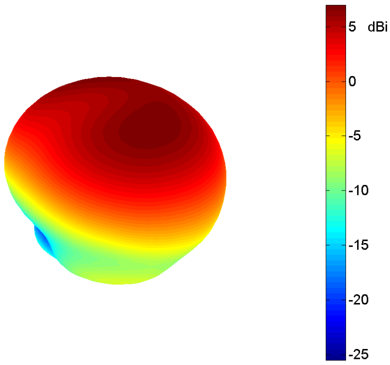

(c) 6.5c $f_c = 2.74\,GHz$

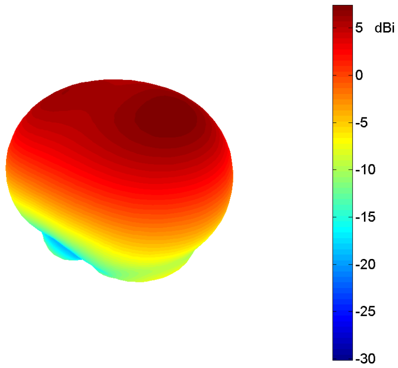

(d) 6.5d $f_c = 2.7\,GHz$

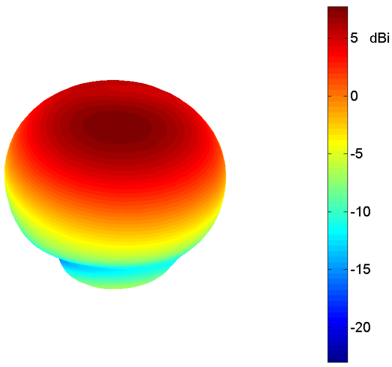

(e) 6.5e $f_c = 2.68\,GHz$

Figure 6.10 Radiation patterns of the SPA's ($m = 1$) in the central operating frequency

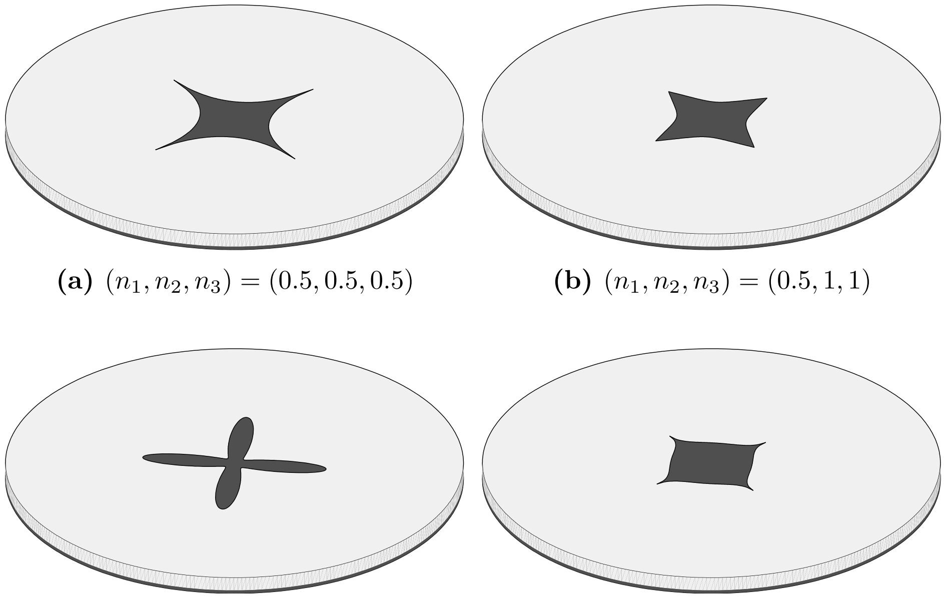

(a) $(n_1, n_2, n_3) = (0.5, 0.5, 0.5)$ **(b)** $(n_1, n_2, n_3) = (0.5, 1, 1)$

(c) $(n_1, n_2, n_3) = (0.5, 5, 5)$ **(d)** $(n_1, n_2, n_3) = (1, 0.5, 0.5)$

Figure 6.11 SPA's derived for $m = 4$

The resonance frequency of the patch antennas depends on their geometrical characteristics. It should be remarked that the resonance frequencies of the antennas 6.11a and 6.11c are $1.79\,GHz$ and $1.37\,GHz$ respectively which is lower compared to those of 6.11b and 6.11d (figures 6.13). This is explained by the existence of bigger branches that cause the prolongation of the current path.

The $m = 4$ antennas are characterized by four symmetry axes, one horizontal, one vertical and two diagonal. So, the first two modes have exactly the same resonant frequencies but their currents are orthogonally polarized and they are in phase which results in a linear diagonal polarization as seen in figures 6.14. The excitement of both modes requires the feeding location to lie on one of the two diagonals, that is $\phi = \pi/4$ or $\phi = 3\pi/4$ plane.

The radiation patterns of the $m = 4$ antennas presented in figures 6.15 show that they exhibit broadside radiation and they are directional since the maximum realized gain varies from 7.4 to $8.1\,dBi$.

In table 6.3 the geometrical and performance characteristics referring to the fundamental resonant frequency of the antennas in figure 6.11 are summa-

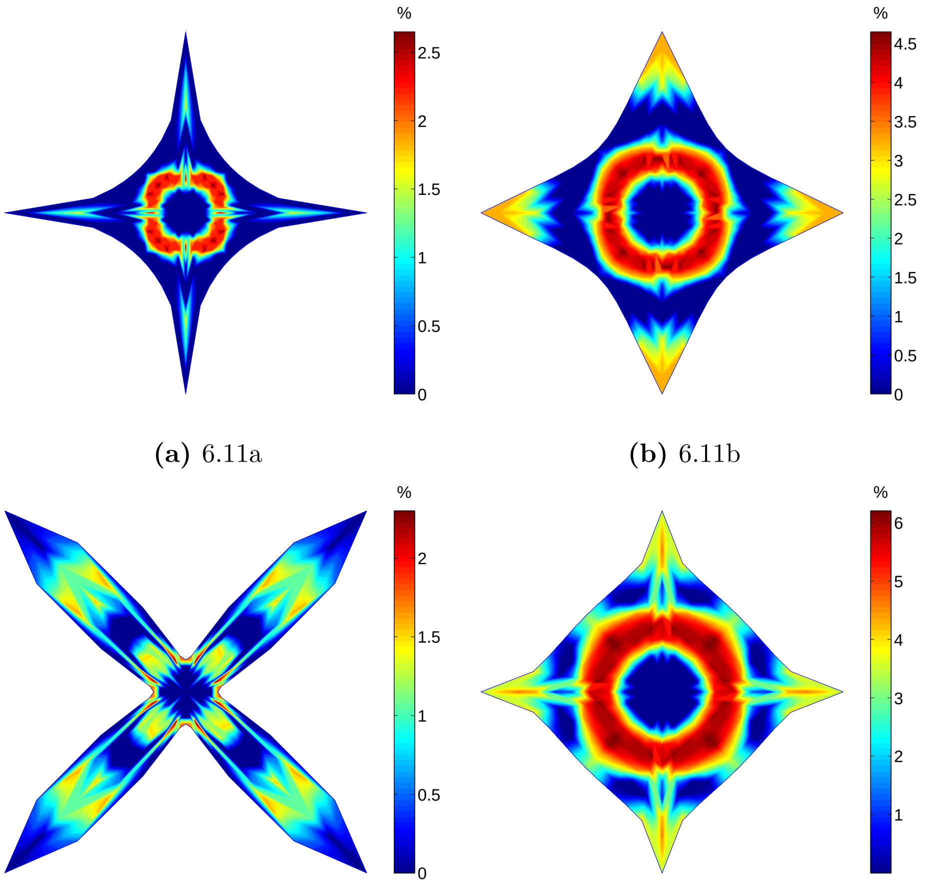

(a) 6.11a **(b)** 6.11b

(c) 6.11c **(d)** 6.11d

Figure 6.12 Fractional bandwidth in % of SPA's ($m = 4$) for the fundamental resonant frequency

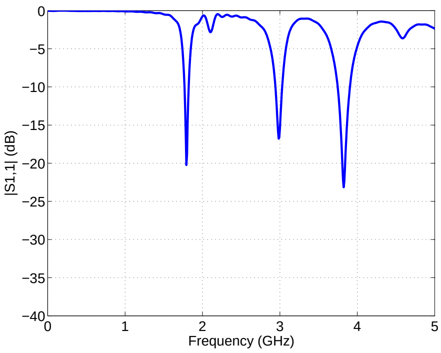

(a) 6.11a $(\phi_0, \rho_0) = (0.7854, 0.6R_g)$

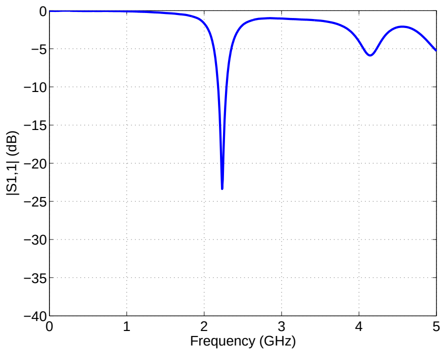

(b) 6.11b $(\phi_0, \rho_0) = (0.7854, 0.6R_g)$

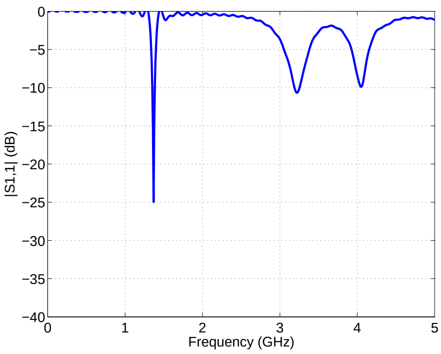

(c) 6.11c $(\phi_0, \rho_0) = (0.3141, 0.6R_g)$

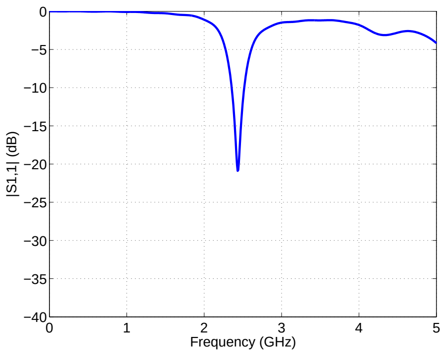

(d) 6.11d $(\phi_0, \rho_0) = (0.7854, 0.6R_g)$

Figure 6.13 Return loss ($m = 4$) when feeding probe is located to the maximum FBW point

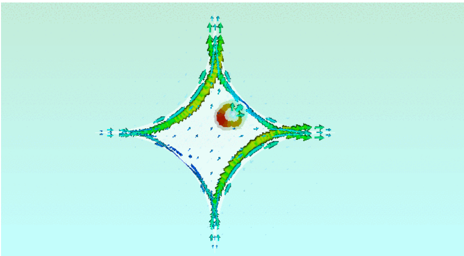

(a) 6.11a $\theta_1 = 0^o$

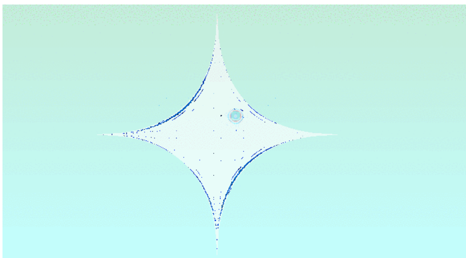

(b) 6.11a $\theta_2 = 90^o$

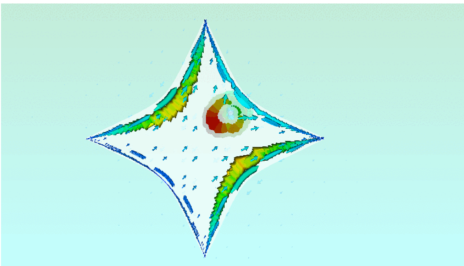

(c) 6.11b $\theta_1 = 0^o$

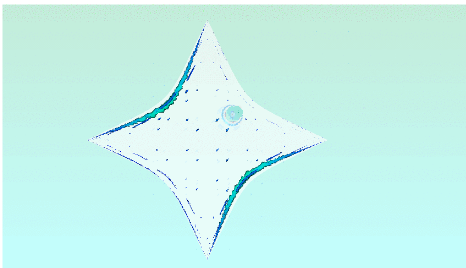

(d) 6.11b $\theta_2 = 90^o$

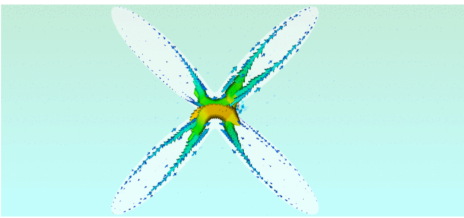

(e) 6.11c $\theta_1 = 0^o$

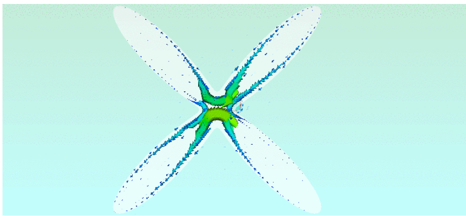

(f) 6.11c $\theta_2 = 90^o$

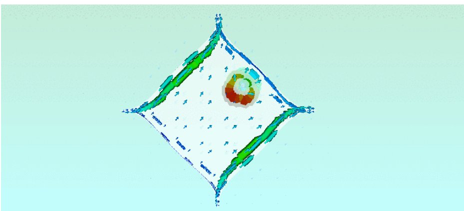

(g) 6.11d $\theta_1 = 0^o$

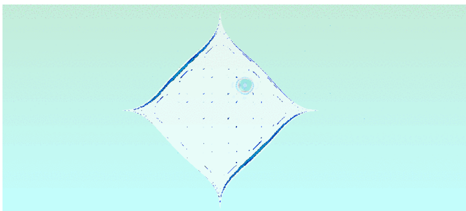

(h) 6.11d $\theta_2 = 90^o$

Figure 6.14 Surface current of $m = 4$ SPA's at the central frequency for the phase angles $\theta_1 = 0^o$ and $\theta_2 = 90^o$

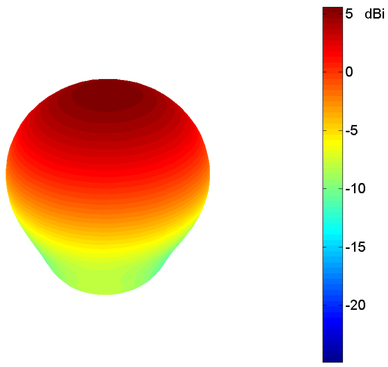

(a) 6.11a $f = 1.8\,GHz$

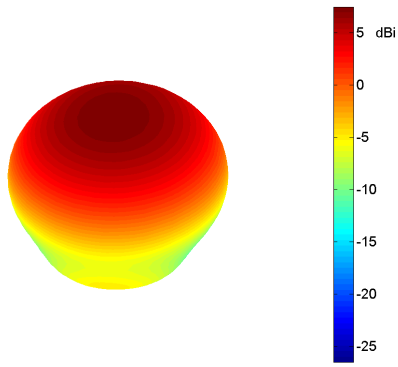

(b) 6.11b $f = 2.22\,GHz$

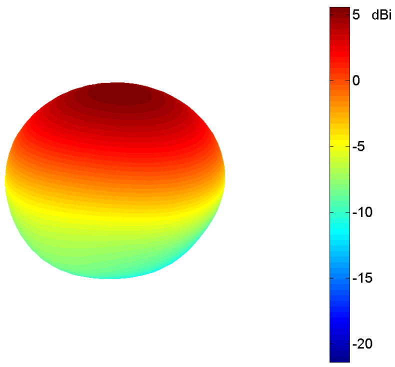

(c) 6.11c $f = 1.37\,GHz$

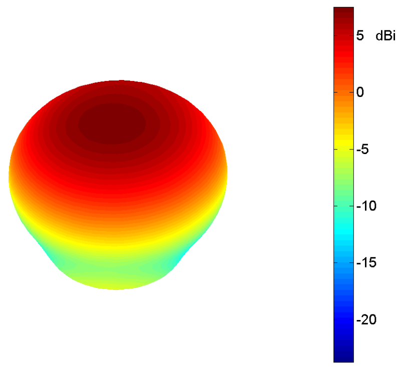

(d) 6.11d $f = 2.43\,GHz$

Figure 6.15 Radiation patterns of the SPA's ($m = 4$) in the central operating frequency rized.

$n1$	$n2$	$n3$	$a = b$	$f_c(GHz)$	$FBW(\%)$	$G_0(dBi)$
0.5	0.5	0.5	43.416	1.79	2.68	8.16
0.5	1	1	5.5407	2.23	4.65	7.48
0.5	5	5	1.1758	1.368	2.34	7.42
1	0.5	0.5	895.992	2.43	6.24	7.6

Table 6.3 Geometrical and performance characteristics of the different SPA's ($m = 4$) for the fundamental resonant frequency

6.5 Correlation with the rectangular patch antenna

Two microstrip patch antennas with the same volume and the same fundamental resonant frequency were simulated and their performances were compared. The first one is a SPA derived by the Gielis' formula for the parameter values $(a, b, m, n_1, n_2, n_3) = (5.5407, 5.5407, 1, 0.5, 1, 1)$. The second one is a rectangular patch antenna whose length is $L = 39.9\,mm$ and width $W = 31.49\,mm$. So, both antennas have an area of $1256.6\,mm^2$. The length of the rectangle was chosen so as the first resonant mode to coincide with the first resonant mode of the drop-shaped antenna while the width was calculated basing on the equality of the two patch areas. The height of the substrate of both antennas is $6.35\,mm$.

Figure 6.16 shows the impedance bandwidth of the two antennas in the band $2-3\,GHz$. The highest fractional bandwidth for both antennas results from the excitation of the first two adjacent modes, TM_{10} and TM_{01}. This happens when the feeding probe deviates from the horizontal axis and the current associated with the TM_{01} becomes noticeable. Figures 6.17 show the highest fractional bandwidth return loss curves. Because of the orthogonality of these modes, when they are excited at the same time they give circular polarization. Specifically, the drop-shaped patch antenna is right-handed circularly polarized while the rectangular patch is left-handed circularly polarized. In both shapes, the dimensions are properly adjusted so as the resonance frequencies of the two modes to be adequately close to each other.

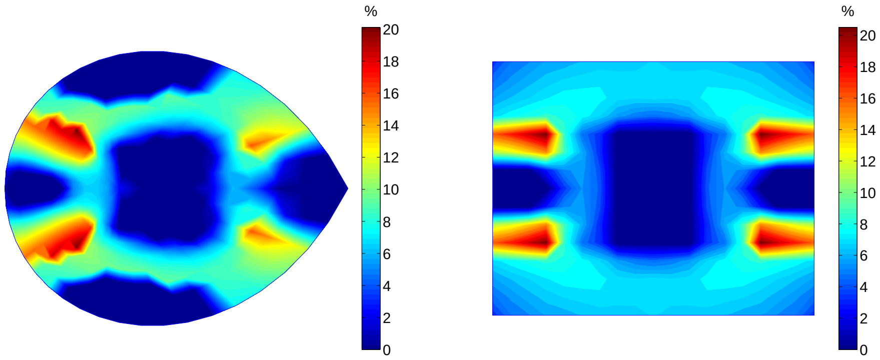

(a) Drop-shaped patch **(b)** Rectangular patch

Figure 6.16 Impedance bandwidth of two equally volume patch antennas

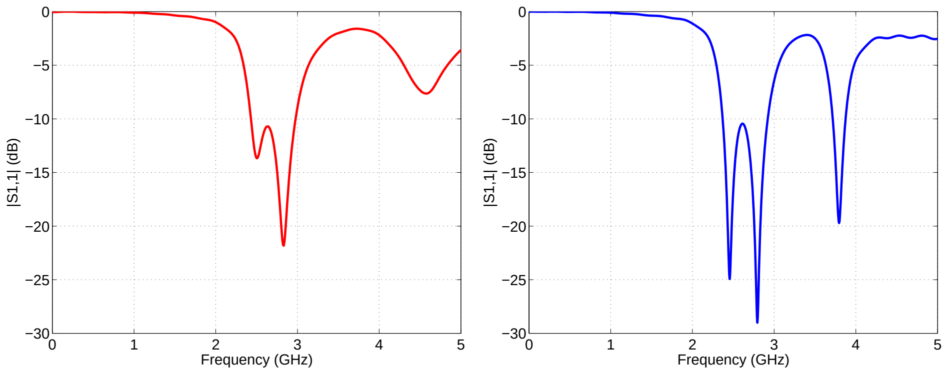

(a) Drop-shaped patch fed at $(\phi_0, \rho_0) = (2.1991, 0.6R_g)$ **(b)** Rectangular patch fed at $(x_0, y_0) = (-13.3, 6.7587)$

Figure 6.17 Frequency responce in terms of return loss when the antenna is fed at the best matching point

The rectangular patch antenna gives linear polarization if the feeding probe point lies on one of the two symmetry axes. When it is fed along the horizontal symmetry axis primarily TM_{10} mode contributes to the radiation. The highest bandwidth achieved under these conditions is 5.5 % at the band with central frequency 2.345 GHz (figure 6.18b). Accordingly, when it is fed along the vertical symmetry axis TM_{01} is responsible for the radiation. In this case, the best matching yields an impedance bandwidth of 7.4 % for the band centred at $2.965\,GHz$.

Similarly, for the drop-shaped patch case, linear polarization can be achieved by feeding the antenna along the symmetry axis x. This gives a maximum impedance bandwidth of $6.5\,\%$ at $2.45\,GHz$ for the feeding point $(\phi_0, \rho_0) = (\pi, 0.2R_g)$ as depicted in figure 6.18a. Due to the asymmetry of patch shape along the y-axis, we have slightly higher cross-polarization level at the $\phi = 90^o$ plane. However, the cross-polarization component at the $\phi = 0^o$ plane is significantly diminished. The corresponding plots are presented in figures 6.21.

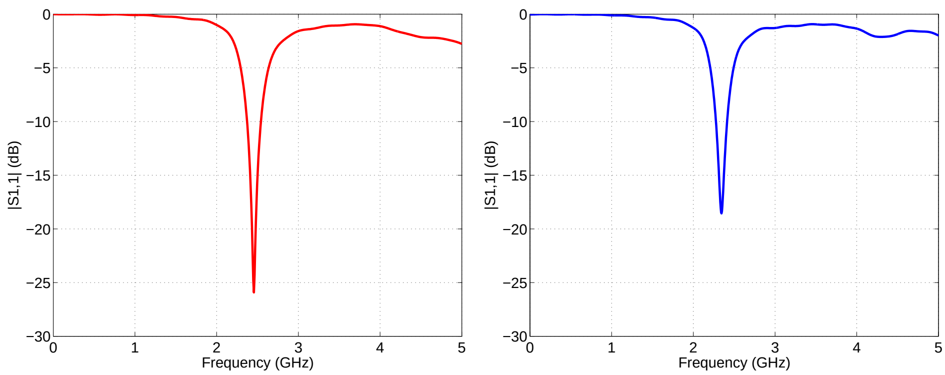

(a) Drop-shaped patch fed at $(\phi_0, \rho_0) = (\pi, 0.2R_g)$

(b) Rectangular patch fed at $(x_0, y_0) = (8.867, 0)$

Figure 6.18 Frequency responce in terms of return loss for linear polarization

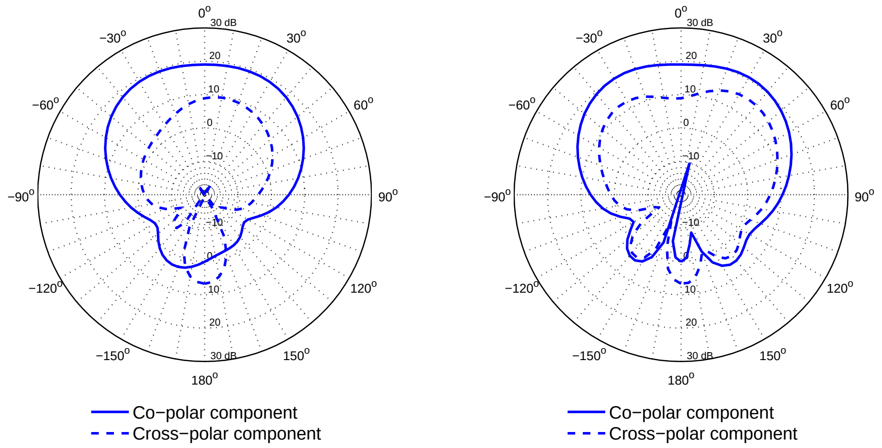

(a) $\phi = 0$ plane

(b) $\phi = 90$ plane

Figure 6.19 Electric field patterns of the circularly polarized drop-shaped patch antenna at $f = 2.65\,GHz$

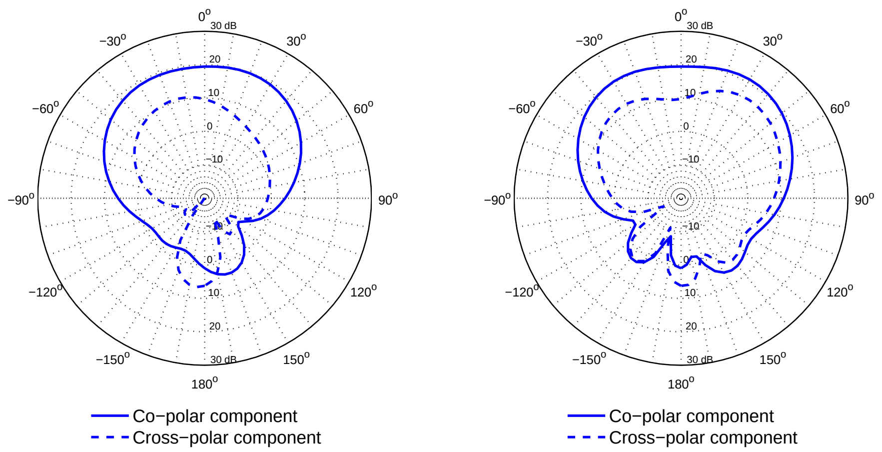

(a) $\phi = 0$ plane

(b) $\phi = 90$ plane

Figure 6.20 Electric field patterns of the circularly polarized rectangular patch antenna at $f = 2.65\,GHz$

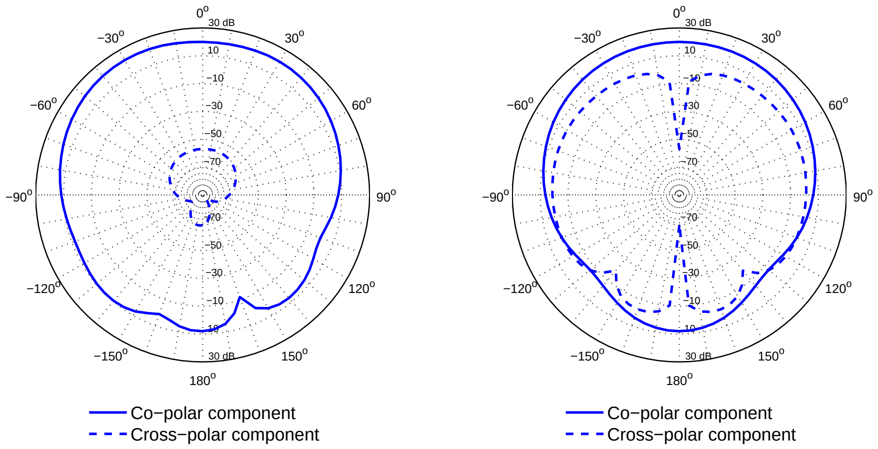

(a) E-plane **(b)** H-plane

Figure 6.21 Electric field patterns of the linearly polarized drop-shaped antenna at $f = 2.45\,GHz$

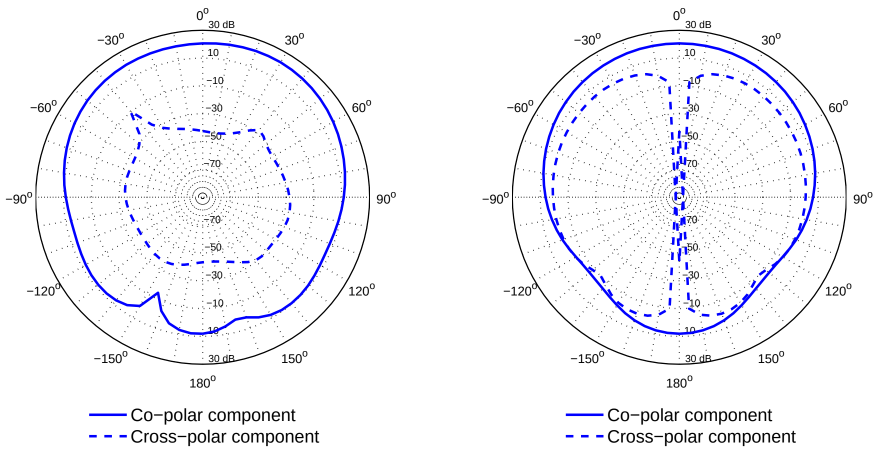

(a) E-plane **(b)** H-plane

Figure 6.22 Electric field patterns of the linearly polarized rectangular patch antenna at $f = 2.345\,GHz$

Chapter 7

The semi-analytical cavity model

7.1 The cavity model principles

As described in section 4.3, the cavity model for the microstrip patch antennas presumes that the region between the microstrip and the ground plane can be treated as a cavity bounded by a magnetic wall along the edge and by electric walls from above and below, under the condition that the substrate thickness h is much less than wavelength λ. Following the general principle of approximation, one may assume that the field structure in the microstrip antenna is essentially the same as that in the cavity. From this, one can compute the radiation pattern, the total radiated power and the input impedance at any feed point.

According to the principles of the model, the close proximity between the microstrip antenna and the ground plane suggests that $\mathbf{E}$ has only the z-component and $\mathbf{H}$ has only the xy-components in the region bound by the microstrip and the ground plane. So, the interior electric field must satisfy the inhomogeneous wave equation

$$\nabla_t^2 E_z + k^2 E_z = j\omega\mu_0 J_z \tag{7.1.1}$$

where $k = \omega\sqrt{\mu_0\epsilon_0\epsilon_r}$ is the wavenumber in the dielectric, J_z is the excitation electric current density due to the feeding probe and ∇_t is the transverse del operator with respect to the z-axis. In addition, the fields must also satisfy

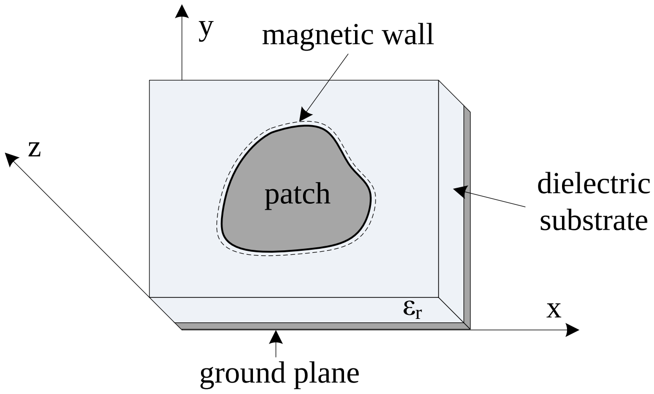

Figure 7.1 General geometry of microstrip antenna

the following boundary conditions:

$$\hat{n} \times \mathbf{E} = 0 \quad \text{on the top and bottom conductors} \tag{7.1.2}$$
$$\hat{n} \times \mathbf{H} = 0 \quad \text{on the magnetic walls} \tag{7.1.3}$$

Here, $\hat{n}$ is the unit outward normal vector with respect to the electric and magnetic conducting surfaces. To solve equation 7.1.1 subject to the boundary conditions, we need to find the eigenfunctions of the homogeneous wave equation

$$\left(\nabla_t^2 + k_{mn}^2\right)\psi_{mn} = 0 \tag{7.1.4}$$

with

$$\frac{\partial \psi_{mn}}{\partial n} = 0 \quad \text{on the magnetic walls} \tag{7.1.5}$$

The solution to equation 7.1.1 expressing the electric field in the patch cavity is

$$E_z(x,y) = \sum_m \sum_n A_{mn}\psi_{mn}(x,y) \quad m,n \in \mathbb{Z} \tag{7.1.6}$$

where A_{mn} are the amplitude coefficients corresponding to the electric field mode vectors or eigenfunctions ψ_{mn}. Assuming the eigenfunctions to be orthogonal, it is proven that the amplitude coefficients are obtained as

$$A_{mn} = \frac{j\omega\mu_0}{k^2 - k_{mn}^2} \frac{\iint J_z \psi_{mn}^* \mathrm{ds}}{\iint \psi_{mn}\psi_{mn}^* \mathrm{ds}} \tag{7.1.7}$$

where ψ_{mn}^* is the complex conjugate of ψ_{mn} and the integration is over the area of the patch s_p.

The resonant frequencies are obtained from setting $k^2 - k_{mn}^2 = 0$ and are given by

$$f_{mn} = k_{mn}/(2\pi\sqrt{\mu_0\epsilon_0\epsilon_r}) \tag{7.1.8}$$

If the frequency f is close to the resonant frequency f_{mn} of a particular mode, the factor $1/(k^2 - k_{mn}^2)$ in equation 7.1.7 is very large and the contribution to E_z, and hence to the radiation field, is due mainly to this resonant mode term.

The interior fields are used to determine the input impedance of the antenna. Input impedance, in the cavity model, is defined as

$$Z_{in} = \frac{V_{in}}{I_{in}} \tag{7.1.9}$$

where V_{in} is the RF voltage at the feed point and is calculated as

$$V_{in} = -E_z h \tag{7.1.10}$$

and the feed current

$$I_{in} = \iint J_z \mathrm{ds} \tag{7.1.11}$$

The preceding procedure will yield the input impedance as purely reactive. Also, at resonance the corresponding coefficient A_{mn} theoretically becomes infinite. To account for these inaccuracies, the permittivity of the dielectric must be be considered complex. The effect of radiation and other losses on the input impedance can be included in the form of an artificially increased dielectric loss tangent.

In the cavity model various types of losses, such as dielectric loss, conductor loss and radiation loss are taken into account by defining an effective loss tangent as

$$\delta_{\text{eff}} = 1/Q = \frac{P_d + P_c + P_r}{\omega_r W_T} \tag{7.1.12}$$

Here, P_d is the power lost in the imperfect dielectric, P_c is the power lost in the imperfect conductors and P_r is the power radiated by the antenna. Surface wave loss can be neglected for thin substrates. W_T is the total energy stored in the patch at resonance ω_r. With the losses described in terms of δ_{eff}, the expression for k^2 is now modified as

$$k^2 = k_0^2\epsilon_r(1 - j\delta_{\text{eff}}) \tag{7.1.13}$$

Substituting 7.1.13 and 7.1.7 into 7.1.6 the following expression for E_z yields

$$E_z = j\omega\mu_0 \sum_m \sum_n \frac{1}{k_0^2\epsilon_r(1 - j\delta_{\text{eff}}) - k_{mn}^2} \frac{\iint J_z \psi_{mn}^* \text{ds}}{\iint \psi_{mn}\psi_{mn}^* \text{ds}} \psi_{mn} \tag{7.1.14}$$

The radiation patterns of a patch antenna is one of the most important characteristics. Since the tangential electric fields on the top and bottom faces, as well as the tangential magnetic field on the vertical surface, are zero, the only contribution to the equivalent sources are the tangential electric field E, on the vertical surface of the cavity. Assuming that the electric field at the perimeter of the patch is known, the equivalence source concept is then used to determine the radiation fields. Together with its image, the total equivalent magnetic current is defined as

$$\mathbf{M}_s = 2\mathbf{E} \times \hat{\mathbf{n}} \tag{7.1.15}$$

where $\hat{n}$ is the unit outward normal. For the surface magnetic current density, the electric vector potential is given by

$$\mathbf{F} = \frac{\epsilon}{4\pi} \iint \mathbf{M}_s \frac{e^{-jk|\mathbf{r}-\mathbf{r}'|}}{|\mathbf{r}-\mathbf{r}'|} \text{ds} \tag{7.1.16}$$

Provided that the substrate thickness h is much less than the wavelength λ, its effect on the radiation field is small and $\mathbf{M}_s$ can be assumed to radiate in free space. Since 7.1.15 is considered to be constant along z, the electric potential at a point r is given by

$$\mathbf{F} = \frac{\epsilon_0 h}{4\pi} \int \mathbf{M}_s \frac{e^{-jk_0|\mathbf{r}-\mathbf{r}'|}}{|\mathbf{r}-\mathbf{r}'|} \text{dl} \tag{7.1.17}$$

where integration is over the perimeter of the patch. The fields in the far-zone are proven to be given by

$$\begin{cases} H_r \simeq 0 \\ H_\theta \simeq -j\omega F_\theta \\ H_\phi \simeq -j\omega F_\phi \end{cases} \tag{7.1.18}$$

$$\begin{cases} E_r \simeq 0 \\ E_\theta \simeq -j\omega\eta_0 F_\phi \\ E_\phi \simeq j\omega\eta_0 F_\theta \end{cases} \tag{7.1.19}$$

where $\eta_0 = \frac{\mu_0}{\epsilon_0}$.

7.2 A semi-analytical approach for super-shape patch antennas

The field estimation based on the cavity model premises the existence of the solutions of the homogeneous Helmholtz equation 7.1.4 under the boundary conditions 7.1.2 and 7.1.3. However, analytical solutions for this equation exist only for a limited number of patch shapes such as rectangle, circle, triangle, ellipse, circular ring, etc. When the patch shape differs from the conventional, like a supershaped patch, then numerical methods might be used to derive the eigenfunctions ψ_{mn} satisfying the equation 7.1.4.

The usage of a tool that numerically calculates the modal eigenvalues and eigenfunctions can provide an overview of the placement of the cutting frequencies of the modes in the spectrum and how this is influenced by the modification of the patch shape. Moreover, the eigenmode analysis provides information about the polarization of the super-shape patch antennas based on the currents excited due to each mode. Also, by using the results regarding the exact electric field excited under the patch derived by the CST transient solver, the modal expansion coefficients 7.1.7 can be calculated, so as the contribution of each mode to the resulting field to be evaluated. In the end, the far-field radiation pattern of a super-shape patch antenna is calculated as a synthesis of the discrete radiation patterns of the mode fields.

Summarizing, this semi-analytical analysis method is aiming at providing a useful physical insight into the operation of the supershaped patch antennas and helps at building a background for the design procedure. For this purpose, the eigenmode solver of *CST microwave studio* is used for the derivation of the mode fields and the mode resonant frequencies. The solution of the eigenvalue equation 7.2.1 for non-driven and loss-free harmonic problems is obtained via the Krylov-Subspace iteration algorithm.

$$\left[\nabla_t^2 + k_{mn}^2\right] \psi_{mn} = 0 \tag{7.2.1}$$

with

$$\frac{\partial \psi_{mn}}{\partial n} = 0 \quad \text{on the magnetic wall} \tag{7.2.2}$$

Each eigenfunction ψ_{mn} can be associated with an eigenvalue k_{mn}^2. The set of eigenfunctions ψ_{mn}, $m, n = 0, 1, \ldots, \infty$ forms an orthogonal basis. This means that

$$\langle \psi_{m_1n_1} \psi_{m_2n_2} \rangle = \iiint \psi_{m_1n_1} \psi_{m_2n_2} \mathrm{dV} = 0 \tag{7.2.3}$$

for $m_1, m_2, n_1, n_2 \in \mathbb{Z}^* \wedge (m_1 \neq m_2 \vee n_1 \neq n_2)$, while the integration is over the volume between the patch and the ground plane. And also

$$\langle \psi_{m_1 n_1} \psi_{m_1 n_1} \rangle = \iiint \psi_{m_1 n_1} \psi_{m_1 n_1} \mathrm{dV} = \|\psi_{m_1 n_1}\|^2 \tag{7.2.4}$$

when $m_1 = m_2 \wedge n_1 = n_2$. Therefore, the total electric field under the patch which has been numerically evaluated from the CST *transient solver* can be expanded in terms of the eigenfunctions ψ_{mn} as follows

$$E = \sum_m \sum_n A_{mn} \psi_{mn} \tag{7.2.5}$$

The expansion coefficients A_{mn} can be easily obtained by multiplying both sides of 7.2.5 with ψ_{mn} and integrating over the cavity volume. Then taking into account the orthogonality properties 7.2.3 and 7.2.4 we find that the expansion coefficients are given by

$$A_{mn} = \frac{\langle E \psi_{mn} \rangle}{\langle \psi_{mn} \psi_{mn} \rangle} = \frac{1}{\|\psi_{mn}\|^2} \iiint E \psi_{mn} \mathrm{dV} \tag{7.2.6}$$

So, for a given feeding probe location and operation frequency we can derive an approximate representation of the expansion coefficient of each mode. This gives us a good picture of the contribution of each mode to the total field.

7.3 The modal analysis

As it is already discussed in section 7.1, a number of conditions must be satisfied in order to apply the cavity model. For this reason the original super-shape patch antennas should be reformed according to the prerequisites of the cavity model.

In particular, the substrate and the ground plane are horizontally confined to the dimensions of the patch as shown in figure 7.2b. Furthermore, a magnetic wall was created ensuring the satisfaction of the condition $H_t = 0$ on it. For the patch and the ground plane PEC (Perfect Electric Conductor) material was used while for the magnetic wall a PMC (Perfect Magnetic Conductor) material was defined. Also the feeding probe was removed in order to have a non-driven resonating cavity, suitable for the eigenmode solver. The first four modes have been evaluated for the supershaped patch antenna derived

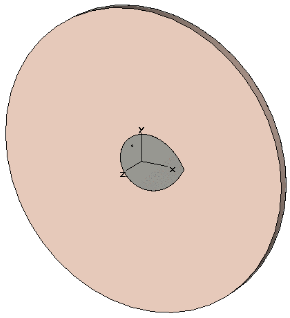

(a) Original model

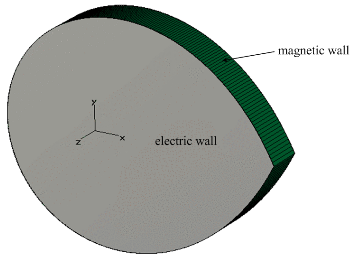

(b) Cavity approximation

Figure 7.2 The original supershaped patch antenna $(a, b, m, n_1, n_2, n_3) = (5.5407, 5.5407, 1, 0.5, 1, 1)$ and its cavity model approximation

for the parameter values $m = 1$, $n_1 = 0.5$, $n_2 = n_3 = 1$. The corresponding normalized electric fields are shown in figure 7.3.

Similarly, the cavity model was applied to the supershaped antenna derived by the parameter values $(a, b, m, n_1, n_2, n_3) = (5.5407, 5.5407, 2, 0.5, 1, 1)$. Therefore, the antennas 7.2 and 7.4 differ only in the parameter m. In figure 7.5, one can observe the shifting in the resonant frequencies occurred by the modification of the parameter m. The decrease of the resonant frequency of TM_{10} and the increase of the frequency of TM_{01} is due to the increase of the horizontal distance and the decrease of vertical distance of the patch respectively. The shift of the other modes can be likewise explained by the change of the radiator dimensions.

Based on the expression 7.2.6, the modal coefficients of the antenna 7.2a in different operating states are calculated and presented in figure 7.6. When the antenna operates at $2.69\,GHz$ and the feed location lies close to the diagonal of the imaginary rectangle enclosing the patch cavity as shown in figure 7.2a, the first two modes are dominant. This can be observed in figure 7.6a. Therefore, due to the orthogonality of these modes, the polarization resulting at the operating band is circular or elliptical.

The expression 7.1.7 denotes that the amplitude of the modal coefficients depends on the operating frequency of the patch antenna as well as the feeding point. In particular, the contribution of a mode increases as the operating frequency is in the vicinity of the cut off frequency of a mode and the feeding probe is placed close to the maximum of the mode field. This is

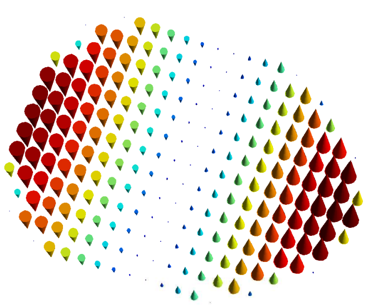

(a) TM_{10} with $f_c = 2.5374\,Ghz$

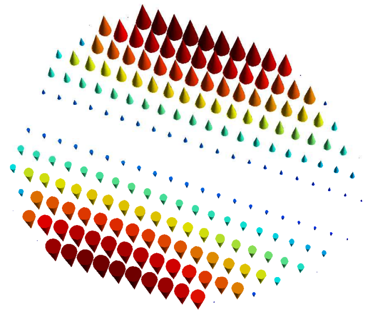

(b) TM_{01} witht $f_c = 3.1181\,Ghz$

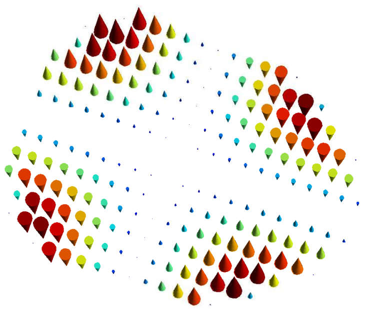

(c) TM_{11} with $f_c = 4.4713\,Ghz$

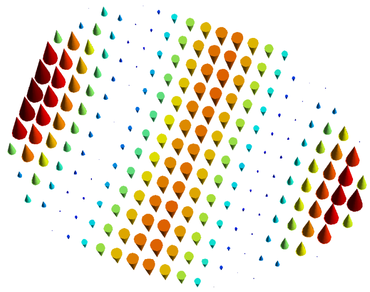

(d) TM_{20} with $f_c = 4.8794\,Ghz$

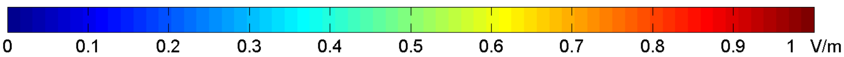

Figure 7.3 Normalized modal electric field configurations of the antenna depicted in 7.2b

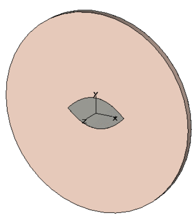

(a) Original model

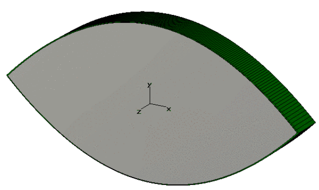

(b) Cavity approximation

Figure 7.4 The original supershaped patch antenna $(a, b, m, n_1, n_2, n_3) = (5.5407, 5.5407, 2, 0.5, 1, 1)$ and its cavity model approximation

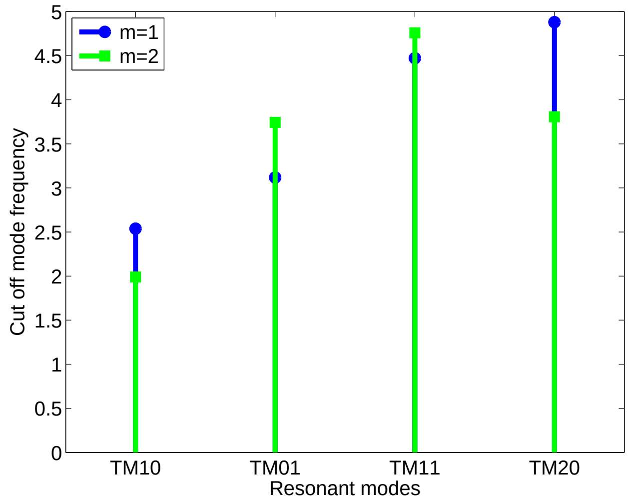

Figure 7.5 The resonant frequency distribution of two supershaped patch antennas $(n_1, n_2, n_3) = (0.5, 1, 1)$

clearly demonstrated in figures 7.6. For example, if the antenna operates at $2.45\,GHz$ and it is fed on the symmetry axis x almost only the fundamental mode 7.3a is excited, as illustrated in figure 7.6b, because the next modes have nulls on the x-axis. In this case, the surface currents induced are mostly parallel to the x-axis yielding a horizontally polarized radiation. Similarly, by properly moving the feeding probe and tuning the frequency figures 7.6c and 7.6d are derived.

7.4 The radiation pattern synthesis

Each mode features a unique current distribution associated with a special radiation pattern. So, the dominance of a mode is also apparent in the radiation pattern of the antenna. This can be demonstrated by recalling the surface magnetic current on the side wall of the cavity. Substituting 7.1.6

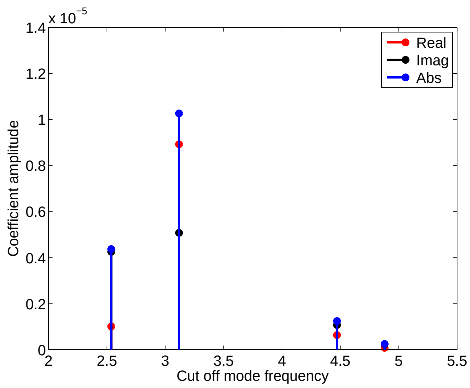

(a) Fed at $\phi = 2.1991$, $\rho = 0.6$ point and operating at $2.7\,Ghz$

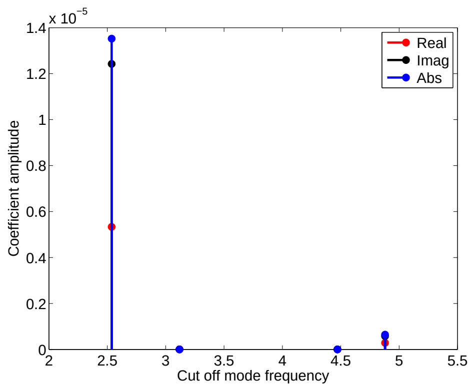

(b) Fed at $\phi = \pi$, $\rho = 0.2$ point and operating at $2.45\,Ghz$

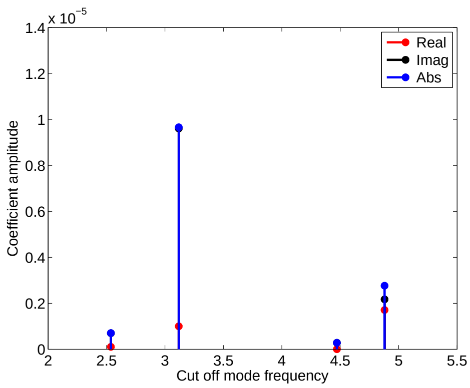

(c) Fed at $\phi = 1.256$, $\rho = 0.9$ point and operating at $3.1\,Ghz$

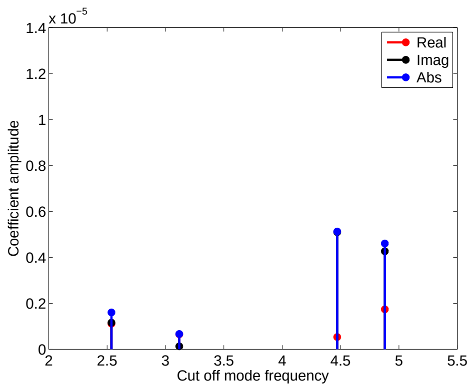

(d) Fed at $\phi = 0.157$, $\rho = 0.9$ point and operating at $4.6\,Ghz$

Figure 7.6 Amplitude coefficients versus cutting frequency of the modes for the super-shape patch antenna $m = 1$, $n_1 = 0.5$, $n_2 = n_3 = 1$

into 7.1.15 we get

$$\begin{aligned}
\mathbf{M}_s =& 2\left(\sum_m \sum_n A_{mn}\psi_{mn}^{\rho=R_g}\hat{\mathbf{z}}\right) \times \hat{\mathbf{n}} \\
=& 2\left(\sum_m \sum_n A_{mn}\psi_{mn}^{\rho=R_g}\right)\hat{\boldsymbol{\tau}} \qquad (7.4.1) \\
=& 2\left(\sum_m \sum_n M_{mn}\right)\hat{\boldsymbol{\tau}} \quad m, n \in \mathbb{Z}
\end{aligned}$$

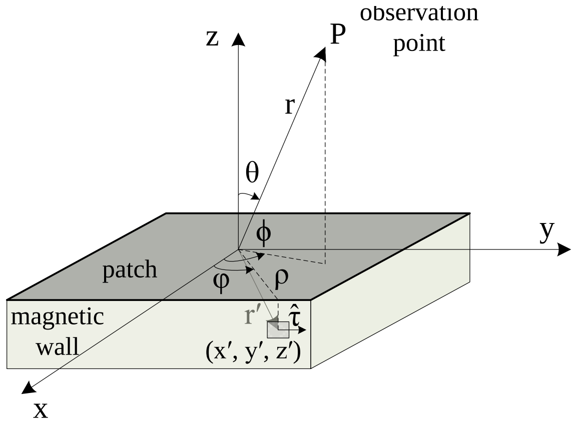

Figure 7.7 Geometry of a patch antenna under the cavity model

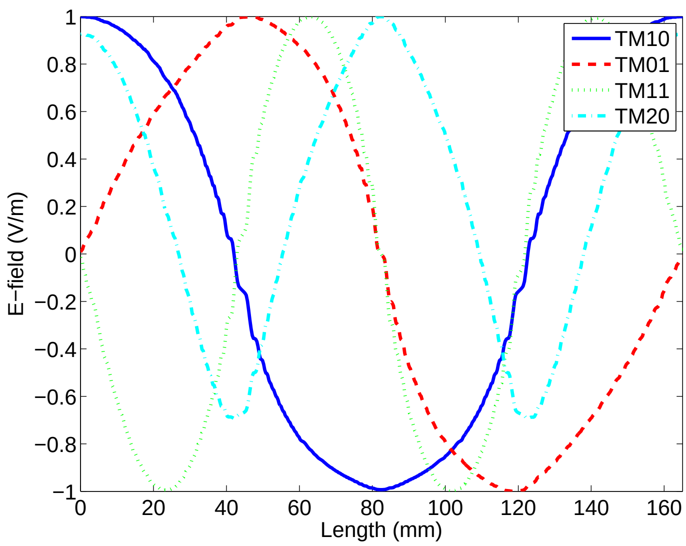

Figure 7.8 Normalized electric field z-component distribution on the side wall of the drop-shaped patch cavity

where $M_{mn} = A_{mn}\psi_{mn}^{\rho=R_g}$ is the equivalent magnetic current density resulting from the electric field configuration of the mn-mode on the periphery of the patch cavity shown in figure 7.8. The unit tangential vector $\hat{\boldsymbol{\tau}}$ with respect to the periphery curve consists of two components and in polar coordinates is expressed as

$$\hat{\boldsymbol{\tau}} = \frac{\xi(\varphi)}{\sqrt{\xi^2(\varphi)+1}}\hat{\boldsymbol{\rho}} + \frac{1}{\sqrt{\xi^2(\varphi)+1}}\hat{\boldsymbol{\varphi}}, \quad \xi(\varphi) = \frac{R_g'(\varphi)}{R_g(\varphi)} \tag{7.4.2}$$

where R_g is the *Gielis* polar equation and R'_g the first derivative of it. Consequently, the total vector potential can be written as

$$\mathbf{F} = \sum_m \sum_n \frac{\epsilon}{2\pi} \iint \left(M_{mn,\rho}\hat{\boldsymbol{\rho}} + M_{mn,\varphi}\hat{\boldsymbol{\varphi}}\right) \frac{e^{-jk|\mathbf{r}-\mathbf{r}'|}}{|\mathbf{r}-\mathbf{r}'|}\mathrm{ds}' \tag{7.4.3}$$

where the integration is over the area of the fictitious magnetic side wall and $|\mathbf{r}-\mathbf{r}'|$ in far-field is given by

$$|\mathbf{r}-\mathbf{r}'| \simeq r - x'\sin\theta\cos\phi - y'\sin\theta\sin\phi - z'\cos\theta \tag{7.4.4}$$

where $x' = \rho\cos\varphi$ and $y' = \rho\sin\varphi$. Since $\mathbf{M}_s$ is expressed in cylindrical coordinates, it has to be transformed to spherical coordinates before delivering the far fields:

$$\begin{bmatrix} M_r \\ M_\theta \\ M_\phi \end{bmatrix} = \begin{bmatrix} \sin\theta\cos(\varphi-\phi) & -\sin\theta\sin(\varphi-\phi) & \cos\theta \\ \cos\theta\cos(\varphi-\phi) & -\cos\theta\sin(\varphi-\phi) & \sin\theta \\ \sin(\varphi-\phi) & \cos(\varphi-\phi) & 0 \end{bmatrix} \begin{bmatrix} M_\rho \\ M_\varphi \\ M_z \end{bmatrix} \tag{7.4.5}$$

In our problem $M_z = 0$. The azimuth and elevation components of the electric vector potential are respectively

$$F_\theta = \sum_m \sum_n \frac{\epsilon}{2\pi} \iint M_{mn,\theta} \frac{e^{-jk|\mathbf{r}-\mathbf{r}'|}}{|\mathbf{r}-\mathbf{r}'|}\mathrm{ds}' \tag{7.4.6a}$$

$$F_\phi = \sum_m \sum_n \frac{\epsilon}{2\pi} \iint M_{mn,\phi} \frac{e^{-jk|\mathbf{r}-\mathbf{r}'|}}{|\mathbf{r}-\mathbf{r}'|}\mathrm{ds}' \tag{7.4.6b}$$

and the radiated far fields are given by the equations 7.1.19. Assuming that $\mathbf{E}_{mn}$ is the radiated electric field due to the mn-mode, it is proven that total far fields are

$$E_\theta = \sum_m \sum_n A_{mn} E_{mn,\theta} \tag{7.4.7a}$$

$$E_\phi = \sum_m \sum_n A_{mn} E_{mn,\phi} \tag{7.4.7b}$$

On that count, the radiation patterns resulting from the modes TM_{10}, TM_{01}, TM_{11} and TM_{20} in a separate basis are given in figure 7.9. For these representations we assume that each time only one mode exists and its modal coefficient equals 1.

At this point, the synthesis of the radiation pattern of the drop-shaped antenna when this is fed at $(\phi, \rho) = (2.1991, 0.6R_g(2.1991))$ and operates at $2.7\,Ghz$ is realized. The corresponding modal expansion coefficients A_{mn}

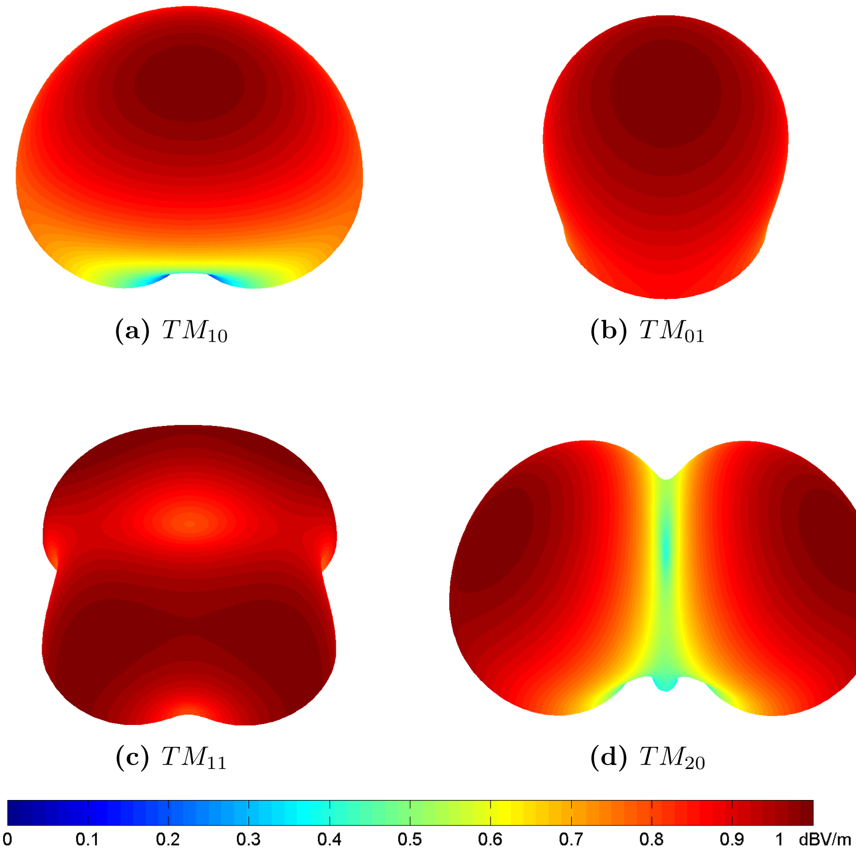

(a) TM_{10} **(b)** TM_{01}

(c) TM_{11} **(d)** TM_{20}

Figure 7.9 Normalized far-field radiation patterns of the first four modes of the drop-shaped patch antenna ($\theta = 30^o$ view)

were calculated from 7.2.6 and presented in figure 7.6a. The patterns are thus created by using 7.4.7b and 7.4.7a.

Apparently, TM_{01} mode is the most dominant in 7.10 while TM_{10} affects the pattern to a smaller extent as it was expected from the expansion coefficient analysis (fig. 7.6a). In 7.10a-7.10b TM_{01} contributes primarily along $\phi = 90^o$ plane while TM_{10} along $\phi = 0^o$ plane. For the E_ϕ component depicted in 7.10c-7.10d, the radiation along $\phi = 0^o$ plane is associated with TM_{01} mode and along $\phi = 90^o$ plane with TM_{10} mode. The mutual involvement of the two modes to the far-field radiation implies that the polarization is either elliptical or circular depending on the values of A_{10} and A_{01}.

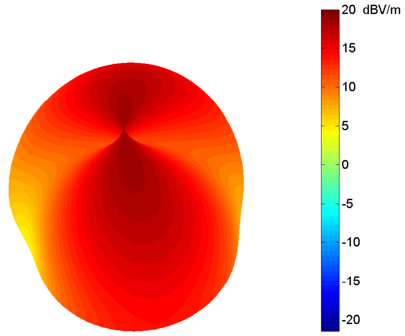

(a) E_θ, $\theta = 30^o$

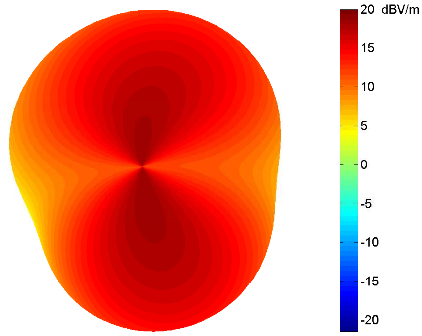

(b) E_θ, $\theta = 0^o$

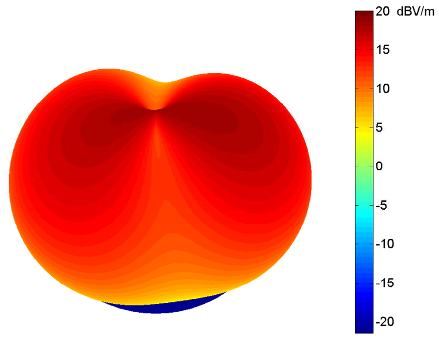

(c) E_ϕ, $\theta = 30^o$

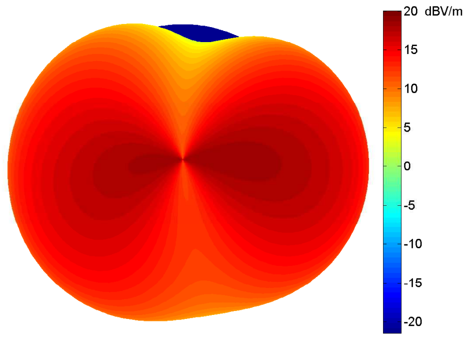

(d) E_ϕ, $\theta = 0^o$

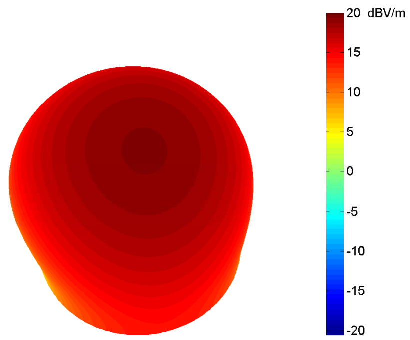

(e) $|E|$, $\theta = 30^o$

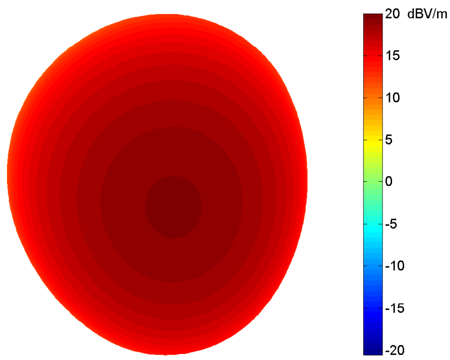

(f) $|E|$, $\theta = 0^o$

Figure 7.10 Electric far-field as a result of modal pattern synthesis of drop-shaped patch antenna

For verification purposes, the drop-shaped antenna was analysed using the full-wave simulator *CST Microwave Studio* and the results of the far-field radiation pattern are shown in figure 7.11. It can be observed that there is a fair convergence of the semi-analytical model to the accurate full-wave method.

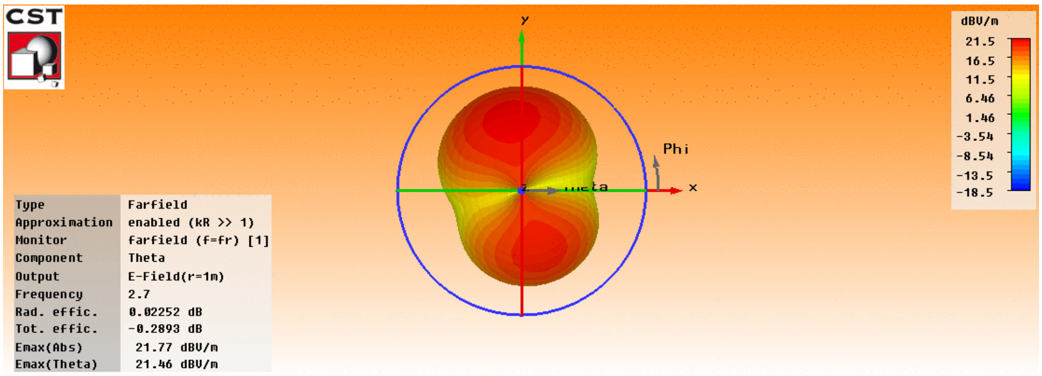

(a) E_θ, $\theta = 0^o$

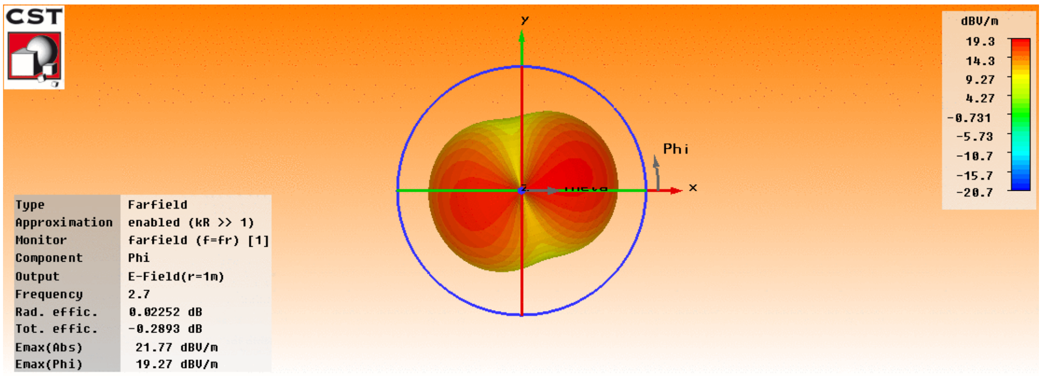

(b) E_ϕ, $\theta = 0^o$

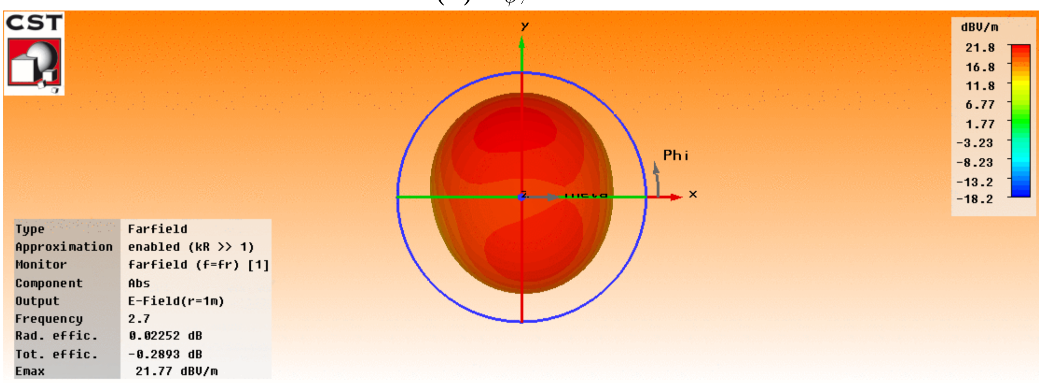

(c) $|E|$, $\theta = 0^o$

Figure 7.11 Electric far-field from CST full-wave simulator

7.5 Summary

The combination of a full-wave time-domain solver and an eigenmode solver provides the possibility of performing a semi-analytical approach to the operation of the irregularly shaped *Gielis* patch antennas. The mode field configurations as well as the cavity resonant frequencies of supershaped antennas could be derived. Also, it was shown how the change of the parameter m affects the distribution of the resonant frequencies to the spectrum. The investigation of the impact of the resonant modes to the radiation pattern over the different operating states in terms of feeding probe location and operating frequency is another feature of this analysis.

The limitations of the model can be attributed to the fact that the substrate thickness of our structure is $h = 6.35\,mm$, that is approximately 5% of free space wavelength. Generally, the accuracy of the cavity model decreases gradually as the substrate thickness exceeds $2-3\%$ of free-space wavelength. In this case, the electric field under the patch does not have only z-component but also x and y components turn up.

The purpose of this study is the deep understanding of the functional principles of the supershaped patch antennas which also helps in the explanation of the simulation results of chapter 6. Although the numerical simulators like *CST* are powerful tools providing a lot of possibilities, they give no physical insight which is necessary for effective antenna design implementations.

Chapter 8

Proposed antenna designs

The rapid development of wireless systems has enforced the simultaneous progression of antenna architecture. The new antenna designs should meet the wideband requirements, have a low profile and be low-cost and easy to fabricate. For these reasons the microstrip patch antennas have become so popular in the last three decades and the researchers' attention aim at the enhancement of their performance in terms of wideband and multiband utilization.

In this chapter two novel *supershaped* antenna designs are proposed, suitable for the most widely used WLAN standards IEEE 802.11$a/b/g/n$ since it is functional in the 2.4 GHz and 5 GHz bands. Specifically, the range of the first band is $2.4 - 2.5\,GHz$ while the second one is $5.1 - 5.8\,GHz$.

Both antennas are using as radiating elements patches generated by the *Gielis* formula which was introduced in previous chapters, appropriately adjusted for dual-band operation. Although *supershape* formula can generate a variety of abstract, natural and artificial geometrical shapes, from an antenna designer's viewpoint only a limited number of them was found to meet specific requirements in terms of desired symmetries, limited edge diffraction, etc. In this respect, we set $\alpha = b$ and $n_2 = n_3$ for both designs and $m = 1$, $m = 2$ for the first and the second configuration respectively. Because of the highly non-linear behaviour and the multi-parametric dependence of the Gielis formula, the selection of the suitable parameter values can be a tedious process. Therefore, a thorough study of the formula and the simulation results of chapter 6 is required.

8.1 The supershaped printed dipole

A dual-band slot-loaded printed dipole antenna for wireless communications is presented. Each flair of the antenna consists of a Gielis supershaped patch featuring a concave ring slot. In particular the parameter set used for the supershape formula is (a, b, m, n_1, n_2, n_3) = (5.74, 5.74, 1, 0.4825, 1.0662, 1.0662). The patch is printed on a dielectric substrate *Rogers RT5880* with $\varepsilon_r = 2.2$ having thickness $h = 9.525\,mm$. The substrate has elliptical shape with x-radius $r_x = 8.6435\,cm$ and y-radius $r_y = 5.929\,cm$.

The novel supershaped printed dipole antenna features a ground plane which results in a unidirectional radiation pattern suitable for WLAN applications, in contrast with the typical bow-tie antenna which has an omnidirectional pattern. Therefore, it is a simple planar structure that can be integrated in a MMIC board. The antenna is differentially fed through a circular slot in the ground plane by two plated-through hole (PTH) pins with characteristic impedance $Z_c = 100\,Ohm$. This is another attractive feature that makes it suitable for MMIC integration. In case of unbalanced input signal, a balun transformer is needed to be adapted.

The antenna is developed, optimized and simulated with the *CST Microwave Studio*. The general geometry and the coordinate system is presented in figure 8.1. The frequency response is shown in figure 8.2 where we can see that the bandwidth is more than sufficient in the bands $2.4/5\,GHz$ since its range is $2.2 - 2.77\,GHz$ and $4.53 - 6.96\,GHz$ respectively. So, it consists a wideband antenna with frequency ratio f_2/f_1 greater than 2/1.

The design steps followed include, firstly, the derivation of the parameter α from an optimization procedure. Through this parameter we control the size of the patch and consequently the low band resonance. Parameters n_1, $n_2 = n_3$ were also optimized aiming at higher bandwidth performance. Then, the gap width d_s as well as the circle center x_s coordinate have been optimized for creating the high band. Moreover, a stub of width $w_s = 1.88\,mm$ and length $l_s = 3.5\,mm$ was placed for matching reasons.

The typical bow-tie antenna is known to be wideband since it has many adjacent resonances. The concave ring slots have been introduced in order to form and center the two bands through the control of the current path and thus the perturbation of the frequency resonances. The best value of the gap width $d_s^{opt} = 5\,mm$ is derived from the optimization procedure and

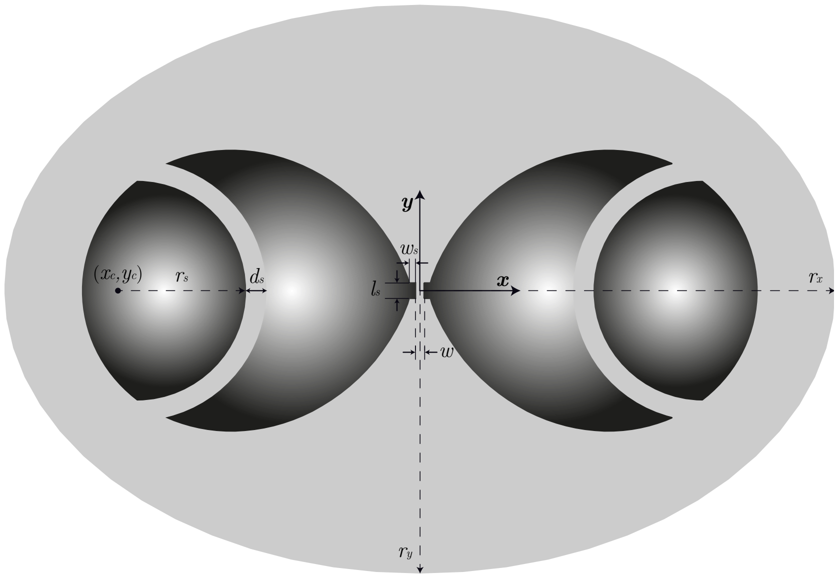

(a) Top view

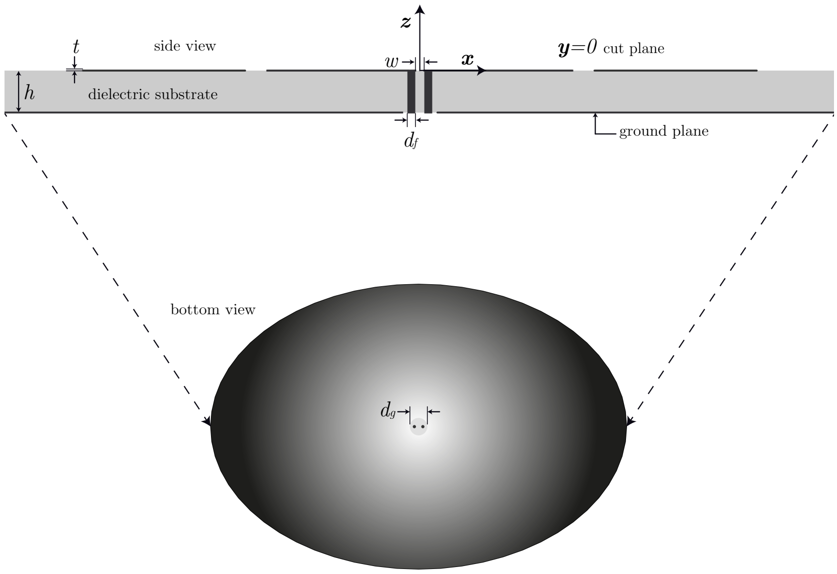

(b) Side and bottom view

Figure 8.1 Geometry of the supershaped printed dipole antenna. Structure characteristics: $h = 9.525\,mm$, $t = 0.068$, $(x_c, y_c) = (65\,mm, 0\,mm)$, $r_s = 25\,mm$, $d_s = 5\,mm$, $r_x = 8.643\,cm$, $r_y = 5.929\,cm$, $l_s = 3.498\,mm$, $w_s = 1.88\,mm$, $w = 5.253\,mm$, $d_f = 1.82\,mm$, $d_g = 8\,mm$.

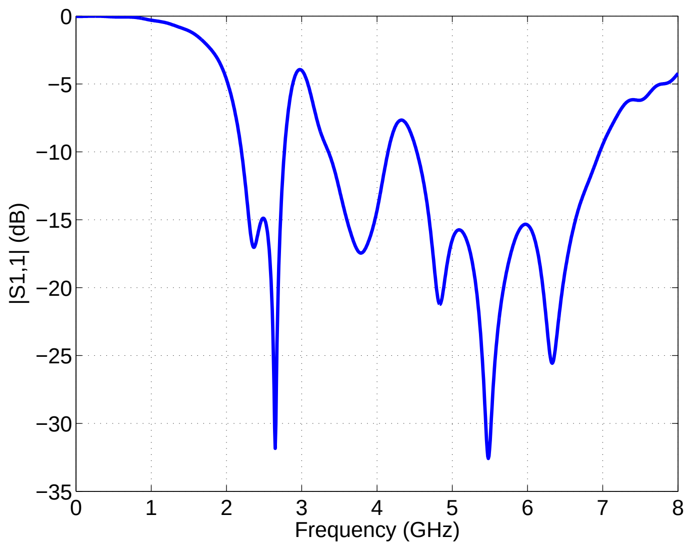

Figure 8.2 Return loss of the supershaped bow-tie patch antenna

the corresponding frequency response is presented in figure 8.2. The effect of the slots was investigated by varying the gap width d_s and the results are presented in figure 8.3. In the low frequency band the slot retains the conduction current in the central part of the antenna while the displacement current flows at the side parts of the antenna. Also, as seen in figure 8.4, most of the current flows in the discontinuities of the structure and the path that follows determines the resonant frequency.

The effect of the slots depends mainly on the current distribution of the unperturbed resonances. The first resonance observed in the graph is mostly attributed to the conduction current flowing along a shortened path in the central part of the antenna. The diminished electrical length of the antenna results in a right-hand displacement of the resonant frequency. As the width of the gap increases the capacitance due to the slots decreases allowing less current to flow towards the edges and moving the resonant frequency to the right. The corresponding current distribution in the frequency $f_1^l = 2.36\,GHz$ is presented in figure 8.4a. In the second mode the current in the side parts is significant. In this case the resonant frequency has been shifted to the left because the air gap increases the electrical length of the structure. Figure 8.4b shows the current distribution in the resonant frequency $f_2^l = 2.65\,GHz$. It can be observed that the slots have a greater effect on the first mode since the current at the slots location for this mode (figure 8.6a) is larger compared to the current in the second mode (figure

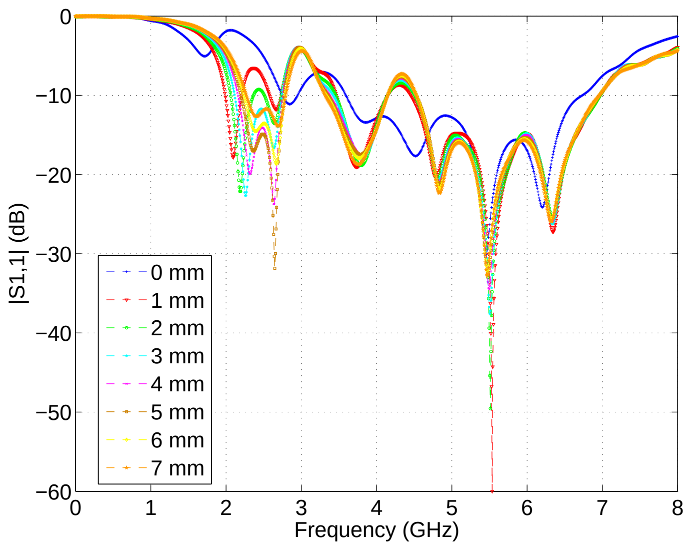

Figure 8.3 Return loss for different d_s slot widths

8.6b).

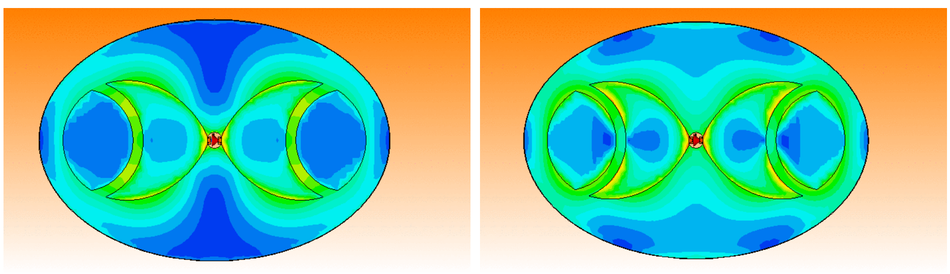

(a) $f = 2.36\,GHz$ **(b)** $f = 2.65\,GHz$

Figure 8.4 Surface current in the two resonant frequencies composing the low band

The high frequency band consists of three resonances in the frequencies $f_1^h = 4.832\,GHz$, $f_2^h = 5.5\,GHz$ and $f_3^h = 6.328\,GHz$. The three modes are derived by perturbation of the original modes caused by the slots. However, in higher frequencies the antenna is electrically longer and the current is mostly concentrated in the center. Figures 8.6 show the surface current distribution of the original unperturbed modes. Therefore, we have less current at the slot locations so the shifting of the resonant frequencies is smaller compared to the low frequency. Also, it can be noticed in figures 8.5 presenting the surface current distribution in the high frequency resonances that the

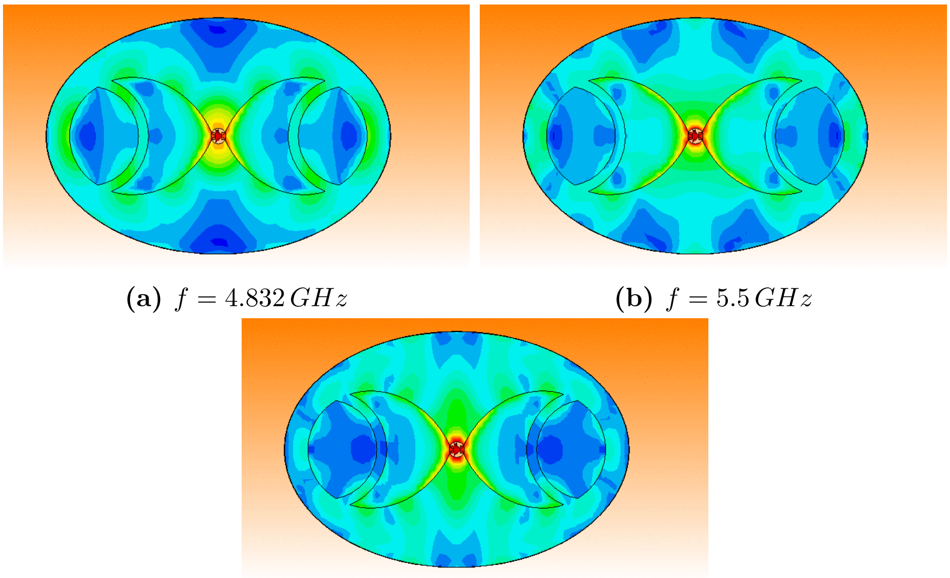

(a) $f = 4.832\,GHz$ **(b)** $f = 5.5\,GHz$ **(c)** $f = 6.328\,GHz$

Figure 8.5 Surface current in the three resonant frequencies composing the high band

fringing current in the slots is diminished. This is because the capacitance in series formed by the slot forms a high-pass filter. This means that in high frequencies the relevant impedance reduces till there is virtually no gap. So, both conduction current and displacement current are flowing there.

Figure 8.7 illustrates the realized gain far-field patterns in the central frequencies of the low and high band. Dipole antennas feature a omnidirectional radiation pattern which is a limitation for applications requiring unidirectional pattern like as downward and sideward WLAN access points. This problem is resolved here by the placement of a ground plane in order the antenna to be effectively used in such kind of applications. The introduction of a ground plane to a printed dipole-like antenna was achieved by implementing the *current delay technique*. Specifically, the substrate height was chosen so as to approximately equal $\lambda_h/4$ for the high frequency band and $\lambda_l/8$ for the low frequency band. However, in order to compensate for the $\pi/2$ phase difference in the $2.4\,GHz$ band we "delay" the current in the patch via the insertion of the slots. As explained above, the gaps affect mostly the low frequency band forcing displacement current to flow at the gaps. This effect causes the total delay in the current flow at the low frequency band, thus, the phase difference reduces to less than $\pi/2$.

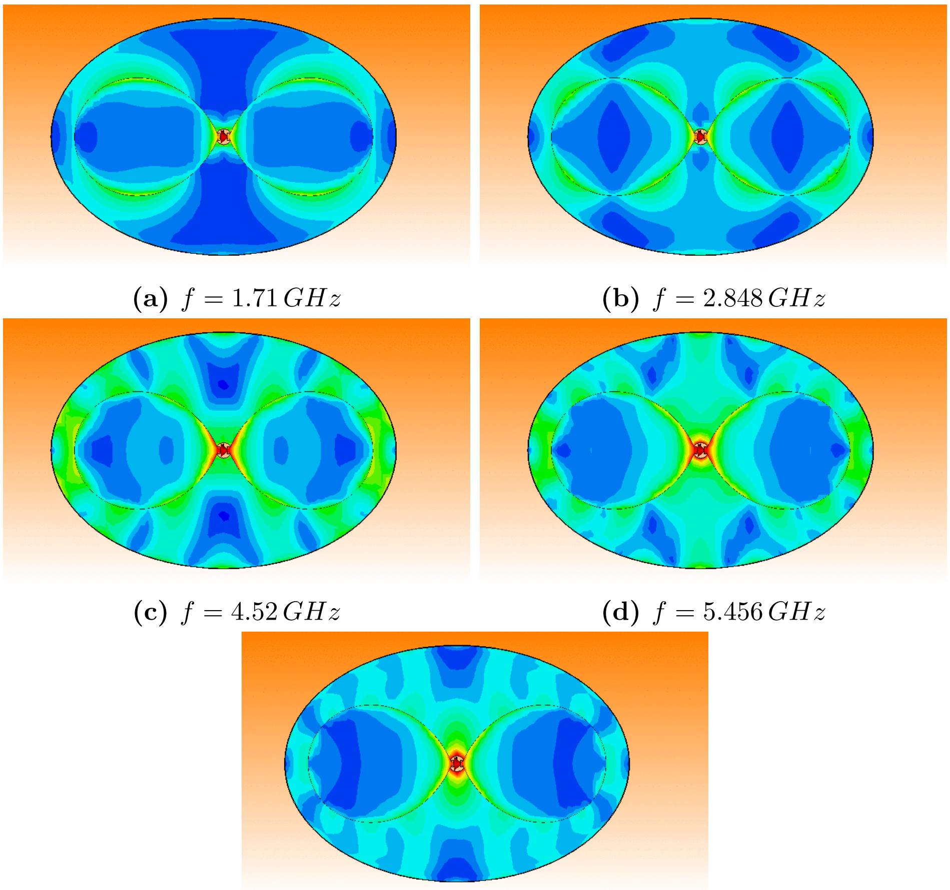

(a) $f = 1.71\,GHz$

(b) $f = 2.848\,GHz$

(c) $f = 4.52\,GHz$

(d) $f = 5.456\,GHz$

(e) $f = 6.2\,GHz$

Figure 8.6 Surface current amplitude of the supershaped bow-tie antenna without slot loading ($d_s = 0\,mm$)

As observed in the figures, the patterns are unidirectional and broadside making the antenna a suitable solution for WiFi applications. It should be noticed that the back radiation observed mainly in the $5\,GHz$ band is expected to be vanished by the extension of the ground plane dimensions. The maximum realized gain for the lower and upper band are $RG_l = 9.91\,dB$ and $RG_l = 5.4\,dB$ respectively. Pure linear polarization is achieved and, as we can see, the cross polarization levels are extremely low. Specifically, they drop down more than $160\,dB$ as shown in figure 8.8. This occurs because the configuration is perfectly symmetrical along both axes. Furthermore, high radiation frequency for both bands was obtained, that is 98.5% for the $2.4\,GHz$ band and 99.1% for the $5.5\,GHz$ band.

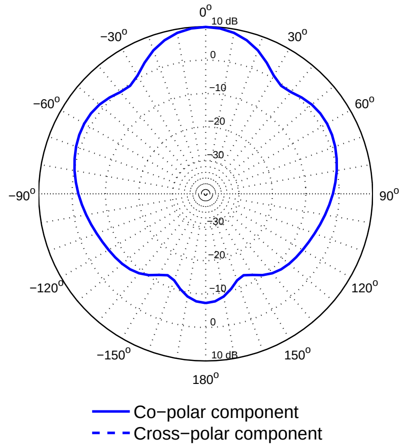

(a) E-plane, $f = 2.45\, GHz$

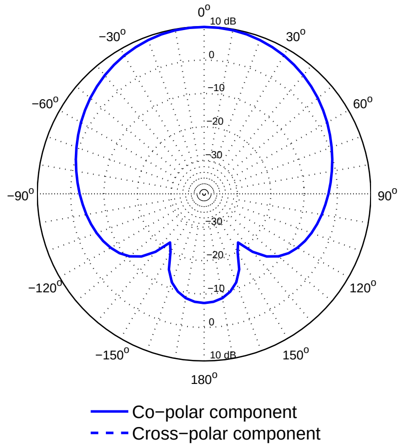

(b) H-plane, $f = 2.45\, GHz$

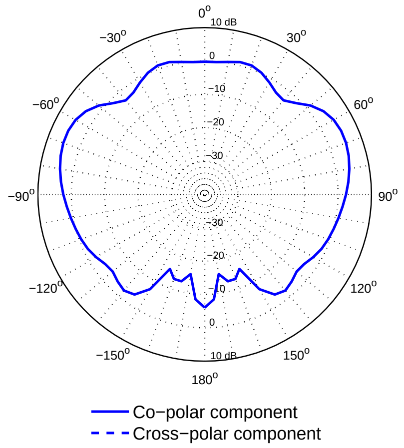

(c) E-plane, $f = 5.45\, GHz$

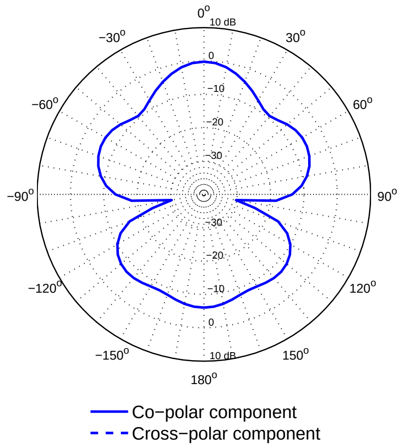

(d) H-plane, $f = 5.45\, GHz$

Figure 8.7 Realized gain far-field patterns of the supershaped bow-tie antenna in the central frequencies of the two bands

8.2 The supershaped ring slotted antenna

The second proposed design is a ring slotted patch antenna fed through a coaxial feeding probe. The antenna consists of an elliptically shaped metallic patch with a supeshaped annular slot and a smaller supershaped slot centrally positioned. The annular slot practically creates two concentric patch

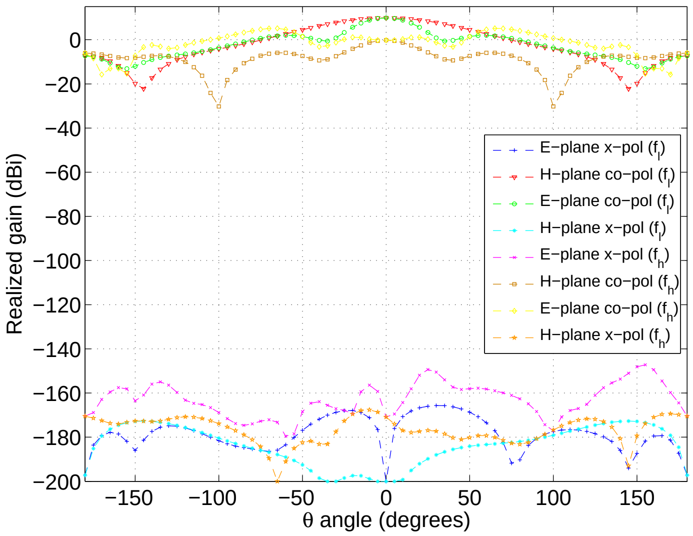

Figure 8.8 Radiation patterns in the low (f_l) and high (f_h) band

elements, the inner one of them is fed along the horizontal symmetry axis via a SMA connector. The patch is mounted on an elliptical dielectric substrate placed on an elliptical ground plane. The antenna structure is displayed in figure 8.9. Similarly to the first proposed configuration, also this antenna is operable in the WLAN bands $2.5/5\,GHz$.

The inner C_{r_i} and the outer C_{r_o} curve forming the annular slot, as well as the periphery C_c of the smaller central slot, have been generated by the supershaped formula by properly adjusting the relevant parameters. All the slot outlines have the same profile but a different scaling factor that is determined by the parameters α, b. These parameters were estimated with the help of the *CST* optimization tool. The substrate dielectric material is the lossy *Rogers Duroid 5880* with dielectric constant $\varepsilon_r = 2.2$. The coaxial feeding probe is filled with lossy *Teflon* with permittivity $\varepsilon_{r_p} = 2.1$ and has a characteristic impedance $Z_c = 50\,Ohm$. The inner conductor diameter of the coaxial connector is increased through the plated-through hole (PTH) technology to $1.8\,mm$ along the inserted section of the pin for reducing the introduced inductance.

As it is observed in 8.10 frequency response figure, the antenna by covering the bands $2.35 - 2.52\,GHz$ and $5.12 - 5.94\,GHz$ meets fully the frequency requirements of the IEEE $802.11a/b/g/n$ standards. Apparently, this antenna structure exhibits frequency selectivity, high quality factor and thus increased sensitivity which is critical for multipath indoor environments.

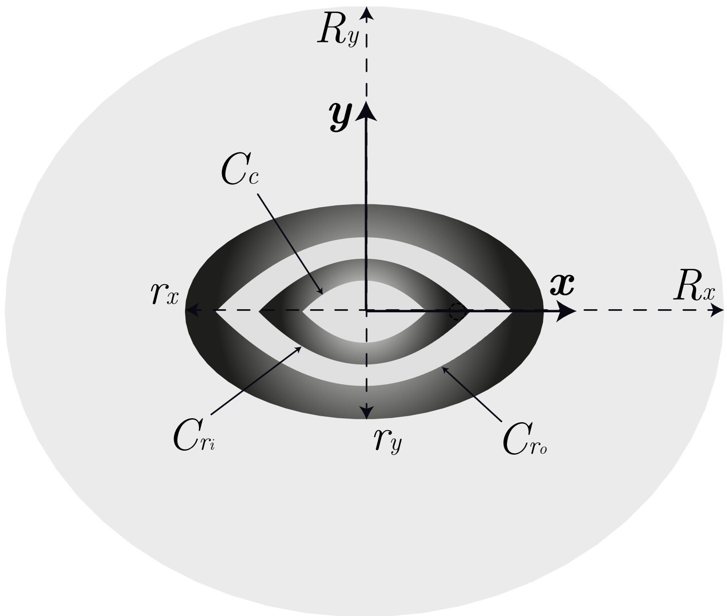

(a) Top view

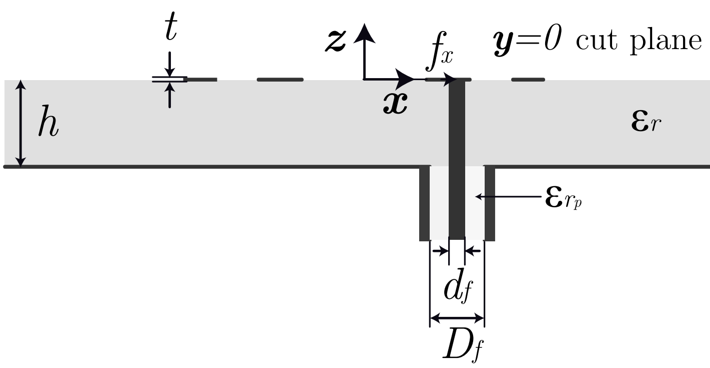

(b) Side view

Figure 8.9 Geometry of the supershaped ring slotted antenna. Structure characteristics: $R_x = 39.675\,mm$, $R_y = 33.723\,mm$ $r_x = 19.796\,mm$, $r_y = 11.877\,mm$, $\varepsilon_r = 2.2$, $h = 9.525\,mm$, $t = 0.07\,mm$, $f_x = 10.263\,mm$, $\varepsilon_{r_p} = 2.1$, $d_f = 1.28\,mm$, $D_f = 4.28\,mm$, C_c: $(a, b, m, n_1, n_2, n_3) = (2.618, 2.618, 2, 0.5, 1, 1)$, C_{r_i}: $(a, b, m, n_1, n_2, n_3) = (3.418, 3.418, 2, 0.5, 1, 1)$, C_{r_o}: $(a, b, m, n_1, n_2, n_3) = (4.05, 4.05, 2, 0.5, 1, 1)$.

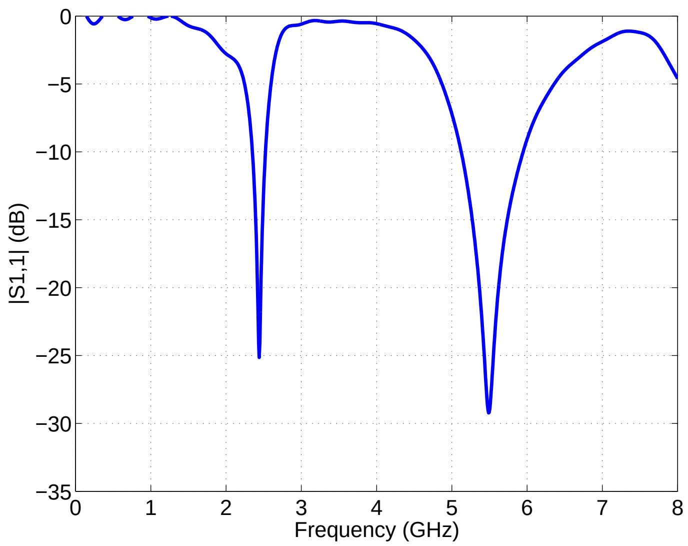

Figure 8.10 Return loss of the supershaped ring slotted patch antenna

The low resonance is mostly attributed to the outer element while the high resonance basically to the smaller inner part of the antenna as it was expected. This can be seen in the surface current figures 8.11. As it is known, the annular slot introduces additional resonances which contribute to the extension of the frequency bands. The key point is to balance properly the annular slot width so as to achieve the required radiation frequencies and bandwidth characteristics. This is done by tuning the values of α, b parameters involved in the supershape formula producing the curves C_c, C_{r_i} and C_{r_o}. The effect of the variation of the C_c curve is presented in figure 8.12. Here, it can be observed that the size of the inner slot doesn't perturb much the resonant frequencies because there is not much current along this edge. However, as α, b increase, the resonant frequency shifts slightly to the left because of the consequent increase of the current path. Figures 8.13 and 8.14 demonstrate the effect of the variation of α, b in the antenna frequency response. The scaling of the contour C_{r_i} influences the size of the inner patch as well as the width of the ring slot. It is observed that it has a strong effect on the central frequency of the high band since much current flows along C_{r_i}. Moreover, as the slot width decreases, an increase in the low band frequency is noticed which indicates the contribution of the ring slot also to the low frequency resonance. According to figure 8.14, the scaling of the curve C_{r_o} through the variation of the relevant parameters causes a perturbation of both resonances as well. Namely, the increase of α, b results in a left-hand shifting of the low resonance frequency due to the increase of the current path in this frequency and a right-hand shifting of the high resonance frequency since the slot width increases. In this way, we can obtain a frequency ratio f_h/f_l that ranges approximately from 1.3 to 3.

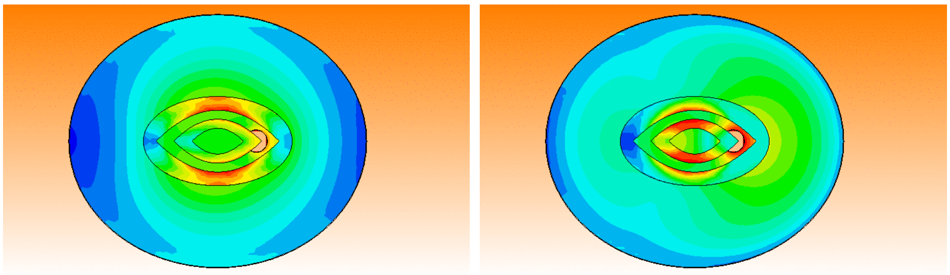

(a) $f = 2.45\,GHz$ **(b)** $f = 5.45\,GHz$

Figure 8.11 Surface current in the low and high frequency band of the ring slotted antenna

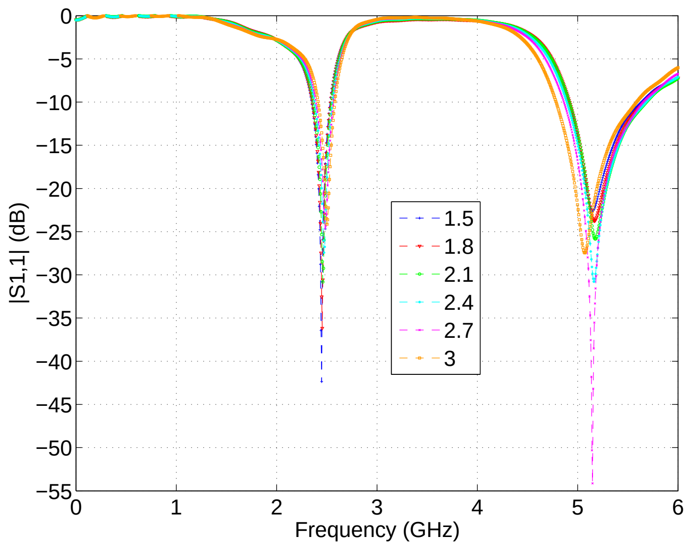

Figure 8.12 Return loss for different a, b parameters controlling the inner slot (C_c curve) size

The radiation patterns in terms of the realized gain are presented in figure 8.15. As can be observed, the antenna features linear polarization and broadside radiation patterns. The maximum realized gain for the lower band is $RG_l = 6.84\,dB$ and for the upper band $RG_u = 7.08\,dB$. Additionally, it exhibits high radiation efficiency which is of the order of 94.4% for the low

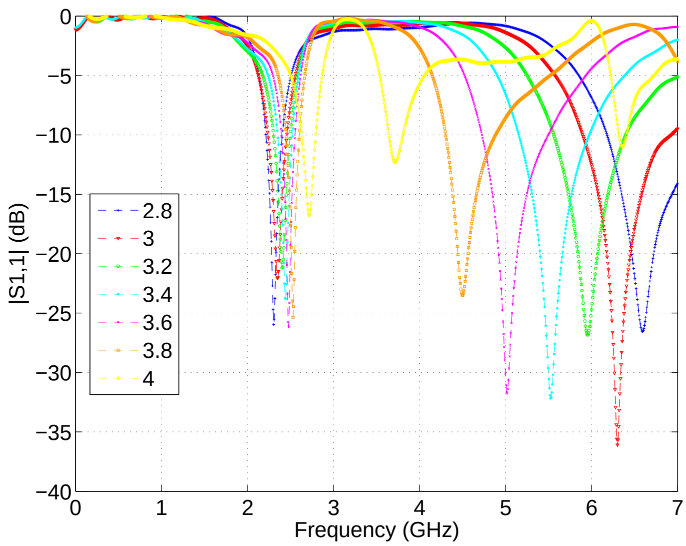

Figure 8.13 Return loss for different a, b parameters controlling the annular slot size by tuning the size of the inner curve (C_{r_i})

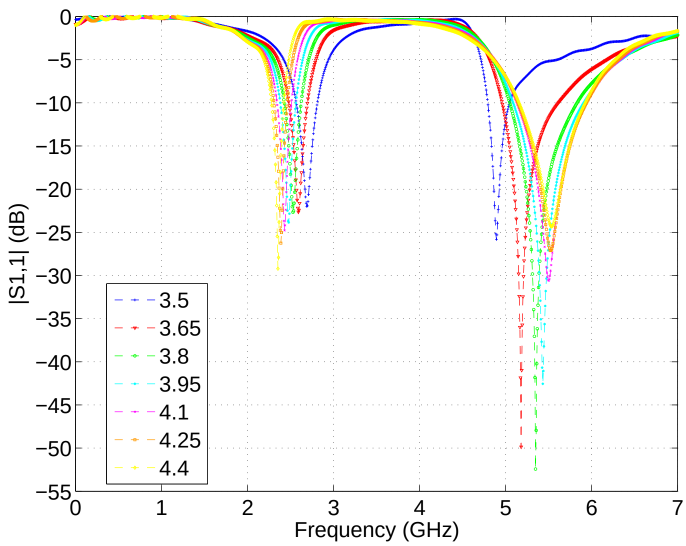

Figure 8.14 Return loss for different a, b parameters controlling the annular slot size by tuning the size of the outer curve (C_{r_o})

band and 98.8% for the high band.

Moreover, it can be noticed that in the $\varphi = 0$ plane the cross-polarization field is so low that it is hardly distinguished. This is due to the perfect symmetry of the antenna along the x-axis.

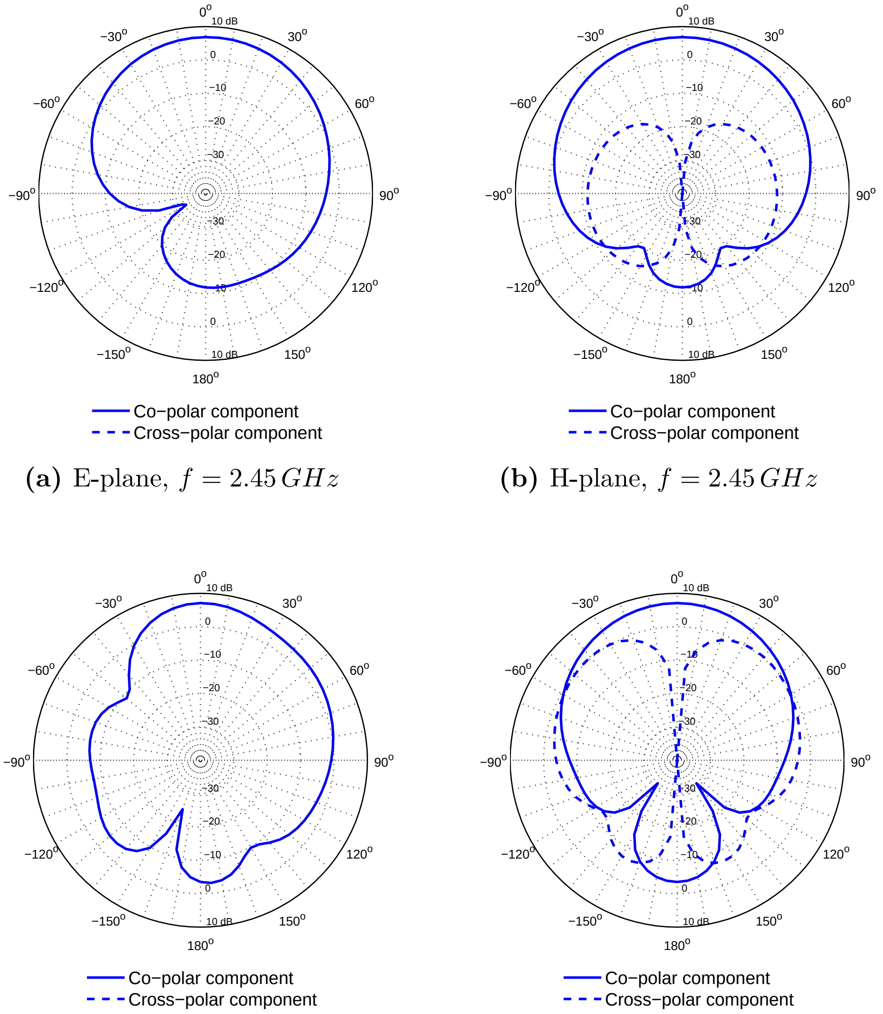

(a) E-plane, $f = 2.45\,GHz$ **(b)** H-plane, $f = 2.45\,GHz$

(c) E-plane, $f = 5.45\,GHz$ **(d)** H-plane, $f = 5.45\,GHz$

Figure 8.15 Realized gain far-field patterns of the supershaped ring slotted antenna in the central frequencies of the two bands

8.3 Relevant studies

The printed dipole antenna is a popular alternative among the patch antenna solutions because of the wideband operation and the pure linear polarization characteristics. With the proper modifications it can be transformed also into a dual-band or multi-band patch antenna. In the past, the printed dipole antenna has been chosen by researchers as an implementation of the WLAN technology.

In 2000 Suh et al. [50] proposed a printed dipole antenna with bi-directional radiation for operation at 2.4 and 5.2 GHz bands. A printed dipole antenna with U-slotted arms was presented by Su et al. in 2002 [51]. This omni-directional antenna was designed for WLAN applications at 2.4 and 5.2 GHz bands. Zhang et al. [52] studied in 2005 a dual-band WLAN dipole with a matching network which operated at 2.4 and 5.5 GHz. One more printed dipole for the WLAN bands 2.4 and 5.5 GHz was proposed by Zhang et al. in 2011 [53]. This L-slotted dipole achieves a good matching for a wide range of frequencies in the two bands. A dual-/triple-band operation of an asymmetric dipole antenna was demonstrated by Sim et al. in 2013 [55]. The proposed design was intended for a WLAN operation in the bands 2.4/5.2/5.8 GHz.

Compared to the aforementioned designs, the supershaped printed dipole consists a novel improved solution for the wireless LAN technology since it is compatible with the most widely used IEEE WLAN standards, has extremely low cross-polarization levels and features a uni-directional radiation pattern after the successful introduction of a ground plane. This makes it a suitable solution for a WLAN access point mounted on a surface, such as a ceiling.

The annular-ring-slotted circular disk microstrip antenna was proven analytically since 1990 [56] to have dual resonance frequencies. Specifically, one resonance is higher than the natural resonance of the annular ring antenna and the other resonance is lower than the natural resonance of the circular-disk antenna. The difference depends on the mutual coupling between the two patches.

In [57] the annular-ring microstrip antenna is studied in terms of the gap length and the feed point. The antenna was found to exhibit frequency tunability with the gap. Another dual-band gap coupled annular ring microstrip antenna is proposed in [58]. The operational bands are situated at 5.2 and 6.1 GHz. Finally, an annular ring slot microstrip antenna for wireless applications was presented by Singh et al. in 2013. The resonant frequency bands are in 0.6/1.6/2.2/2.7 GHz.

The supershaped ring slotted antenna achieves a higher frequency ratio and a larger bandwidth compared to the above antenna configurations. Furthermore, through the variation of the slot width a frequency ratio tuning can

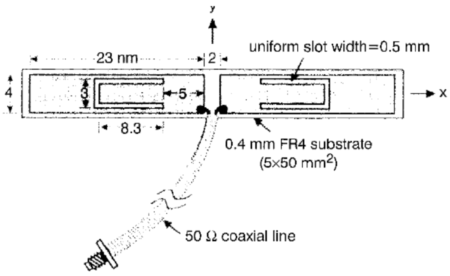

(a) Geometry of [51]

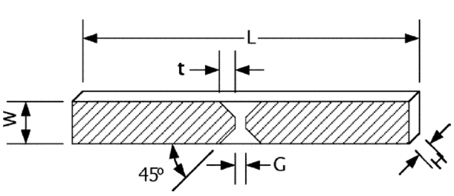

(b) Diagram of [52] printed dipole

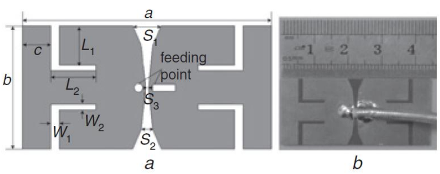

(c) Structure and photograph of antenna [53]

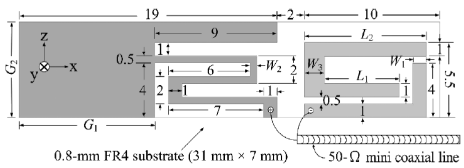

(d) Geomtery of the asymmetric dipole in [55]

Figure 8.16 Printed dipole antenna configurations proposed in the past for WLAN operation

be achieved. Finally, the broadside radiation patterns makes it a strong candidate for WLAN applications.

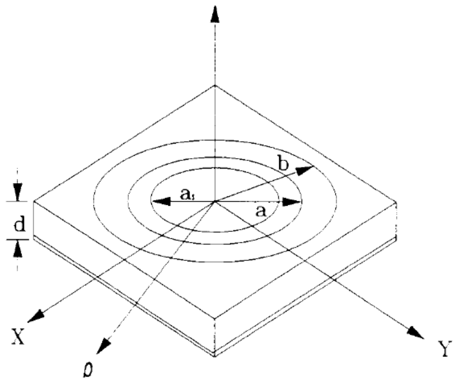

(a) Geometrical configuration of [56]

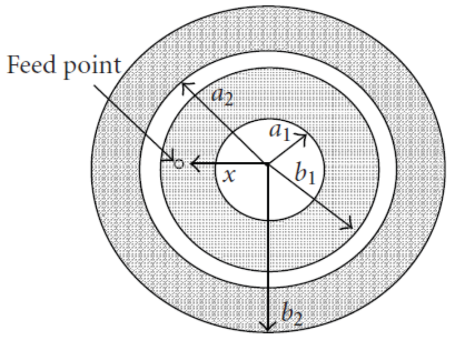

(b) Concentric annular ring of [57]

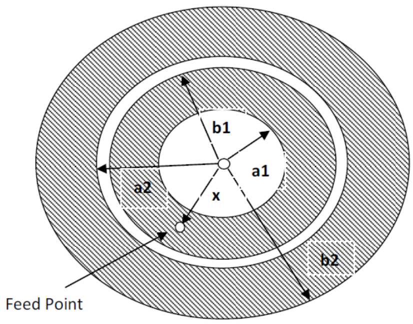

(c) Gap coupled annular ring antenna [58]

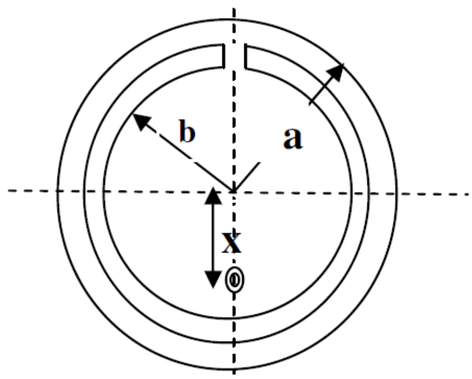

(d) Geomtery of design [59]

Figure 8.17 Dual-band annular ring slotted antennas

Chapter 9

Conclusions and recommendations

9.1 Conclusions

In this project, a mathematical relation know as *Gielis* or supershape formula was introduced in the field of microstrip patch antennas. The variation of the parameters involved in the equation resulted in some naturally inspired patch shapes. The patch antennas generated in this way were simulated by means of the commercial software *CST Microwave Studio* and the outcomes regarding the fractional bandwidth as a function of the feeding probe, the realized gain, the surface current distribution and the radiation patterns were analysed and evaluated.

Thereafter, an approximate model based on the cavity model theory was built and simulated with the help of the *CST* eigenmode solver. From this analysis we extracted the resonant frequencies and the field configurations of the first modes of the structures. Then, by combining the numerical results from the transient solver with that coming from the eigenmode solver we calculated the contribution of each mode in a certain operating state determined by the feeding probe location and the operating frequency. Useful conclusions were made from this analysis concerning the resonant mode distribution and thus the polarization of the supershaped patch antennas.

From these two investigation steps, it was concluded that the alteration of the radiator shape redistributes the resonant frequencies of the antenna. This is explained from the fact that the resonant frequency depends on the geometric characteristics of the patch antenna which determines the surface current path. In general, the current concentrates at the discontinuities of the structure, so it flows at the edges of the metal patch. In the rectangular patch case the current path distance coincides with the length of the rectangle which equals about $\lambda/2$, where λ is the wavelength in the dielectric for the first resonant mode. In an irregularly shaped patch antenna, like a supershaped antenna, the resonant mode is determined mostly from the periphery length of the patch. Therefore, even for the same patch area, the resonant frequencies of two differently shaped patch antennas may differ significantly. Figure 9.1 shows the S_{11} coefficient of two supershaped patch antennas which differ in the parameter m.

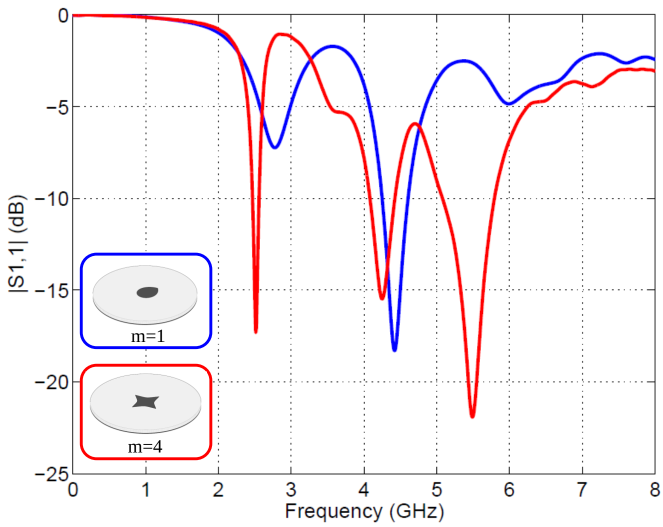

Figure 9.1 Frequency response of two supeshaped patch antennas with $(n_1, n_2, n_3) = (0.5, 1, 1)$ and fed at $(\phi_0, \rho_0) = (0, 0.8R_g)$

As far as concerns the fractional bandwidth, it can be observed in the section 6.5 that the modification of the shape can slightly increase it. The different configuration of the field in the antenna might result in a matching for a little bigger range of frequencies. However, this does not consist a significant enhancement of the bandwidth.

The supershaped patches can be the starting point for UWB and multiband designs with high performance standards resulting from the proper elaboration of the equation parameters and the geometrical characteristics of the introduced features (slots, coplanar/stacked patches, feeding mechanism, etc.). In the design process, the biggest challenge is the selection of the right *Gielis* shape. On consideration of low cross polarization and limited edge diffraction, only a limited number of them can be used for antenna design purposes. The shape determination is a complicated process because the multi-parametrization and especially the non-linear behaviour of the equation makes it sharply burst or shrink with small variations of the parameters. Therefore, a careful examination and deep understanding of the simulation results is needed in order to define the limits of the equation parameters. Nonetheless, the *Gielis* formula provides the advantage of controlling the size and the shape of the patch through only six parameters (four if symmetry is required). Thus, the optimization process becomes simpler provided that we have correctly set the bounds in the optimizer tool.

Two supershaped configurations were chosen as building blocks for the two novel proposed designs, one from the $m = 1$ and the other from the $m = 2$ subgroup. The selection was based on the required operating frequencies and the radiation patterns we want to achieve. These two supershaped patch antennas were especially designed for WLAN applications. Both antennas cover the frequency bands $2.4 - 2.5\,GHz$ and $5.15 - 5.75\,GHz$, are linearly polarized, have broadside radiation patterns and have low cross-polarization levels. Moreover, they achieve a frequency ratio greater than $2 : 1$. Therefore, they consist a attractive candidate for the WLAN IEEE $802.11a/b/g/n$ standards.

The first antenna is a supershaped printed dipole antenna with a concave ring slot on each flair. It is comprised of two supershaped patches coming from the $m = 1$ subgroup, symmetrically positioned with respect to $y - z$ plane. The antenna is fed by two metallic pins forming a $100\,Ohm$ input impedance. The concave slots are introduced for the configuration of the two bands. The variation of the gap width provides the possibility of controlling the bandwidth of the $2.4\,GHz$ band independently, without affecting the high band. In contrast with other microstrip antenna architectures, the bandwidth enhancement of the low band is achieved while keeping the antenna dimensions unchanged. Because of the perfect symmetry of the structure the cross-polarized radiation is extremely reduced, that is less than $-160\,dB$, which is the lowest ever recorded for a microstrip antenna. Furthermore, a ground plane is introduced in order to have uni-directional radiation patterns. The successful insertion of the ground plane was achieved by implementing the $\lambda/8$ backing height technique instead of the traditional $\lambda/4$ rule.

The second design is a supershaped annular-ring slotted patch antenna fed by a $50\,Ohm$ SMA connector. In this antenna a ring slot, whose profile is defined by the *Gielis* equation for $m = 2$, is used to create dual-band operation. This antenna provides the possibility of centring the resonant frequencies and controlling the frequency ratio through the scaling of the inner and outer annular ring contour. This is simply done by tuning the parameter values $\alpha = b$ involved in the *Gielis* formula. As a result, a frequency ratio f_h/f_l approximately ranging from 1.3 to 3 can be obtained. The radiation patterns are broadside and the cross-polarization levels are low. Especially At the $x-z$ symmetry plane we observe extremely low cross-polarized radiation due to the symmetry along the x-axis. Other discrete features of this antenna are the frequency selective behaviour and the high quality factor yielding increased sensitivity levels.

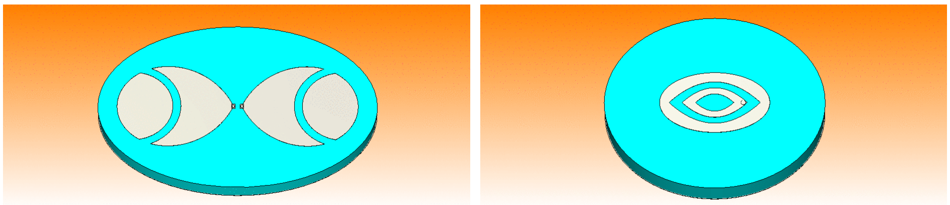

(a) The supershaped printed dipole **(b)** The supershaped ring slotted patch

Figure 9.2 The proposed designs based on the *Gielis* equation

In section 8.3 some similar research studies are quoted for comparison reasons. Both designs outperform their counterparts and significantly improve their performance characteristics.

9.2 Remarks and recommendations for future work

The supershaped patch antenna concept is an extended project whose limits are not known yet. This fact provides plenty exploration possibilities for the future. Particularly, in this thesis, only a small part of the possible supershaped radiators are simulated and analysed because of limited resources. Therefore, more *Gielis* shapes should be simulated so as to extend the data base and to broaden the selection space of the available patch shapes. So, depending on the antenna application one can have the right starting point for further optimization. For example, supershaped monopoles could be a possible future investigation topic.

Regarding the new designs, a different version of the supershaped printed dipole can be created if we use convex slots instead of concave ones. In this case, we still have multi-band operation but with a different frequency response profile. Also, the printed dipole antenna can be easily transformed into an ultra-wideband antenna by removing the slots and appropriately adjusting the relevant parameters. The UWB supershaped dipole can then compete the UWB planar bulbous dipole antenna and be successfully embedded in a ground penetrating radar.

Additionally, there is room for improvement in the feeding method of the supershaped annular slotted patch antenna. A proximity coupled feeding or an aperture coupled feeding can ameliorate the radiation patterns, decrease the cross-polarization in the $y - z$ plane and enhance the bandwidth performance.

Bibliography

[1] D. D. Greig and H. F. Engelmann, "Microstrip - a new transmission technology for the kilomegacycle range", *Proc. IRE*, vol. 40, pp. 1644-1650, 1952.

[2] G. A. Deschamps, "Microstrip Microwave Antennas", Presented at the *Third USAF Symposium on Antennas*, 1953.

[3] J. Q. Howell, "Microstrip antennas", *IEEE Group on Antennas and Propagation Int. Symp.,*, pp. 177-180, Dec. 1972.

[4] R. E. Munson, "Conformal microstrip antennas and microstrip phased arrays", *IEEE Trans. on Antennas and Propagation*, vol.22, no. 1, pp. 74-78, Jan. 1974.

[5] C. A. Balanis, "Antenna theory analysis and design", *John Wiley & Sons, Inc*, 2005.

[6] W. F. Richards, Y. T. Lo, and D. D. Harrison, "An improved theory for microstrip antennas and applications", *IEEE Trans. Antennas Propag*, vol. AP-29, pp. 38-46, 1981.

[7] J. R. Mosig and F. E. Gardiol, "General integral equation formulation for microstrip antennas and scatters", *IEE Proc.*, vol. 132, no. 7, pt. H, pp. 424-432, 1985.

[8] A. Reineix and B. Jecko, "Analysis of microstrip patch antennas using the finite difference time domain method", *IEEE Trans. Antennas Propag.*, vol. 37, no. 11, pp. 1361-1369, 1989.

[9] K. F. Lee and K. F. Tong, "Microstrip Patch Antennas - Basic Characteristics and Some Recent Advances", *Proceedings of the IEEE*, vol. 100, no. 7, July 2012.

[10] W. Chen, K. F. Lee and R. Q. Lee, "Spectral-Domain Moment-Method Analysis of Co-planar Microstrip Parasitic Subarrays", *Microwave and Optical Technology Letters*, vol. 6, no. 3, pp. 157-163, 1993.

[11] C. Wood, "Improved Bandwidth of Microstrip Antennas Using Parasitic Elements", *IEE Proc., Pt. H*, vol. 127, pp. 231-234, 1980.

[12] C. K. Aanandan, P. Mohanabm and K. G. Nair, "Broad-Band Gap Coupled Antenna", *IEEE Trans. Antennas Propagation*, vol. AP-38, no. 10, pp. 1581-1586, 1990.

[13] G. Kumar and K. C. Gupta, "Broadband microstrip antennas using additional resonators gap-coupled to radiating edges", *IEEE Trans. Antennas and Propagation*, vol. AP-32, pp. 1375-1379, 1984.

[14] R. Q. Lee, K. F. Lee and J. Bobinchak, "Characteristics of a two-layer electromagnetically coupled rectangular patch antenna", *Electronics Letters*, vol. 23, no. 20, pp. 1070-1073, 1987.

[15] T. Huynh and K. F. Lee, "Single-layer single-patch wideband microstrip antenna", *Electronics Letters*, vol.31, no. 16, pp. 1310-1312, 1995.

[16] K. F. Lee, K. M. Luk, K. F. Tong, S. M. Shum, T. Huynh and J. R. Q. Lee, "Experimental and simulation studies of the coaxially-fed U-slot rectangular patch antenna", *IEE Proc. Microwaves, Antennas and Propagation*, vol. 144, no. 5, pp. 354-358, 1997.

[17] Z. N. Chen, "Experimental investigation on impedance characteristics of patch antenna with with finite-size substrate", *Microwave and Optical Technology Letters*, vol. 25, no. 2, pp. 107-111, 2000.

[18] K. M Luk, C. L. Mak, Y. L. Chow and K. F. Lee, "Broadband microstrip patch antenna", *Electronics Letters*, vol. 34, pp. 1442-1443, 1998.

[19] F. Croq and A. Papiernik, "Large bandwidth aperture-coupled microstrip antenna", *Electronics Letters*, vol. 26, pp. 1293-1294, 1990.

[20] S. D. Targonski, R. B. Waterhouse and D. M. Pozar, "Design of wide-band aperture-stacked patch microstrip antennas", *IEEE Trans. Antennas Propagation*, vol. 46, no. 9, pp. 1245-1251, 1998.

[21] F. Yang, X. Zhang, X. Ye and Y. Rahmat-Samii,"Wide-Band E-Shaped Patch Antennas for Wireless Communications",*IEEE Transactions on Antennas and Propagation*, vol. 49, no. 7, July 2001.

[22] S. K. Sharma and L. Shafai, "Investigations of a novel ψ-shape microstrip patch antenna with wide impedance bandwidth", *IEEE An-*

tennas and Propagation Society International Symposium, pp. 881-884, June 2007.

[23] B. L. Ooi and I. Ang, "Broadband semicircle-fed flower-shaped microstrip patch antenna", *Electronics Letters*, vol. 41, no. 17, August 2005.

[24] B. Mirzapour and H. R. Hassani, "Wideband and small size star-shaped microstrip patch antenna", *Electronics Letters*, vol. 42, no. 23, November 2006.

[25] A. A. Lotfi Neyestanak, "Ultra wideband rose leaf microstrip patch antenna", *Progress in Electromagnetics Research*, PIER 86, pp. 155-168, 2008.

[26] M. Abbaspour and H. R. Hassani, "Wideband star-shaped microstrip patch antenna", *Progress in Electromagnetics Research Letters*, vol. 1, pp. 61-68, 2008.

[27] S. A. Long and W. D. Walton, "A dual-frequency stacked microstrip circular-disk antenna", *IEEE Trans. Antennas Propagation*, vol. AP 27, pp. 270-273, 1979.

[28] J. S. Dahele and K. F. Lee, "Theory and experiment on microstrip antennas with airgaps", *IEE Proc.*, vol. 132, Pt H, no. 7, pp. 455-460, 1985.

[29] J. Anguera, G. Font, C. Puente, C. Borja and J. Soler, "Multifrequency microstrip patch antenna using multiple stacked elements", *IEEE Microwave and Wireless Compon. Lett.*, vol. 13, pp. 123-124, March 2003.

[30] S. S. Zhong and Y. T. Lo, "Single-element rectangular microstrip antenna for dual-frequency operation", *Electronics Letters*, vol. 19, pp. 298-300, 1983.

[31] K. F. Lee, K. M. Luk and J. S. Dahele, "Characteristics of the equilateral triangular patch antenna", *IEEE Trans. Antennas and Propagation*, vol. 36, pp. 1510-1518, 1988.

[32] S. Maci, G. Biffi Gentili, P. Piazzesi and C. Salvador, "Dual-band slot-loaded patch antenna", *IEE Proc, Microwave Antennas*, Propagation H, vol. 142, pp. 225-232, 1995.

[33] K. F. Lee and K. M. Luk, "Microstrip Patch Antennas", *Imperial College press*, 2011.

[34] Z. N. Chen and M. Y. W. Chia, ”Broadband Planar Antennas”, *John Wiley & Sons, Ltd*, 2006.

[35] K. F. Lee, S. L. S. Yang and A. A. Kishk, ”Dual- and Multi-Band U-Slot Antenna”, *IEEE Antennas and Wireless Propagation Letters*, vol. 7, pp. 645-647, 2008.

[36] S. L. S. Yang, K. F. Lee, A. A. Kishk and K. M. Luk, ”Design and study of wideband single feed circularly polarized microstrip antenna”, *Progress in Electromagnetic Research*, vol. 80, pp. 45-61,2008.

[37] K. F. Tong and T. P. Wong, ”Circularly Polarized U-slot Antenna”, *IEEE Transactions on Antennas and Propagation*, vol. 55, no. 8, August 2007.

[38] A. Khidre, K. F. Lee, F. Yang and A. Elsherbeni, ”Wideband circularly polarized E-shape patch antenna for wireless communications”, *IEEE Antennas and Propagation Magazine*, vol. 52, no. 5, pp. 219-229, October 2010.

[39] P. Nayeri, K. F. Lee, A. Elsherbeni and F. Yang, ”Dual-band circularly polarized antennas using stacked patches with asymmetric U-slots”, *IEEE Antennas and Wireless Propagation Letters*, vol. 10, pp. 492-495, 2011.

[40] K. L. Chung and A. S. Mohan, ”A systematic design method to obtain broadband characteristics for singly-fed electromagnetic coupled patch antennas for circular polarization”, *IEEE Transactions on Antennas and Propagation*, vol. AP-51, pp. 3239-3248, 2003.

[41] P. S. Hall and J. S. Dahele, ”Dual and circularly polarized microstrip antennas”, *Advances in Microstrip and Printed Antennas*, K. F. Lee and W. Chen, John Wiley & Sons, New York, 1997.

[42] A. Adrian and D. H. Schaubert, ”Dual aperture-coupled microstrip antenna for dual or circular polarization”, *Electronics Letters*, vol. 23, pp. 1226-1228, 1987.

[43] C. H. Tsao, Y. M. Hwang, F. Killburg and F. Dietrich, ”Aperture-coupled patch antennas with wide-bandwidth and dual polarization capabilities”, *IEEE Antennas Propag. Soc. Int. Symp. Dig.*, vol. 3, pp. 936-939, 1988.

[44] Y. T. Lo, D. Solomon and W.F. Richards, ”Theory and experiment on microstrip antennas”, *IEEE Transactions on Antennas and Propagation*, vol. 27, no.2, pp. 137-145, Mar. 1979.

[45] E. H. Newman and P. Tulyathan, ”Analysis of Microstrip Antennas Using Moment Methods”, *IEEE Transactions on Antennas and Propagation*, vol. 29, no. 1, Jan. 1981.

[46] A. Reineix and B. Jecko, ”Analysis of microstrip patch antennas using finite difference time domain method”, *IEEE Transactions on Antennas and Propagation*, vol. 37, no. 11, Nov. 1989.

[47] R. Hestand and C. Christodoulou, ”Analysis of planar microstrip antennas using the finite element method”, *IEEE Proc. Southeastcon ’96*, pp. 136-139, April 1996.

[48] T. Weiland, ”A discretization method for the solution of Maxwell’s equations for six-component fields”, *Electronics and Communication (AEÜ)*, vol. 31, pp. 116-120, Mar. 1977.

[49] J. Gielis, ”A generic geometric transformation that unifies a wide range of natural and abstract shapes”, *American Journal of Botany*, vol. 90, no. 3, pp. 333-338,2003.

[50] Y. H. Suh and K. Chang, ”Low cost microstrip-fed dual frequency printed dipole antenna for wireless communications”, *Electronics Letters*, vol. 36, no. 14, pp. 1177-1179, 2000.

[51] C. M. Su, H. T. Chen and K. L. Wong,”Printed dual-band dipole antenna with U-slotted arms for 2.4/5.2 GHz WLAN operation”, *Electronics Letters*, vol. 38, no. 22, pp. 1308-1309, 2002.

[52] Z. Zhang, M. F. Iskander, J.-C. Langer and J. Mathews,”Dual-Band WLAN Dipole Antenna Using an Internal Matching Circuit”, *IEEE Transactions on Antennas and Propagation*, vol. 53, no. 5, pp. 1813-1818, May 2005.

[53] N. Zhang, P. Li, B. Liu, X.W. Shi and Y.J. Wang, ”Dual-band and low cross-polarisation printed dipole antenna with L-slot and tapered structure for WLAN applications”, *Electronics Letters*, vol. 47, no. 6, pp. 360-361. 2011.

[54] M.-C. Chang and W.-C. Weng, ”A Dual-Band Printed Dipole Slot Antenna for 2.4/5.2 GHz WLAN Applications”, *IEEE International Symposium on Antennas and Propagation (APSURSI)*, pp. 274-277, 2011.

[55] C.-Y.-D. Sim, H.-Y. Chien, and C.-H. Lee, ”Dual-/Triple-Band Asymmetric Dipole Antenna for WLAN Operation in Laptop Computer”, *IEEE Trans. on Antennas and Propagation*, vol. 61, no. 7, pp. 3808-3813, July 2013.

[56] Z. Nie, W. C. Chew and Y. T. Lo, ”Analysis of the Annular-Ring-Loaded Circular-Disk Microstrip Antenna”, *IEEE Trans. on Antennas and Propagation*, vol. 38, no. 6, pp. 806-813, June 1990.

[57] B. K. Kanaujia and A. K. Singh, ”Analysis and Design of Gap-Coupled Annular Ring Microstrip Antenna”, *International Journal of Antennas and Propagation*, Hindawi Publishing Corporation, vol. 2008, 2008.

[58] S. Saxena and B. K. Kanaujia, ”Design and simulation of a dual band gap coupled annular ring microstrip antenna”, *International Journal of Advances in Engineering & Technology*, vol. 1, no. 2, pp. 151-158, May 2011.

[59] P. Singh, D. C. Dhubkarya and A. Aggrawal, ”Design and Analysis of Annular Ring Slot MSA for wireless and UHF Applications”, *Conference on Advances in Communication and Control Systems (CAC2S 2013)*, pp. 541-544, 2013.

Acknowledgements

The implementation of this MSc thesis project was an absolutely valuable experience for me. It gave me the chance to explore some interesting aspects of the applied electromagnetism field within the framework of microstrip patch antenna systems. The first logical step was the wide comprehension of the basic principles of the electromagnetic theory. Afterwards, it comes the effort to control these physical phenomena so as to adjust their operation in real-life matters, such as the development of microstrip patch antennas. All this, was for me a fascinating learning journey that allowed me to build a strong background as electrical engineer.

Apart from my own efforts, also some other people in TU Delft contributed to the implementation of this work. I would like to express my sincere thanks to my supervisor Dr. Diego Caratelli for his support and his useful feedback and Dr. Massimiliano Simeoni for giving me the opportunity to carry out this thesis project. Also, I want to express my appreciation to my graduation professor prof. dr. Alexander Yarovoy for his help and encouragement. Finally, some special mention to Ir. Dani Tran. I cannot say thanks enough for his important help and support. The discussions with him were always meaningful and enlightening.

On a personal note, I would like to express my love to my family who inspired, encouraged and fully supported me in every aspect of my life. I thank them for giving me not just financial but moral and spiritual support as well. And of course, a big ”thank you” to Alex for his patience, support and helpful advice.